The Dissertation Committee for Annie C. Weathers
certifies that this is the approved version of the following dissertation:

Transport and Coupling of Phonons, Electrons, and Magnons in Complex Materials

Committee:

_____

Li Shi, Supervisor

_____

John B. Goodenough

_____

Xiaoqin E. Li

_____

John T. Markert

_____

Raymond Lee Orbach

Transport and Coupling of Phonons, Electrons, and Magnons in Complex Materials

by

Annie C. Weathers, BS; MSE

DISSERTATION

Presented to the Faculty of the Graduate School of

The University of Texas at Austin

in Partial Fulfillment

of the Requirements

for the Degree of

DOCTOR OF PHILOSOPHY

THE UNIVERSITY OF TEXAS AT AUSTIN

May 2016

Dedicated to Mom, Dad, Jess, Margy,

and Matt

Acknowledgments

I would like to sincerely thank my advisor, Professor Li Shi, without whom I would never have been introduced to the field of nanoscale heat transport. His patience, expertise, and encouragement have been invaluable during my graduate studies, and I am very grateful to have shared such rich discussions with him over the years. In addition, I would also like to thank my dissertation committee for all their time in providing thoughtful comments on this dissertation.

My graduate studies at UT have been a vibrant experience because of the support and friendship from all of the students and post-docs in Professor Li Shi's group and throughout UT. In particular, I would like to thank Dr. Xi Chen, for his guidance in working on the higher manganese silicide systems, and Sean Sullivan, Kevin Olsson, and Kyongmo An for their collaboration in designing and setting up our Brillouin light scattering system. I would also like to thank Dr. Jaehyun Kim, Dr. Insun Jo, and Dr. Michael T. Pettes for their expert guidance in all manner of microfabrication techniques. In addition, I am very grateful to the staff at the Microelectronics Research Center for their hard work in maintaining a safe and well-functioning research facility.

Lastly, I would like to thank my friends in Austin and my family for their unwavering support and inspiration during my graduate studies. I have inherited all of my diligence and intellectual curiosity from my parents, who have taught me the vast importance of a deep and thoughtful education, and the joys that one can find from it. In this short acknowledgment, it is not possible to fully express my gratitude towards my husband, Matt, for all of his love and support during my graduate work. I am so happy to be able to spend time with someone who has such enthusiasm for engineering and science.

Transport and Coupling of Phonons, Electrons, and Magnons in Complex Materials

Publication No. _____

Annie C. Weathers, Ph.D.
The University of Texas at Austin, 2016

Supervisor: Li Shi

In nanoscale systems, in which the relevant length scales can be comparable to the mean free paths and wavelengths of the energy, charge and spin carriers, it is necessary to examine the microscopic transport of heat, spin and charge at the atomic scale and the quantization of the associated quasiparticles. The intricacies of the transport dynamics can be even more complicated in materials with atomic scale complexities, such as incommensurate crystals, magnetic materials, and quasi-one-dimensional systems. Meanwhile, the transport properties and coupling between these quasiparticles is important in determining the strength of various thermoelectric and spincaloritronic phenomena, as well as the reliability of nanoscale electronics.

This work seeks to further the understanding of the complicated transport dynamics in complex structured materials at nanometer and micrometer length scales, and to address some of the fundamental questions about the interactions between energy, charge and spin carriers in the conducting polymer poly(3,4- ethylenedioxythiophene) (PEDOT), the incommensurate higher manganese silicide (HMS) thermoelectric material, and the magnetic insulator yttrium iron garnet (YIG). These questions are addressed through a number of combined experimental approaches through the use of thermal conductance and thermoelectric property measurements of suspended nanostructures, inelastic neutron scattering, Brillouin light scattering, and electron microscopy.

According to in-plane thermal and thermoelectric transport measurements of PEDOT thin films, the electronic thermal conductivity of this conducting polymer is found to be significant and exceeds that predicted by the Wiedemann-Franz law for metals. Furthermore, thermoelectric transport measurements of suspended HMS nanoribbons show a reduction in the lattice thermal conductivity by approximately a factor of two compared to bulk HMS, which is qualitatively consistent with that predicted from a diffuson model for thermal conductivity derived from the phonon dispersion of HMS. Lastly, pressure dependent Brillouin light scattering spectroscopy is used to determine the influence of hydrostatic stress on the dispersions of magnons and phonons in YIG, in order to determine the magnon and phonon peak frequency shift associated with localized laser heating induced strain.

Table of Contents

Chapter 1

Introduction

Understanding the fundamental, microscopic origins of energy transport is the foundation of nanoscale heat transfer. In systems in which the relevant length scales are comparable to the mean free paths and wavelengths of the energy carriers, such as in nanoscale electronics and nanostructured materials, the classical heat transport laws are unable to capture the true physics of the system. Instead, it is necessary to consider the mechanisms of heat transport at atomic scales and the resulting quantization of the quasiparticles that carry energy. In materials with atomic scale complexities, the mechanics of heat transport can become even more complicated because of the intricacies of the energy carrier dynamics and the coupling between different kinds of energy carriers – namely, lattice vibrational modes, charge carriers, and magnetic excitations.

The study of nanoscale heat transport is a fundamental subject that is important for both managing the heat generated in nanoscale electronics and in engineering material systems with improved energy conversion efficiencies. For example, in logic devices with nanometer scale channel lengths, the dissipation of heat is an important design challenge that can dramatically limit the device reliability and performance.[1] This challenge has motivated a strong interest in finding substrate and component materials with outstanding heat conduction properties, for example BAs,[2] diamond,[3] graphene,[4] and other carbon based materials.[5]

The efficiencies of energy conversion devices, e.g., thermoelectric modules, are also governed by the fundamental heat carrier transport mechanisms. Thermoelectric materials are characterized by the ability to convert a temperature gradient across the

material into an electrical potential, or vice versa as a solid state heat pump. Thermoelectrics generators have found niche applications in powering space exploration missions and cooling small scale refrigeration units. More recently, they have also been investigated for waste heat recovery in automobiles and industrial power plants. For example, a number of automobile manufacturers have begun investigating how to incorporating thermoelectric generators on the exhaust manifold of gasoline and diesel vehicles in order to power low voltage appliances.[6] However, the cost-to-efficiency is still not competitive to warrant wide spread adoption.

The efficiency of a thermoelectric material depends on the thermoelectric figure of merit, $zT = S^2\sigma T/\kappa$, where S is the Seebeck coefficient, i.e., thermopower, σ is the electrical conductivity, T is the temperature, and κ is the thermal conductivity. Thermoelectric materials research has focused on improving the material's zT through both top-down and bottom-up nanoscale and materials engineering.[7,8] However, the coupling between S, σ, and κ in a single material can make the optimization of zT challenging.

The basis of thermoelectric research has been in understanding the transport and coupling of charge and heat carriers, and in manipulating their properties for improved efficiencies. Large improvements in the thermoelectric efficiency have been demonstrated by reducing the lattice thermal conductivity through nanostructuring[9] and the engineering of complex crystal structures,[10] as well as improving the power factor, $S^2\sigma$, by tuning the electronic density of states with impurity doping.[11,12] Recently, it has been suggested that a zT higher than 2 is possible in some SnSe and PbTe based systems.[13,14] However, the highest efficiency thermoelectric materials are almost exclusively based on expensive, toxic, or rare materials, such as Pb and Te. Therefore, there has been an industrial need for low-cost thermoelectric materials based on non-toxic and abundant materials with an improved cost-to-efficiency ratio. Conducting polymer thermoelectrics are one material system being investigated for their low-cost and mechanical flexibility.[15] Likewise, half-Heusler, oxide, cathrate, and silicide inorganic thermoelectric materials based on low-cost and abundant materials

have generated considerable interest.[16,17]

While thermoelectric devices convert heat to electricity through the coupling of heat and charge currents, the nascent field of spincaloritronics is focused on designing energy conversion devices based on manipulating heat and *spin* currents in magnetic and spin-polarized materials. A number of recent discoveries within the field, including the spin Seebeck effect,[18-20] spin Peltier effect,[21] large magnon thermal conductivity,[22] and thermal spin transfer torque,[23-25] have provided new and unique approaches to thermal spin injection,[26,27] thermally induced domain wall motion,[28] and energy conversion devices.[29,30]

The investigation of thermoelectric and spincaloritronic phenomenon requires an acute understanding of the interplay between the carriers of charge, heat, and spin. For example, while charge is typically carried by electrons and holes in metallic and semiconducting solids, heat can be carried by lattice vibrations, charge carriers, and magnetic excitations such as magnons, the latter of which also carries spin. In a crystalline material, lattice vibrations exist as quantized vibrational modes, referred to as phonons, whose characteristics depend on their energy and momentum. Acoustic phonons are vibrational modes with low energy, in which atoms moves collectively in-phase with relatively large group velocity and often over long distances before being scattering. As the name suggests, acoustic modes with very low momentum are responsible for the propagation of sound in a solid. Optical phonon modes, on the other hand, are characterized by high energy, out-of-phase motions of atoms within a single unit cell, and earn their name from their strong coupling with light.

Magnons, which are quantized spin waves generated in a magnetic material, are equally complex in their spectral properties, especially because the direction of propagation could be either perpendicular or parallel to the direction of magnetization, resulting in characteristically different modes. In addition, magnons in different ranges of the energy and momentum spectrum can have drastically different mean free paths because of differences in the inelastic coupling with phonons and coupling with other magnon modes. While high-energy thermal magnons ($E > k_b T$) with

strong phonon interactions and correspondingly short mean free paths can store a significant amount of thermal energy, subthermal magnons with low energy and long mean free paths are suspected to be most important for a variety of spincaloritronic phenomenon.[31,32]

Simultaneously, heat is also carried by charge carriers in a metallic or semiconducting material. In a generic semiconductor, the electronic thermal conductivity is composed of a contribution to the heat current from each transport band (electrons, holes, or both). In addition, in an intrinsic semiconductor with a finite band gap, or in a semimetal with overlapping bands, a bipolar contribution to the thermal conductivity from electron hole pairs is also present. The theory of electronic thermal transport is often explained by the Wiedemann-Franz law, which states that the ratio of the electronic thermal conductivity to the electrical conductivity, κ_e/σ, is proportional to temperature, T, with a proportionality constant termed the Lorenz number, L. This relationship is application to a wide variety of metallic and semiconducting materials, with a Lorenz number on the order of k_b^2/q^2, and whose exact value depends on the dispersion and scattering processes of the charge carriers.

While the transport properties of magnons, phonons, and electrons are dictated by their respective dispersions and scattering mechanisms, the macroscopic transport of heat in a material and the magnitude of the various thermoelectric and spincaloritronic phenomena are ultimately determined by the microscopic exchange of energy and momentum between heat, charge and spin carriers. This work aims to address some of the fundamental questions about the interactions between phonons, magnons, and charge carriers in materials with structural and magnetic complexity.

Chapter 2 discusses the experimental methods necessary for probing the transport properties of phonons, electrons, and magnons. Methods of measuring the thermoelectric properties of suspended nanostructures, the dispersion of phonons with inelastic neutron scattering, and the frequency of low energy magnons and phonons with Brillouin light scattering will be discussed.

Chapter 3 investigates the coupling of charge and heat transport in the conducting polymer poly(3,4-ethylenedioxythiophene) (PEDOT), which is a leading candidate for polymer based thermoelectrics and is a low-cost and non-toxic alternative to state-of-the-art thermoelectric materials. The thermoelectric properties along the same transport direction and on the same suspended PEDOT sample are measured, and the ratio of the electrical to thermal conductivity is used to determine the contribution to the thermal transport from charge carriers in PEDOT. Furthermore, from the measured thermoelectric properties, the applicability of the Wiedemann-Franz law in this complex conducting polymer system is examined, as this is a fundamental question important for the development of organic electronic and thermoelectric materials.

Like conducting polymers, silicide based thermoelectrics materials also offer affordability and abundance compared to PbTe and Bi_2Te_3 based thermoelectrics. In particular, higher manganese silicide (HMS) is an increasingly competitive thermoelectric material that is both environmentally stable and composed of the earth abundant elements Si and Mn. HMS is characterized by a phenomenally low and anisotropic thermal conductivity, a complicated and unusual crystal structure, and an equally unusual phonon dispersion. Despite knowledge of the lattice structure of HMS, there has been a lack of understanding of how the structure and phonon dynamics influence the thermal conductivity. Chapter 4 investigates the phonon transport in HMS bulk crystals and nanoribbons in order to shed light on the structure-property relations in this material. The thermoelectric properties of suspended HMS nanoribbons are measured along the same transport direction in order to understand the effects of size confinement on the phonon transport. These results are compared with a recent work that obtained the phonon dispersion of HMS from inelastic neutron scattering and density functional theory calculations, and are compared to a thermal conductivity model used to predict the thermal conductivity of nanostructured HMS.

Finally, Chapter 5 examines the phonon and magnon transport in the magnetic insulator yttrium iron garnet (YIG) using Brillouin light scattering. A variable

temperature and variable pressure Brillouin light scattering setup has been built, which can simultaneously measure the low energy phonon and magnon modes in a material at both ambient pressure and under hydrostatic pressure. The magnon and phonon frequencies as a function of hydrostatic pressure are investigated to determine the effects of strain on the phonon and magnon frequencies in YIG.

The results from this work are expected to provide fundamental insights into the transport and coupling of heat carriers in a number of complex materials important for the advancement of low-cost, high-efficiency and high-throughput energy conversion technologies.

Chapter 2

Methods of Probing Thermoelectric and Magnetic Transport at the Nanoscale

Nanomaterials, such as two-dimensional (2D) layered materials, carbon nanotubes (CNTs), aligned polymer fibers, and semiconductor nanowires and thin films have provided a wealth of new possibilities for functional devices with improved efficiencies. For example, graphene and carbon nanotubes have been lauded for their enormously high thermal conductivity that is desirable for thermal management applications,[33] and nanowire and carbon nanotube transistors are in the early stages of commercialization.[34] Similarly, in logic devices with device dimensions on the order of the phonon and electron mean free paths, the generation of local hot spots on the sub-device scale and chip-level scale can be detrimental to the device performance and reliability.[35] This challenge can be even more problematic for novel, non-planar device designs and three-dimensional (3D) packaging of logic devices. In these electronic devices, the dissipation of heat from local hot spots is a crucial design parameter, for which an accurate understanding of nanoscale heat transport is essential.

Furthermore, nanostructuring has become a key component in optimizing the efficiency of thermoelectric materials, which benefit from reduced thermal conductivity.[36] However, characterization of the transport properties of such nanoscale materials has remained a difficult and often tedious task compared to measurements of bulk materials. Furthermore, the characterization of thermal transport properties are typically even more difficult than electrical transport measurements because of systemic issues such as radiation and conduction heat loss to the environment and substrate and contact thermal resistance at the thermometer contacts.

Over the past few decades, a number of experimental methods have been developed to overcome these difficulties in characterizing the thermoelectric transport properties of nanoscale samples.[37] For example, a number of methods based on pulsed or modulated self-heating of the sample have been reported, such as the 3ω method for thermal conductivity measurements of thin films, nanowires and nanotubes,[38–42] and transient electrothermal techniques for measuring the thermal conductivity and diffusivity of nanowires.[43] In addition, time-domain thermoreflectance (TDTR)[44] has become the definitive method for studying the interfacial thermal resistance of thin films, and is particularly useful for measuring the cross-plane thermal conductivity of thin films. Other optical-based non-contact methods such as micro-Raman spectroscopy[45] and frequency domain thermoreflectance (FDTR)[46] have also been explored for measuring the thermal conductivity of thin films at high spatial resolution. Moreover, methods based on a steady state temperature difference applied to each end of the sample, such as bimaterial cantilever sensors,[47] T-junction sensors,[48] and suspended resistance thermometer devices[49] have been popular because of the relative simplicity in the measurement method and the data analysis, despite the difficulty in fabricating such devices.

In addition to the characterization of the thermal and thermoelectric transport properties in nanoscale samples, a complete understanding of the thermal transport in these systems requires accurate knowledge of the microscopic transport of the heat carriers, in particular, knowledge of the scattering length scales and the dispersion of the energy carriers. The dispersion of energy carriers such as phonons, magnons and electrons can be determined computationally by density functional theory and lattice dynamics simulations, and experimentally with inelastic neutron scattering for phonons and magnons or angle-resolved photoemission spectroscopy (ARPES) for electrons.[50,51] Furthermore, the mean free path spectrum of phonons has been measured experimentally in semiconductor systems by applying a laser induced temperature gradient over a length scale comparable to the mean free path of phonons, in a method now referred to as mean free path spectroscopy.[52–54] The transport of

magnons, the quanta of spin waves, has been studied by a variety of methods, including electrical contact based methods such as ferromagnetic resonance (FMR) of magnetic thin films[55] and more recently by the inverse spin hall effect (ISHE) through the spin Seebeck effect.[20] Non-contact optical methods such as time domain magneto-optic Kerr effect (MOKE) can provide picosecond resolution of THz magnons.[26,56] Similarly, frequency domain Brillouin light scattering[57] and Raman spectroscopy[58–60] are popular methods for probing magnons over a wide range of energies, with up to 250 nm spatial resolution.[61]

Within the emerging field of spincaloritronics, the transport and coupling of phonons and magnons is important in understanding many of the thermally driven spincaloritronic phenomena, including the spin Seebeck effect (SSE),[18,19] spin Peltier effect (SPE),[21] thermal spin transfer torque (TSST),[23,25] and the large magnon thermal conductivity in complex spin ladder compounds.[62,63] In order to understand the transport and coupling of phonons and magnons in these magnetic materials, it is necessary to devise measurement methods capable of probing not only magnetic excitations, but also the accompanying phonon modes in the system, both of which can carry heat. Furthermore, the non-equilibrium between magnons, phonons, and electrons can be crucial in explaining some of these spincaloritronic phenomena. However, measuring the non-equilibrium between these heat carriers requires the generation of a temperature gradient at a length scale smaller than the intrinsic coupling length between the quasiparticles, which can range from nanometers to microns depending on the material. Brillouin light scattering has been shown to be very useful at simultaneously investigating the broadband of phonon and magnon modes that carry heat in a magnetic material to sub-micron spatial resolution.[64–66] This enables one to probe the local populations of magnons and phonon responsible for these non-equilibrium phenomena.

The remainder of this chapter will outline the measurement techniques used for the work presented in Chapters 3-5. These techniques include steady state thermoelectric property measurements of suspended nanowires and thin films, micro-

Brillouin light scattering, inelastic neutron scattering, and sample fabrication methods.

2.1 Steady State Thermoelectric Transport Measurements of Nanostructures

The steady state comparative method of measuring the heat conduction through a sample and an adjacent reference material has been a common method of measuring the thermal conductivity of bulk crystals. The method was adapted for the measurement of micro-/nano-scale samples by Shi[67] Shi et al.,[49] and Kim et al.[68] using a microfabricated device. In this method, the nanostructure sample is bridged between two adjacent, suspended silicon nitride (SiN) membranes each supported by six SiN beams. The temperature difference across the sample is measured with the platinum resistance thermometers (PRTs) patterned on each membrane while applying a known DC heating to one membrane. This temperature difference is compared to the temperature drop across the supporting SiN beams, whose far end is held at the ambient substrate temperature, in order to determine the thermal conductance of the sample itself.

This method has become an increasingly popular method for measuring thermal transport in a wide variety of materials, including graphene,[69] carbon nanotubes,[70] semiconducting and insulating nanowires and thin films,[71–74] and polymer fibers and thin films,[75–77] owing to the relative ease of the measurement and data analysis once the devices have been batch fabricated. A number of improvements and revisions to the method have been published over the years, including a four probe thermoelectric technique,[71] a differential method which removes any background conductance,[77] and a novel method in which the thermal contact resistance is eliminate from the measurement entirely.[78] The details of the measurement method and sample preparation will be discussed in this section, and the inherent uncertainties and complications will be discussed.
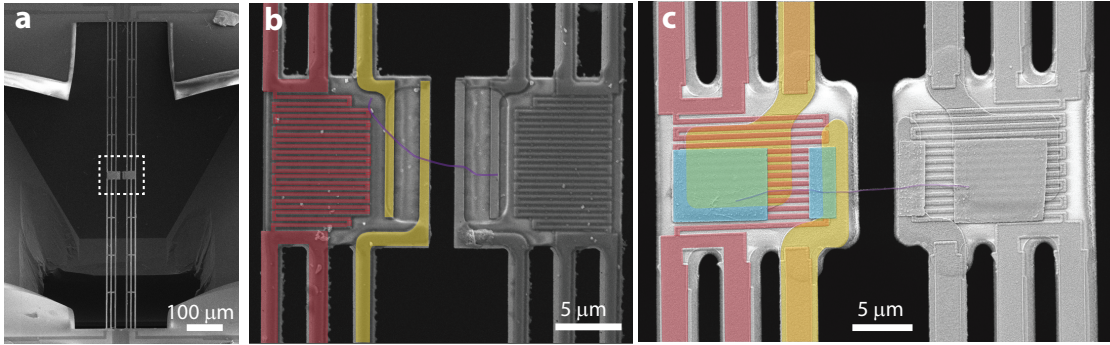
Figure 2.1: Microfabricated devices with false coloring of the Pt electrodes (yellow), platinum resistance thermometer (PRT) (red), sample (purple), and metallic tags (blue). (a) Low magnification image of the microfabricated device showing the long SiN beams. (b) Previous device design with two sample electrodes and one PRT patterned on each membrane. (c) New device design with two sample electrodes patterned on top of the PRT with a HfO_2 dielectric layer between. The blue metallic tags are transferred with the sample to the device.

2.1.1 Thermoelectric Property Measurements

The microfabricated device is composed of two adjacent SiN membranes each supported by six SiN beams. A layer of Cr(6 nm)/Pt(60 nm) covers the top of all twelve beams, which act as conducting leads to the PRTs and two electrodes patterned on each membrane. In addition, four electrode connections to the sample allow for simultaneous four-probe electrical and Seebeck measurements. Figures 2.1a and 2.1b show a device used in previous work with false coloring of the sample, two sample electrodes, and one PRT.

Two-Probe Thermal Measurement Method

In a typical two-probe thermal measurement procedure, the microfabricated device is placed in an evacuated cryostat with a pressure better than 10^{-6} torr. A DC heating current, I, is supplied to the PRT on the heating membrane, which generates a Joule heating power of $Q_h = I^2 R_h$ in the heater serpentine and $Q_L = I^2 R_L$ in each of the current carrying leads, as shown in Figure 2.2a. This raises the temperature of

the heating membrane $\Delta T_h = T_h - T_0$. According to the thermal conduction diagram in Figure 2.2a, some of the heat is conducting through the suspended gap due to both conduction through the sample, Q_s, as well as unwanted background radiation and conduction, Q_{bg}. This raises the temperature of the adjacent sensing membrane by $\Delta T_s = T_s - T_0$. The heat generated in each of the current carrying leads, Q_L, alone generates a parabolic temperature distribution in the long supporting leads. This symmetric temperature profile about the middle of the beam causes half of the heat, $Q_L/2$, to flow to the substrate, while the other half, $Q_L/2$, flows to the heater membrane. With the addition of the heat generated in the heater serpentine, the heat conducted to the substrate through the two current carrying leads ($i = 1, 2$) on the heater side is $Q_{1-2} = 2(g_{b1}\Delta T_h + Q_L/2)$. The heat conducted to the substrate through the non-current carrying leads ($i = 3 - 6$) on the heater side is $Q_{3-6} = 4g_{b1}\Delta T_h$, where g_{b1} is the thermal conductance of each beam on the heater side. Likewise, on the sensing side, the heat conducted to the substrate is $Q_{7-12} = 6g_{b2}\Delta T_s$, where g_{b2} is the thermal conductance of each beam on the sensing side. As shown in the control volume schematic in Figure 2.2a, energy conservation on the heating and sensing membranes requires that the total heat dissipation to the substrate be equal to the total heat generation,[77]

$$Q_h + 2Q_L = 2(g_{b1}\Delta T_h + Q_L/2) + 4g_{b1}\Delta T_h + 6g_{b2}\Delta T_s$$
$$= Q_L + 6g_{b1}\Delta T_h + 6g_{b2}\Delta T_s \tag{2.1}$$

$$Q_{total} \equiv Q_h + Q_L = G_{b1}\Delta T_h + G_{b2}\Delta T_s \tag{2.2}$$

where $G_{bi} = 6g_{bi}$. While G_{b1} and G_{b2} are designed to be equal, there can be minor variations in the fabrication process that cause them to differ. In the general case that they are not equal,

$$1 = \frac{\Delta T_h G_{b1}}{Q_{total}} + \frac{\Delta T_s G_{b2}}{Q_{total}} \tag{2.3}$$

A similar measurement with the heating and sensing membranes switched yields a second equation

$$1 = \frac{\Delta T_s^* G_{b1}}{Q_{total}} + \frac{\Delta T_h^* G_{b2}}{Q_{total}} \tag{2.4}$$

12

where ΔT^* is the temperature measured in the second measurement with reversed heat flow. Eqs. (2.3) and (2.4) can be combined to yield the thermal conductance of the beams,

$$G_{b1} = \frac{\Delta T_h^* - \Delta T_s}{\Delta T_h^* \Delta T_h - \Delta T_s^* \Delta T_s} Q_{total} \tag{2.5}$$

$$G_{b2} = \frac{\Delta T_h - \Delta T_s^*}{\Delta T_h^* \Delta T_h - \Delta T_s^* \Delta T_s} Q_{total} \tag{2.6}$$

The thermal conductance of the sample is then

$$G_s = G_{b2} \frac{T_s}{T_h - T_s} \quad \text{or} \quad G_s = G_{b1} \frac{T_s^*}{T_h^* - T_s^*} \tag{2.7}$$

Previous measurements have assumed that $G_{b1} \approx G_{b2}$, which is typically true within 5% error. For low thermal conductance samples, in which $G_s \ll G_{b1}, G_{b2}$, almost all of the Joule heating will be dissipated through the beams supporting the heating membrane, and therefore the measured G_{b2} will be nearly equal to G_{b1}. As a result, the error in the obtained G_s will be as large as the relative difference between G_{b1} and G_{b2}.

The temperatures ΔT_h and ΔT_s are monitored by supplying a small AC sensing current, $i_{AC} = i_{1\omega} e^{i\omega t}$, to each serpentine. The first harmonic voltages across the serpentines are measured with two lock-in amplifiers and are used to obtain the four-probe differential resistances of the serpentines, $R_h(I)$ and $R_s(I)$. The resistances of the serpentines at zero heating power, $R_h(I = 0)$ and $R_s(I = 0)$, are measured at each ambient temperature, T_0, which yields the temperature coefficient of resistances, dR_h/dT and dR_s/dT. The resistance of the sensing serpentine is converted to a temperature as $\Delta T_s = \Delta R_s/(dR_s/dT)$. On the heating membrane, the coupling between the DC heating current and the first harmonic (1ω) sensing current results in a modulation of Q_h at 1ω and 2ω

$$Q_h = (I^2 + 2I i_{1\omega} e^{i\omega t} + i_{1\omega}^2 e^{2i\omega t}) R_h(I) \tag{2.8}$$

When the lock-in amplifier measures the first harmonic AC resistance of the heating
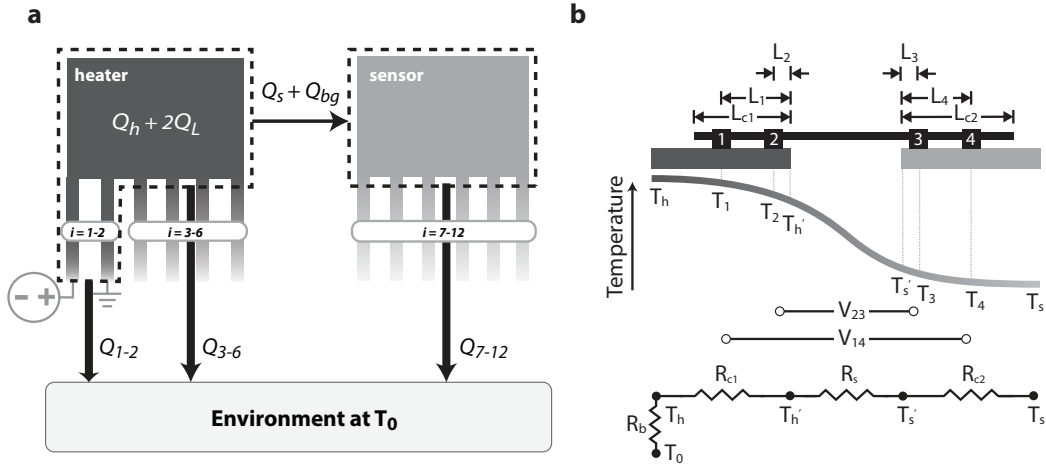
Figure 2.2: (a) Heat conduction pathways from the heater island to the sensor island and the supporting substrate at temperature T_0. Reproduced from Weathers et al.[77] (b) Temperature profile along the sample, and thermal resistance circuit in the four-probe thermal measurement method. Reproduced from Weathers et al.[37]

serpentine, $R_h = v_{1\omega}/i_{1\omega}$, the resulting temperature rise on the heater is given by

$$\Delta T_h(I) = \frac{1}{3}\frac{\Delta R_h}{dR_h/dT} \quad \text{for} \quad \omega \ll 1/\tau \tag{2.9}$$

$$\Delta T_h(I) = \frac{\Delta R_h}{dR_h/dT} \quad \text{for} \quad \omega \gg 1/\tau \tag{2.10}$$

in the low and high frequency limits. The factor of three difference arises as a result of ΔT_h having time to respond fully to the 1ω heating term at low frequencies. This factor of three is indeed observable in the measured resistance as a function lock-in frequency.[49] For a typical time constant of the SiN membrane on the order of 0.1 ms, the high frequency limit is easily achievable with $\omega > 2$ kHz, which ensures that the temperature of the membrane does not have time to respond to the oscillating current.

Differential Measurement Method for Elimination of Background Conductance

In addition to the heat transfer through the sample, there is also a heat transfer from the heating membrane to the sensing membrane due to radiation heat transfer and conduction through residual gas molecules in the evacuated sample space of the cryostat. This background thermal conductance has been previously measured to be 0.4 nW/K at room temperature, and drops to $\sim$ 0.1 nW/K at 100 K,[70] which is comparable to low thermal conductance samples such as single walled carbon nanotubes,[70] polymer nanofibers,[75] and semiconducting nanowires with diameters on the order of 10 nm. While the sensitivity of the thermal conductance measurements can be improved to around 0.01 nW/K with the use of a differential Wheatstone bridge to eliminate the noise from stage temperature fluctuations,[79] the background conductance must be measured at a different time, and later subtracted from the measured sample conductance. The resulting error associated with subtracting two numbers of similar magnitude results in an error in the sample thermal conductance that is on the order of the error in the background conductance.

In order to measure a sample with thermal conductance on the order of 0.1 nW/K, Weathers et al.[77] have developed a method to measure the thermal conductance of the sample relative to a blank reference device with no sample located between the membranes but nearly identical device dimensions and design. As a result, the sample conductance alone is obtained independent of any background conductance, with an error better than 0.1 nW/K, which is sufficient to measure low thermal conductance nanowires of small cross sections. In this method, equal heating power is supplied to both the sample and reference heaters, and the increase in the sensing side temperature on the sample device relative to the temperature rise in a blank device is measured with two lock-in amplifiers. Schematics of the non-differential and differential measurements are shown in Figure 2.3.

Two DC heating currents of I_{DC} and $I_{DC,ref}$ are supplied to the sample and reference device heating membranes, respectively. The heating currents are controlled
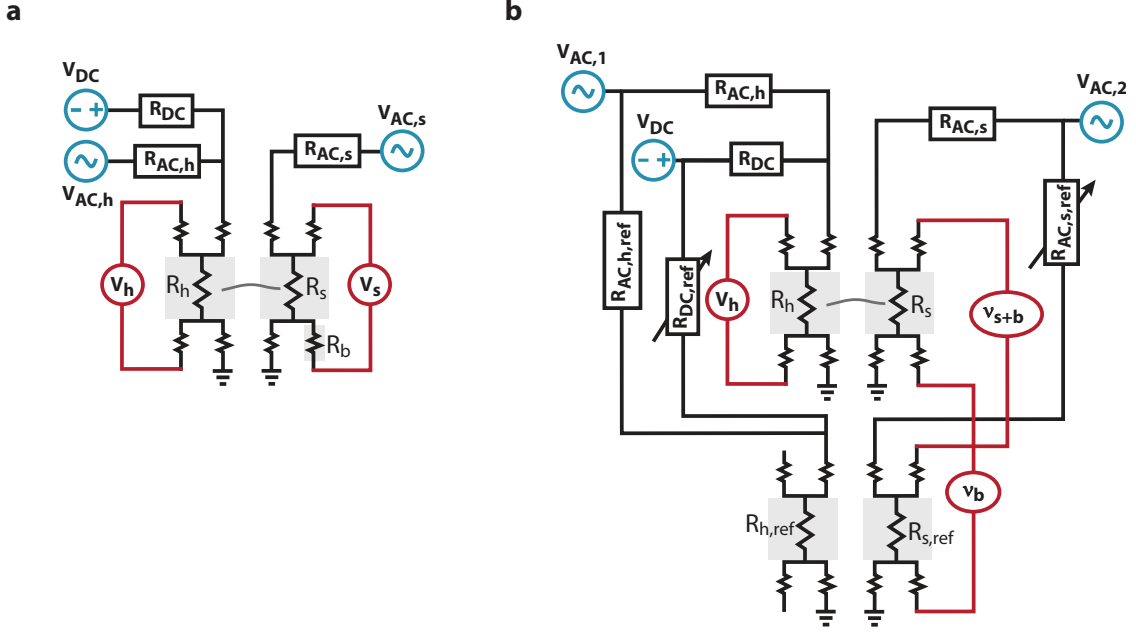
Figure 2.3: Measurement setups for the (a) differential and (b) non-differential measurements. Reproduced from Weathers et al.[77]

with the resistors R_{DC} and $R_{DC,ref}$. The first lock-in amplifier is used to measure the AC voltage drop (v_h) across the heater, in the same was as was discussed previously for the non-differential measurement. A single AC voltage output from the second lock-in is supplied to both the sample and reference sensor PRT, with resistances of R_s and $R_{s,ref}$, respectively. The second and third lock-in amplifiers are used to measure the relative AC voltage drops on the sensing membranes, v_{s+b} and v_b, as shown in Figure 2.3b. In this notation, $s+b$ refers to the relative voltage drop across the serpentine and one supporting beam, and b refers to the relative voltage drop across one supporting beam. The reference signal for the third lock-in is the TTL (transistor-transistor logic) square pulse from the second lock-in, so that the second and third lock-ins are locked in frequency and phase. While the heating current is swept, the relative voltage rise in the sample sensing PRT relative to the reference sensing PRT is obtained as $v_s = v_{s+b} - v_b$. Because the thermal conductance across the suspended region is different for the sample, G_s, and reference device, $G_{s,ref}$, the

16

sensor PRT temperature rise will also differ, which results in a detectable signal in v_s. In particular,

$$\Delta v_s = i \frac{dR_s}{dT} \Delta T_s - i_{ref} \frac{dR_{s,ref}}{dT} \Delta T_{s,ref} \qquad (2.11)$$

where Δ refers to the voltage or temperature rise relative to zero heating, $I_{DC} = 0$ and $I_{DC,ref} = 0$. At the beginning of the measurement at each ambient temperature, $R_{AC,s,ref}$ is adjusted when $I_{DC} = 0$ and $I_{DC,ref} = 0$, so that $v_s = iR_s - i_{ref}R_{s,ref} = 0$. This ensures that if $\delta T_s \equiv \Delta T_s - \Delta T_{s,ref} = 0$, then $\Delta v_s = 0$, as long as $idR_s/dT = i_{ref}dR_{s,ref}/dT$. Furthermore, in order to ensure that equal DC heating is applied to the sample and reference heaters so that $\delta T_s = 0$ when $G_s = G_{s,ref}$, it is necessary to adjust I_{DC} and $I_{DC,ref}$ so that

$$\frac{I_{DC}}{I_{DC,ref}} = \left[\frac{G_{b1}G_{b2}}{G_{b1,ref}G_{b2,ref}} \frac{R_{h,ref} + \beta R_{b,ref}}{R_h + \beta R_b} \right]^{1/2} \qquad (2.12)$$

where G_{b1} and G_{b2} were defined previously for the non-differential measurement and are obtained by two non-differential measurements with reversed heat flow. The electrical resistances of the heater PRTs, R_h and $R_{h,ref}$, and the current carrying beams, R_b and $R_{b,ref}$, are measured in separate four-probe electrical measurements. The factor β describes the degree of radiation loss from the long supporting beams, and approaches 1 in the limit of no radiation loss.[77] With these two balancing requirements and the assumption that the background thermal conductance is the same on the sample and reference device, the measured temperature δT_s is the temperature rise due to conduction through the sample alone. The thermal conductance of just the sample, G_n, is then found from

$$G_n = G_{b2} \frac{\delta T_s}{\Delta T_h - \Delta T_s} \qquad (2.13)$$

This differential measurement method has been used to measure the thermal conductance of polythiophene[77,80] and polyacetylene[75] nanofibers in other reported works, and has been used to measure the thermal conductance of higher manganese silicide (HMS) nanostructures discussed in Chapter 4.

Four-Probe Thermoelectric Measurement Method

In addition to the intrinsic thermal resistance of the sample, R_s, there is also a contribution to the measured thermal resistance due to contact resistance at each membrane, R_{c1} and R_{c2}, as shown in the thermal resistance circuit in Figure 2.2b. This contact resistance is a result of both the interfacial thermal contact resistance across the sample/SiN or sample/metal interface, as well as a contact resistance associated with the internal thermal resistance of the SiN membrane. Because the internal thermal resistance of the membrane is about two orders of magnitude smaller than the combined thermal resistance of the six supporting beams, which is approximately $10^6 - 10^7$ K/W, the temperature distribution of each membrane is approximately uniform during the measurement as long as the sample resistance is similarly large.[81] In the case of low thermal resistance samples on the order of 10^6 K/W or less (i.e., $G_s > 1$ μW/K), this assumption of a uniform temperature distribution is no longer valid.

In order to determine the thermal contact resistance, a four-probe thermoelectric measurement method was previously developed by Mavrokefalos et al.[71] In this method, the thermal contact resistance of the sample is determined by measuring the difference in thermoelectric voltage between the inner and outer electrodes. The difference in thermoelectric voltage is proportional to the difference in temperature between these contact pads, as a direct result of interfacial contact thermal resistance and a non-uniform membrane temperature.

According to a fin temperature model, the temperature profile along the sample decays approximately exponentially in the area supported by the SiN membrane, and is approximately linear in the suspended segment when the radiation loss from the sample is negligible. The thermal contact resistance can be found from the fin resistance formula,

$$R_{c,i} = \frac{1}{\kappa A m \tanh m L_{c,i}} \qquad i = 1, 2 \qquad (2.14)$$

where κ is the thermal conductivity of the sample, A is the cross sectional area of the

suspended sample, and $L_{c,i}$ is the contact length between the sample and membrane as defined in Figure 2.2b. Because of the thermal contact resistance, the temperature drop across contacts 1 and 4 (outer electrodes) is larger than that between contacts 2 and 3 (inner electrodes). Likewise, the measured thermoelectric voltages, V_{14} and V_{23}, will differ by an amount that is related to the difference in temperature as,

$$\gamma = \frac{\gamma_{14}}{\gamma_{23}} = \frac{T_1 - T_4}{T_2 - T_3} = \frac{V_{14}}{V_{23}} \tag{2.15}$$

where

$$\gamma_{ij} = \frac{T_i - T_j}{T'_h - T'_s} = 1 + \frac{1 - \cosh m(L_{c,1} - L_i)/\cosh mL_{c,1}}{L_s m \tanh mL_{c,1}} \tag{2.16}$$
$$+ \frac{1 - \cosh m(L_{c,2} - L_i)/\cosh mL_{c,2}}{L_s m \tanh mL_{c,2}}$$

and T' is the temperature at the edge of the membrane, as defined in Figure 2.2b. Therefore, the Seebeck coefficient and intrinsic thermal resistance of the sample can be found from[71]

$$S = \frac{\alpha V_{23}}{\gamma_{23}(T_h - T_s)} \tag{2.17}$$

$$R_s = \frac{R_{total}}{\alpha} \tag{2.18}$$

where
$$\alpha = \frac{T_h - T_s}{T'_h - T'_s} = 1 + \frac{1}{L_s m} \left[\frac{1}{\tanh mL_{c,1}} + \frac{1}{\tanh mL_{c,2}} \right] \tag{2.19}$$

In practice, this method requires that the thermoelectric voltage between the two inner electrodes and between the two outer electrodes be measured simultaneously and that Eqs. (2.15 - 2.16) be solved numerically for m from the measured γ value at each temperature. Figure 2.4a shows the measured V_{14} and V_{23} as a function of $T_h - T_s$ for a thin film sample of poly(3,4-ethylenedioxythiophene) (PEDOT), which shows the deviation in the thermoelectric voltage between the two sets of contacts. This amounts to an R_c that is approximately 15% of the total measured thermal resistance, R_{total}.
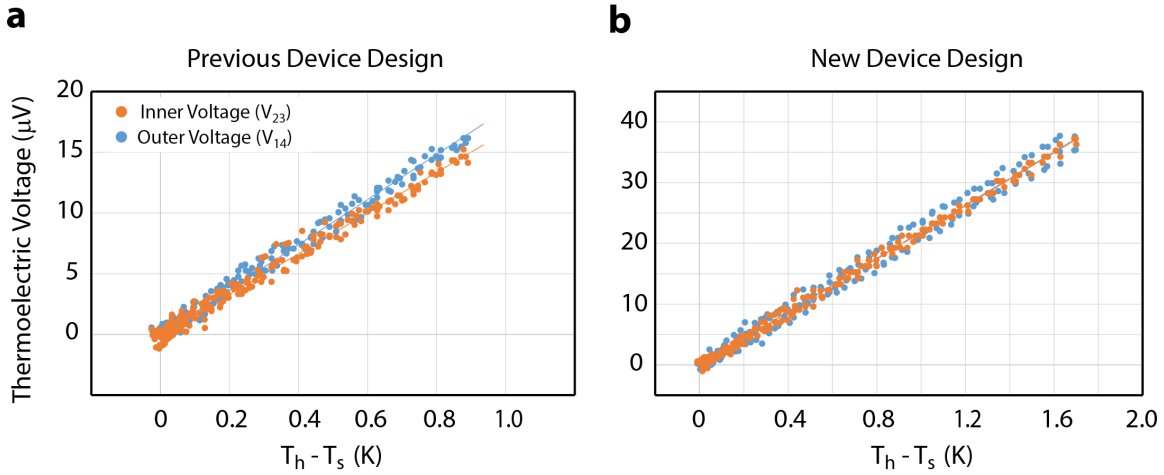
Figure 2.4: The thermoelectric voltage measured between the inner (orange) and outer (blue) electrodes on a (a) previous and (b) new device design.

Improved Device Design with Reduced Thermal Contact Resistance

The two-probe thermal conductance measurement relies on the assumption of a uniform temperature across the SiN membranes, which is only valid when the thermal resistance of the supporting beams and the sample are much greater than the internal thermal resistance of the membrane, which is approximately 10^5 K/W.[71] To address this concern, a new device has been designed and fabricated with reduced membrane thermal resistance, in order to decrease the contact thermal resistance in the measurement.[76] In the previous design, shown in Figure 2.1b, the 1 μm width electrodes were patterned next to the PRT, which occupies only a portion of the membrane. In the new design, shown in Figure 2.1c, the PRT takes up nearly the entire SiN membrane, which is reduced slightly in lateral size compared to the previous design. An 80 nm HfO_2 dielectric film is deposited by atomic layer deposition (ALD) through a photolithography mask on top of the PRT and the six supporting Pt/SiN beams on each membrane. Next, two Pd electrodes (yellow) are patterned on top of the HfO_2 on each membrane with photolithography and lift-off.

Because the serpentine heater occupies nearly the entire membrane surface,

the temperature distribution is expected to be more uniform compared to the previous design. In addition, the large Pd electrodes with relatively large thermal conductivity, act as lateral heat spreaders, which reduce the internal thermal resistance of the membrane even further. As a result, the thermal contact resistance measured by the four-probe thermoelectric method has been found to be smaller on the new devices for both conducting polymer thin films and semiconducting nanowires. For example, Figures 2.4a and 2.4b show the measured thermoelectric voltages of the inner and outer electrodes of a poly(3,4-ethylenedioxythiophene) (PEDOT) thin film sample measured on a previous device and a new device design, respectively. The sample on the previous device design (Figure 2.4a) has ~ 200 nm of Au deposited through a shadowmask onto the electrical contact pads to improve the electrical and thermal contact resistance, while the sample on the new device has no shadowmask deposition. Even without any additional metal deposition, the new device shows negligible thermal contact resistance determined from the difference between the thermoelectric voltage measured between the two inner electrodes and two outer electrodes.

2.1.2 Sample Preparation

Assembly of Samples on the Suspended Device

The placement of the nanowire or thin film sample on the suspended measurements device requires care to avoid damaging the sample. In the best case, the sample can be picked up from the growth substrate with a sharp tungsten tip and positioned across the measurement device. In this method, tungsten tips are electrochemically etched from thin tungsten wire in potassium hydroxide solution, and the alignment of the sample is done under an optical microscope by moving the tungsten tip with a manual xyz stage. This method introduces no contaminants or residue to the sample, and is able to achieve better than 1 μm alignment accuracy. However, this method is not feasible for many large area, conformal samples like graphene or polymer thin films, as the samples simply tear or fold during transfer. On the other hand, this method has been very successful in manipulating semiconducting nanowire samples,

21

in particular, the higher manganese silicide nanoribbons discussed in Chapter 4.

Alternatively, the sample can be transferred to the measurement device with the use of a polymer carrier layer, as shown in Figure 2.5.[76,82,83] In one such method, the sample can be patterned to the correct dimensions on the growth substrate with electron beam lithography or by mechanically cutting the sample with a tungsten tip. Then, 8% water soluble polyvinyl alcohol (PVA) is drop cast on the growth substrate, and is baked at 80 °C for approximately 1 minute. The PVA layer can then be peeled from the growth substrate with tweezers, which removes the sample attached to the PVA. The PVA carrier layer is then transferred on top of the measurement device with a drop of isopropanol and the sample is aligned to the device membranes with the help of a tungsten tip or tweezers. The PVA can then be dissolved by placing the entire device in water, which leaves just the sample suspended across the measurement platform.

Similarly, samples can be transferred onto a substrate composed of a bilayer of 1% PVA and 11% poly(methyl acrylate) (PMMA) each spin coated at approximately 6000 rpm. As long as the samples are well adhered to the top surface of the PMMA, the Si/PVA/PMMA substrate with the samples is placed in water to dissolve the PVA, which leaves the PMMA/sample layer floating on the top of the water. The PMMA/sample layer is flipped over and placed on top of the measurement device with a drop of water and aligned with the tungsten tip or tweezers. The PMMA can then be removed by placing the entire device in acetone or by baking the device in a tube furnace with argon and hydrogen at 350 °C.

Methods for Making Electrical Contact to Suspended Samples

In order to measure the thermal contact resistance between the sample and the membrane, the four-probe thermal conductance measurement method requires four electrical contacts to the sample in order to measure the inner and outer thermoelectric voltages. Unfortunately, making electrical contact to a suspended semiconducting

PMMA
PVA
Si

PVA
Si

dissolve PVA in water to
release PMMA/sample

peel PVA from the Si to
remove PVA/sample

align PMMA/sample
to the device

align PVA/sample
to the device

dissolve PMMA
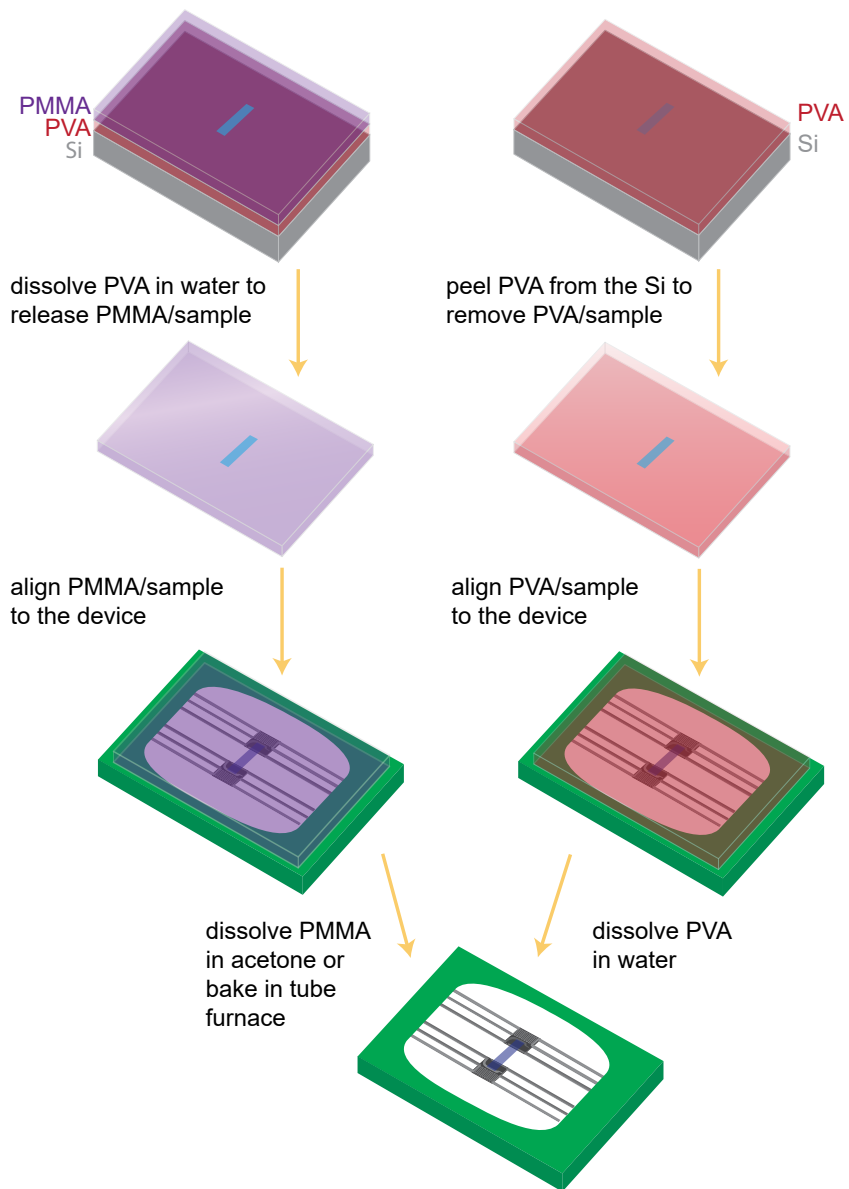in acetone or
bake in tube
furnace

dissolve PVA
in water

Figure 2.5: Procedure for placing a sample on the measurement device with a polymer
carrier layer. Reproduced from Weathers et al.[76]

nanowire or thin film can be exceedingly difficult because of native oxide or polymer residue on the sample surface. Devices with supported nanowires or thin films can easily be wet-etched, for example in hydrofluoric acid, to remove the native oxide before metal deposition. However, the etching of native oxide from a suspended sample can be much more challenging. Previous reports have used a focused Ga ion beam (FIB) or focused electron beam (FEB) to deposit Pt and Ni contacts on the suspended sample on the measurement device.[84] Under high enough accelerating voltages, the ion beam or electron beam can etch some of the native oxide, before deposition of metal. However, FIB deposition of Pt is known to spray Pt or Pt-C particles up to several microns outside the deposition area,[85] which can result in contamination of the sample with Pt particles or Ga ions, especially in the ~ 5 μm suspended region. An alternative method, which has been very successful for a limited number of materials, is *in situ* hydrogen or forming gas (5% hydrogen, 95% nitrogen) annealing of the sample during measurement. For example, a previous report has shown that electrical connection to Bi_2Te_3 nanowires and nanoplates could be obtained after annealing in forming gas at 480 K.[86,87] However, this method has not been demonstrated to be successful with other semiconducting materials.

Shadowmask deposition of metal through a SiN stencil has also been used to deposit Ti/Au contact pads on InAs nanowires following a brief reactive ion etch (RIE) exposure to BCl_3 plasma.[80] While this method has been moderately successful in achieving electrical contact to this material and improves the thermal contact resistance,[80] it has not successfully made electrical contact to silicon based nanowires. In addition, there is concern that RIE etching of a nanowire could introduce surface defects to the nanowire, which could affect the measured electrical properties.

Because of the limitations and complications in these methods, there has been a need for a robust technique to make electrical contact to a suspended nanostructure sample without introducing contaminates or additional defects to the sample. To address this need, a technique has been developed in this work to allow for reliable electrical connection to semiconducting nanowires and thin films with minimal

contamination of the sample.

A schematic of this method is depicted in Figure 2.6. First, a Si/SiO$_2$ wafer with Pt alignment marks patterned at regular intervals is coated with 6 nm of Ni by electron beam deposition. Following the Ni deposition, Pd contact pads with the exact dimensions of the Pd electrodes on the device are patterned on the substrate at regular intervals of 2 mm with electron beam lithography (EBL) followed by liftoff of 30 nm of Pd deposited by e-beam evaporation. A nanowire or thin film sample is transferred to the Pd contact pads on the Si/SiO$_2$/Ni substrate so that the sample bridges all four contact pads. For the case of higher manganese silicide nanowires that are grown on Si wafer chips, the nanowires can be picked up with a sharp tungsten tip and easily transferred to the Pd contact pads. For other samples that cannot be transferred with a tungsten tip, it is relatively straightforward to transfer and align the sample to the Pd contact pads with a sacrificial carrier layer as has been done for graphene[88] and polymer thin films[76] with a PMMA carrier film.

The substrate with the Pd contact pads and the sample is then spin coated with 4% PMMA and the area above the Pd contact pads is patterned with EBL, leaving the sample exposed just in the regions of the Pd contact pad. The native oxide on the sample can now be easily wet etched in hydrofluoric (HF) acid, or other etchant, followed immediately by metal deposition of $\sim$ 50 nm of Pd and liftoff in acetone. This leaves the sample sandwiched between two layers of Pd, with the top layer of Pd deposited without any native oxide on the sample. The substrate is then coated with 11% PMMA, which forms a thick carrier layer to transfer the sample to the measurement device. The Si/SiO2/Ni/Sample/PMMA substrate is placed in 10% hydrochloric (HCl) acid for approximately 20 minutes, which etches the sacrificial Ni layer and releases the sample/PMMA layer, which floats on the top of the solution. For samples that are not etched by HF, such as silicon or III-V semiconductor samples, the sacrificial Ni layer is not necessary, and HF etching can be used to etch the native oxide on the silicon wafer, which can serve the same role as the Ni sacrificial layer. Similarly, for samples which are easily etched by HCl, such as III-V semiconductors,
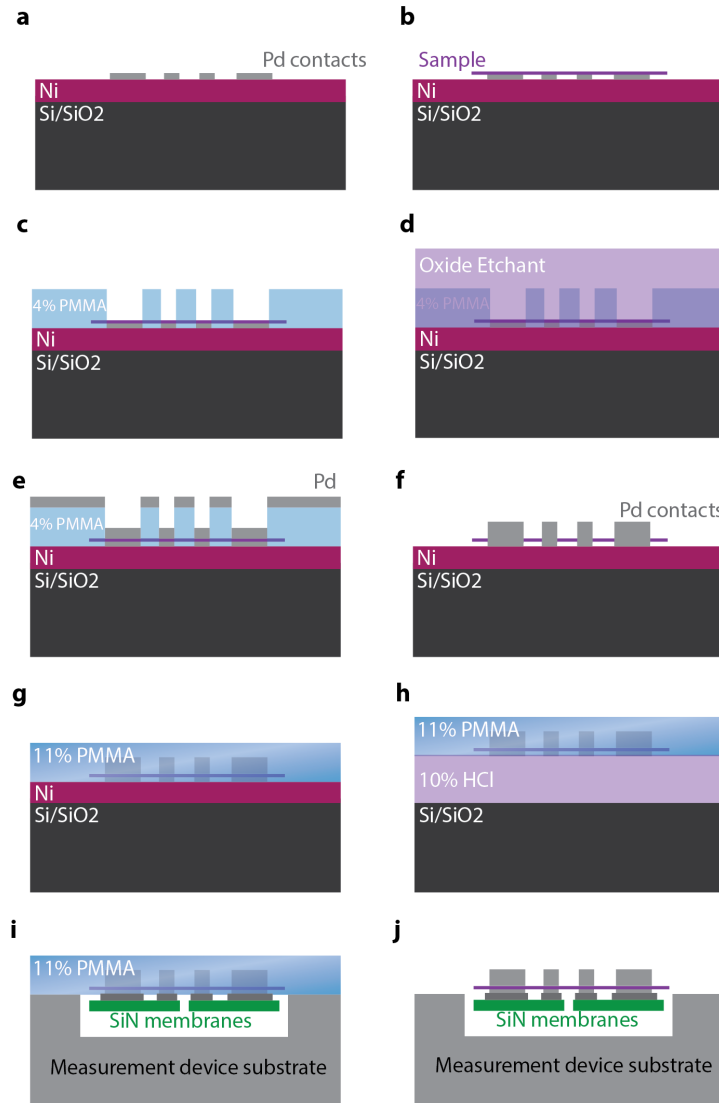
Figure 2.6: Procedure for the Pd contact method. (a) 30 nm thick Pd contacts are deposited on a Si/SiO$_2$/Ni substrate with electron beam lithography and e-beam deposition. (b) A sample is transferred to the Pd contacts, and (c) 4% PMMA is patterned with electron beam lithography to expose the sample in the area above the Pd contacts. (d) The device is placed in an oxide etchant to remove the native oxide on the sample, (e) followed immediately by metal deposition of 60 nm of Pd, (f) leaving the sample sandwiched between Pd contact pads. (g) The substrate is spin coated with 11% PMMA and (h) placed in 10% HCl to etch the sacrificial Ni layer. (i) The floating PMMA layer with the sample and Pd contacts is transferred to the measurement device and aligned to the Pd electrodes with a tungsten tip controlled by a manual xyz stage under an optical microscope. (j) The 11% PMMA is burned off at 350 °C in a tube furnace leaving just the sample and Pd contacts adhered to the suspended device.

26

the Ni layer must be replaced with a sacrificial layer that can be etched with an etchant that does not damage the sample.

The sample/PMMA layer is cleaned in water and transferred to the top of the device. The Pd contact pads are aligned to the Pd electrodes on the device with the use of the tungsten tip and a drop of water. As the residual water dries, the PMMA/sample layer is adhered to the device substrate. A brief ~ 30 second exposure to a hotplate at 180 °C further adheres the PMMA to the device so that it is permanently stuck. In the case of most inorganic semiconductors that are stable at high temperature, the device with the sample/PMMA layer is placed in an evacuated tube furnace with argon and hydrogen at a pressure of approximately 10 mT, and is heated to 350 °C to burn off the PMMA layer. This leaves just the sample with the Pd contacts adhered to the device membranes. Figure 2.1c shows a higher manganese silicide nanoribbon transferred to a measurement device with Pd contact pads (blue) that make electrical contact to the sample on top of the Pd electrodes.

In typical electrical property measurements, Ohmic contact to a semiconductor sample is often made by the deposition of an adhesion layer of Ti, Cr, In, Al, or W, which form low Schottky barriers with many semiconductors or form a conducting alloy interface. This is followed by a capping layer of Au to prevent oxidation. However, in this transfer method, the exposure to HCl or HF etchant could slightly etch the metal adhesion layer resulting in poor adhesion of the metal to the sample. Therefore, with the recipe described above, it is advisable that only a noble metal that is not etched by HCl or HF be deposited in the contact pad deposition. For the higher manganese silicide nanoribbons, the Pd deposition provides Schottky contact to the nanoribbon with a contact resistance on the order of 1 MΩ, which is sufficient for Seebeck and four-probe electrical conductivity measurements when care is given to amplifier loading errors. The two-probe and four-probe electrical I-V curves of a higher manganese silicide nanoribbon are shown in Figure 2.7, which indicates a Schottky barrier less than 1 V at the inner electrodes.
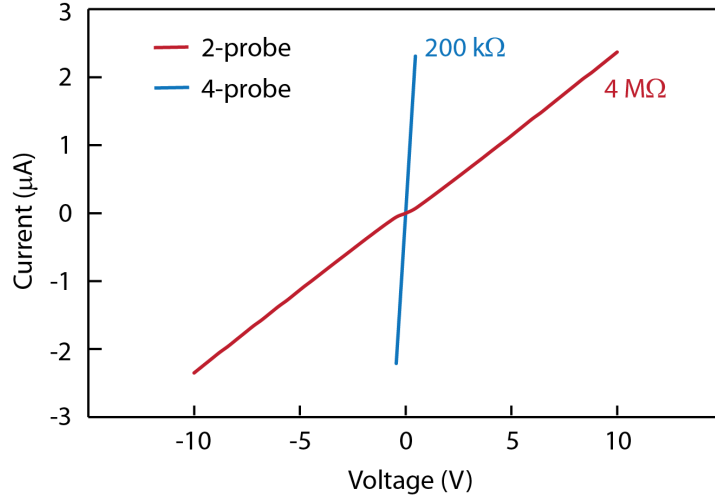
Figure 2.7: I-V curve for a higher manganese silicide nanoribbon after assembly by the Pd contact pad method. The red curve is the 2-probe resistance between the inner Pd electrodes, which shows a Schottky barrier smaller than 1 V, and the blue curve is the 4-probe resistance across the four Pd contacts.

2.2 Brillouin Light Scattering of Phonons and Magnons

In addition to characterizing the thermoelectric properties of a nanoscale systems, the fundamental dynamics and transport of energy carriers can be further investigated by optical spectroscopy techniques. For example, Raman spectroscopy has been used extensively to investigate the high frequency atomic vibrations in crystalline, amorphous, and molecular materials.[89–91] In crystalline materials, the Raman active modes are typically optical phonon modes which have energies on the order of THz, and are associated with the out-of-phase motion of ions within a unit cell. While first-order Raman scattering can be used to probe the zone center phonon modes, such as the graphene G-mode,[92] double resonant Raman scattering has been used to investigate the intervalley scattering of near zone boundary optical and acoustic phonons in graphite and graphene.[90,93] In many materials, the dominant heat carrying modes are intermediate frequency phonons, with energies on the order of 100 - 1000 GHz, although acoustic phonons with energies on the order of 10 - 100 GHz can also make important contributions to thermal transport. In addition, the transport of heat by

28

magnetic excitations, namely magnons, has been demonstrated by the large magnon thermal conductivity of some cuprate crystals.[62] Long wavelength magnons modes, like acoustic phonons, are also found in the GHz energy regime and can be important for heat transport in magnetic materials. Therefore, a method of probing low frequency modes in the GHz energy regime is an important tool in understanding heat transport in a variety of materials.

Brillouin light scattering (BLS) measures the inelastic scattering of light as a result of periodic modulations in the index of refraction in the presence of a magnon or phonon in the GHz energy regime. For the case of a phonon, periodic modulation of the lattice ions result in a periodic modulation in the polarization of the material through the acousto-optic effect. Similarly, for the case of magnons, the periodic modulation of the magnetization results in a change in the permittivity tensor through the magneto-optic effect.[94] An incident photon with a frequency ω_0 is inelastically scattered with a magnon or phonon, resulting in a loss (Stokes) or gain (Anti-Stokes) in photon energy associated with the phonon or magnon energy, ω. The inelastically scattered light can be collected and directed to an interferometer to resolve the associated frequency shift. The measured *intensity* of a given phonon or magnon peak is directly related to the occupation number of that particular mode, given by the equilibrium Bose-Einstein distribution function,

$$n = \frac{1}{e^{\hbar\omega/k_b T} - 1} \tag{2.20}$$

However, the temperature dependent frequency *shift* of a phonon or magnon mode is, in general, a function of the occupation of the entire distribution of phonon or magnon modes involved in heat transport, as a result of bond softening and anharmonic scattering between phonon modes as well as the temperature dependence of the saturation magnetization of the material. As a result, temperature dependent BLS has been used recently to investigate the local magnon and phonon populations in silicon, permalloy, glass, and yttrium iron garnet (YIG),[64–66,95] and to determine the nature of the coupling between magnetic and vibrational modes. This will be discussed further in Chapter 5.

2.2.1 Brillouin Light Scattering Experimental Setup

Tandem Fabry-Perot Interferometer

The detection of inelastically scattering light with MHz - GHz frequencies requires a more complicated spectrometer than the optical gratings commonly found in Raman or IR spectroscopy systems. To achieve a spectral resolution of better than 1 GHz, a Fabry-Perot interferometer is typically used. In the simplest Fabry-Perot interferometer, a pair of parallel mirrors, termed a cavity, is aligned at a spacing of L_1 with a partially reflective coating on the inner surfaces, as shown in Figure 2.8a. In an idealized system, the cavity acts as a filter in which only light that satisfies the constructive interference condition $L_1 = n\lambda/2$ is transmitted through the pair of mirrors, where n is an integer. In practice, the transmittance has some finite spectral width according to the Airy function,

$$T \sim \frac{1}{1 + \frac{4F^2}{\pi^2} \sin^2 \frac{2\pi L_1}{\lambda}} \tag{2.21}$$

The finesse, F, is a constant given by the quality of the mirrors, and is approximately 100. By scanning the mirror spacing, L_1, the transmitted intensity as a function of wavelength can be resolved. Figure 2.8c shows a characteristic spectrum from a single set of mirrors in a Fabry-Perot interferometer (FP1). The spacing between transmittance peaks, $\Delta\lambda$, is referred to as the free spectral range (FSR), while the linewidth of the transmitted peaks, $\delta\lambda$, is the instrument resolution, and is related to the finesse by $\delta\lambda = \Delta\lambda/F$. Because the measured intensity at a given mirror spacing is the sum of all wavelengths satisfying the constructive interference condition, a spectrum of interest, i.e. inelastically scattered light from a magnon or phonon, must fall entirely with one FSR to avoid ambiguity in the signal. However, with a single pair of mirrors, the FSR can only be increased by decreasing L_1, which also decreases the instrument resolution and the contrast, which scales as F.

In order to increase the FSR and contrast without decreasing the resolution, two tandem Fabry-Perot cavities (FP1 and FP2) can be employed with slightly different mirror spacings, L_1 and L_2, as shown in Figure 2.8b. In this configuration, light
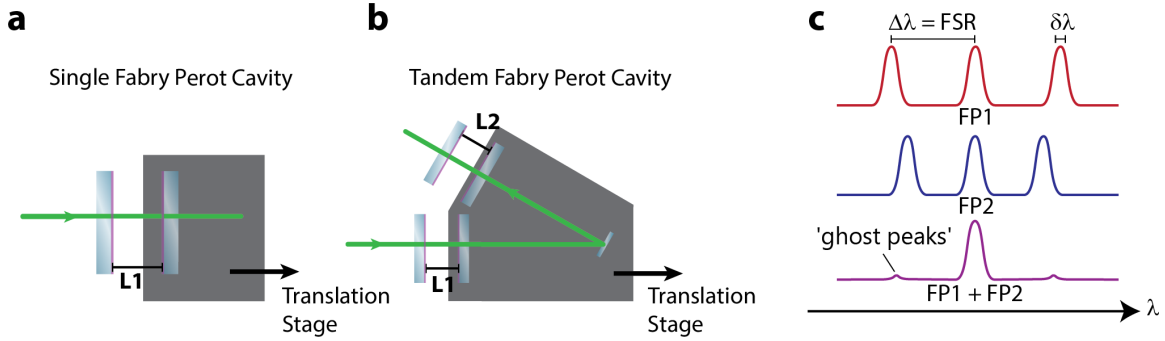
Figure 2.8: Illustration of the (a) single Fabry-Perot cavity and the (b) tandem Fabry-Perot cavity, with (c) representative spectra from each individual sets of cavities (FP1 and FP2) with different mirror spacing. The purple curve is the resulting spectrum from the tandem Fabry-Perot cavity.

must pass through both sets of mirrors with the simultaneous conditions $L_1 = n\lambda/2$ and $L_2 = m\lambda/2$, which is satisfied only at many multiples of the FSR of the first mirror pair, as shown in Figure 2.8c. Because the transmittance peaks of each set of mirrors is not a perfect delta function, there is some overlap of the transmitted peaks, which results in small "ghost peaks" occurring at the FSR of the first set of mirrors. These ghost peaks are sometimes visible in the recorded BLS spectra, and should not be confused with the inelastic scattering peaks.

The Fabry-Perot interferometer used in this work was acquired from JRS Scientific following the design of Dr. John Sandercock.[96] The Sandercock Fabry-Perot interferometer is a six pass interferometer, in which the scattered signal is passed through each set of mirrors three times, for a total of six cavity passes. In effect, this enhances the filtering effect of the cavities, resulting in higher contrast and resolution. The mirror spacing is scanned by moving a translation stage on which one set of mirrors is offset at an angle θ, so that the mirror spacing of FP1 and FP2 are different by $\cos\theta$. Following the six cavity passes, the light is directed through a pin-hole onto an avalanche photodiode (APD) single photon detector (Laser Components, BLUE Series).

Each set of mirrors is actively controlled by three sets of piezoelectric motors to control the alignment to sub-nanometer resolution, and to scan the mirror spacing, z. The alignment of the mirrors is facilitated by monitoring a weak reference signal that is sampled directly from the laser. At the beginning of each full scan of the mirrors, the detector monitors the reference peak for a brief amount of time, and the piezoelectric motors for the tip-tilt and z position of each pair of mirrors is adjusted to optimize the reference signal. With the default JRS Scientific hardware, this optimization is achieved through an analog control circuitry. After-market software provided by several research groups can provide more customized automation and control (e.g., the BrilliaNT software package from Prof. Dr. S. O Demokritov, Universität Münster). In addition to the active mirror control, the mirror cavities are mounted on top of an actively controlled vibration isolation stage (JRS Scientific, Table Stable). The active alignment of the mirrors and vibration isolation allow the system to remain at a stable operating condition for extended periods of time, even in the presence of minor external vibrations and temperature fluctuations. Nonetheless, there can be a noticeable drift in the signal over the course of an hour, which must be considered during long measurement acquisitions.

Optical System

The BLS system established in this work is composed of a micro-BLS (μ-BLS) system in the backscattering geometry, inspired by previous designs.[65,97] The most basic experimental setup is shown in Figure 2.9.

A single longitudinal mode, 200 mW, 532 nm solid state laser (Newport Physics, Excelsior) provides the probing beam for the BLS signal. First, the beam is sent through a spatial filter to remove all modes except the TEM00 mode, and to optimize the beam width, which is designed to be $\sim$ 2 mm. Approximately 1 mW is sectioned off with a beam sampler, to be used as the reference beam for the interferometer alignment. The horizontally polarized main beam is sent through a
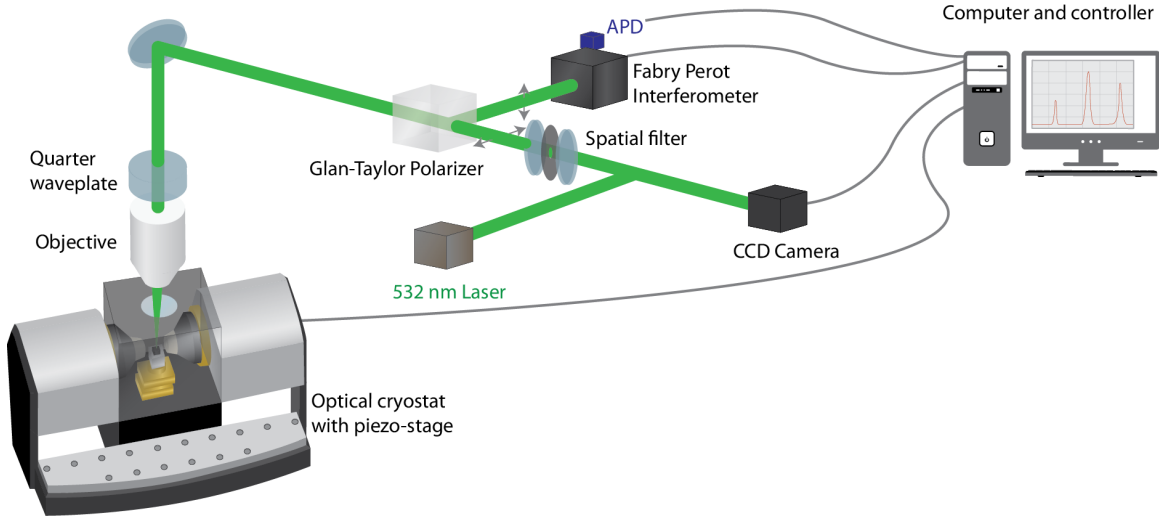
Figure 2.9: Experimental setup of the μ-BLS system established in this work.

Glan-Taylor polarizer (Thorlabs, GT15-A), which acts as a polarizing beam splitter. All of the horizontally polarized beam is allowed through the first pass of the Glan-Taylor polarizer and is focused on a sample surface through a 100x objective (Mitutoyo Plan Apo SL infinity corrected) with a working distance of 13 mm and a numerical aperture of 0.55. The polarization of the inelastically scattered light is either rotated by 90° upon interaction with a magnon, or rotated by 0° upon interaction with a phonon. The inelastically scattered light is then collected by the objective and redirected back through the Glan-Taylor polarizer, which splits the beam into horizontally polarized and vertically polarized beams. The vertically polarized beam, i.e., light that has undergone a 90° rotation, is directed through a 150 mm focal length lens into the interferometer input pin-hole for spectral analysis, while the horizontally polarized beam is sent to a charge-coupled device (CCD) camera for monitoring. In effect, this only allows inelastically scattered light that has been rotated by 90° to be collected by the interferometer, which greatly reduces the noise from the elastically scattered light which has not undergone a polarization rotation.

In order to sample the inelastically scattered light from phonons, which is not rotated by 90°, a quarter-waveplate is inserted just before the objective, which

effectively rotates the polarization by 90° upon two passes. This configuration collects both the inelastically scattered light from phonons as well as all the elastically scattered light, which can provide a strong background signal for highly reflective surfaces. Therefore, it is often necessary to tilt the sample to approximately 20° for phonon measurements, to remove a large contribution of this elastically backscattered light.

In order to probe low temperature excitations, the μ-BLS system also consists of a closed cycle helium cryostat (Montana Instruments) with an achievable temperature of $\sim 5 - 350$ K at a pressure better than 10^{-5} torr. The cryostat is equipped with an electromagnet with an achieveable magnetic field of up to 300 mT. The pole tips can be removed from the cryostat and can be used independently at room temperature. The sample stage inside the cryostat contains a closed loop piezoelectric xyz and rotation stage (Attocube, ANPx101 and ANR101) for nanometer precision alignment of the sample in four coordinates. The sample surface can be imaged during measurements with a white light source and a CCD camera (Sentech, MB33USB) to ensure that the laser spot is aligned to the correct location on the sample.

The analog controllers for the mirror spacing and mirror alignment are provided by JRS Scientific and interface with the control software through a USB connection. At the beginning of a measurement, the nominal mirror spacing of the first cavity, L_1, must be set by moving the translation stage with a geared motor attached to a dial gauge. The mirror spacing determines the FSR of the first mirror cavity according to FSR $= c/2L_1$, which must be chosen with consideration of the particular mode being probed. For example, for glass with a phonon peak at 33 GHz, an FSR of 40 GHz (mirror spacing of 3.7 mm) is sufficient to observe the peak near the edge of the first FSR. The inelastically scattered peak can also be probed in the second or third FSR in order to improve the signal to noise ratio from the strong elastic scattering peak. For example, in the case of glass, the 33 GHz signal could be observed in the third FSR if the mirror spacing is set to 10 mm with an FSR of 15 GHz. In this case, there will be two ghost peaks at 15 GHz and 30 GHz in addition to the phonon

peak at 33 GHz. The choice of FSR is a compromise between spectral resolution and signal quality, and is an important adjustable parameter in any BLS measurement.

Pressure Dependent Brillouin Light Scattering

The hydrostatic pressure dependence of the BLS spectrum has been used to study the effects of strain on the acoustic, optical and electronic properties of a variety of materials.[98–102] Often, this is achieved with the use of a diamond anvil cell,[103] in which the sample is sandwiched between two diamond anvils, which are compressed to increase the hydrostatic pressure of a gaseous medium surrounding the sample. While this method can achieve pressures on the order of 10 GPa or higher, low pressure measurements in the MPa regime are more problematic because of the difficulty in measuring the pressure accurately in this regime. Therefore, for low pressure measurements, a low-cost, straightforward apparatus has been designed in this work to measure the pressure dependent BLS signal from 0 to 40 MPa.

The sample is placed inside a high pressure cell with an 8 mm thick *c*-axis sapphire window (Rayotek, 1/4 NPT, 10k PSI), as shown in Figure 2.10. The sight glass cell is connected to a 6000 psi argon cylinder and the pressure delivered to the sight glass cell is adjusted with a single stage regulator. A pressure gauge (Honeywell, JAW10KGZ) is placed on the output side of the regulator to monitor the hydrostatic pressure delivered sample. The pressure cell can fit between the electromagnet pole tips in order to measure the magnon signal from a sample. A 532 nm laser is focused on the sample through the sapphire window and the scattered signal is collected with the objective and sent to the interferometer for analysis. The thick sapphire window attenuates the scattered signal by at least a factor 10, so that it is necessary to collect the signal for much longer to obtain a reasonable signal to noise ratio.

During long acquisition times, it necessary to perform a measurement sequence that can correct for any systematic drift in the mirror spacing over long periods of time due to thermal expansion of the mirror cavities. For example, previous measurements
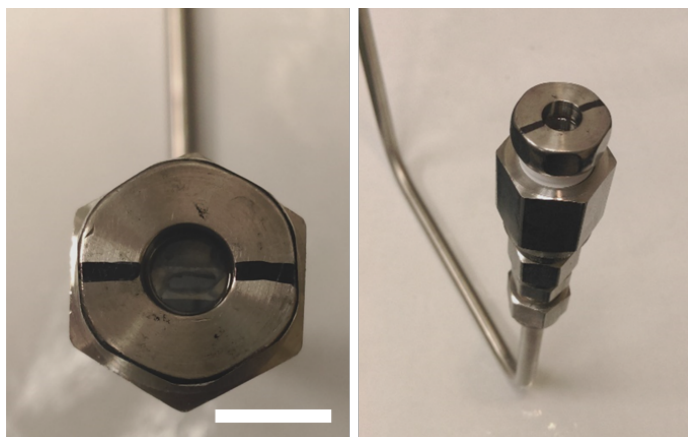
Figure 2.10: Sapphire window pressure cell for pressure dependent BLS measurements up to 40 MPa. The sample is placed just below the sapphire window, and the cell is connected to a 6000 psi Ar cylinder. Scale bar is 10 mm.

of the temperature dependence of the BLS signal have performed a measurement at zero temperature rise in between each high temperature measurement, in order to determine any drift in the signal over time.[66] Likewise, in the pressure dependent measurements, a measurement at zero gauge pressure is performed in between each high pressure measurement.

2.3   Inelastic Neutron Scattering

One standard method for determining the phonon and magnon dispersion is through inelastic neutron scattering (INS), in which the sample is bombarded with neutrons of constant energy. The resulting accumulation of energy and momentum loss of the scattered neutrons is used to determine the probability of a quasiparticle occurring with a given energy and momentum. INS requires a high energy particle accelerator, such as those found at Oakridge National Lab (ORNL) or the ISIS Neutron Source in the UK, and can take up to a week of continuous measurement time. Because of inherent limitations in the measurement resolution and signal-to-noise ratio due to limited sample size, scattering cross section, and accumulation time, INS

measurements are most enlightening when accompanied by density functional theory (DFT)/lattice dynamics simulations.

In a typical INS measurement, a single crystal sample with a volume on the order of or greater than 1 cm^3, is placed in the path of neutrons of constant energy. The spectral distribution of neutrons that scatter both elastically and inelastically with a phonon or magnon in the material are detected either with a time-of-flight technique or by Bragg reflection. The results are reported as the dynamic structure factor, $S(\mathbf{Q}, E)$, where $\mathbf{Q} = (q_x, q_y, q_z)$ is the momentum change and E is the energy lost or absorbed by the scattered neutron. S is a measure of the thermal fluctuations of a particle in a material, and is directly related to the probability of a neutron scattering with a quasiparticle of a given $(\mathbf{Q}, E)$. The function $S(\mathbf{Q}, E)$ is therefore a representation of the quasiparticle dispersion at finite temperature and finite linewidth.

A number of neutron scattering spectroscopy techniques are available to experimentalists, including the wide angular-range chopper spectrometer (ARCS) at ORNL, which provides the 4-dimensional scattering function $S(\mathbf{Q}, E)$ with a time-of-flight spectrometer, and the triple-axis spectrometer at ORNL, which provides the 2-dimensional scattering intensity $S(\mathbf{q_i}, E)$ for high energy modes at typically higher energy resolution than ARCS.

Understanding Inelastic Neutron Scattering Data

A neutron incident on a sample can scattering with a phonon mode, α, with a momentum exchange of $\mathbf{Q} = \mathbf{G_{HKL}} + \mathbf{q}$ and an energy exchange of E_α to the phonon, where $\mathbf{G_{HKL}}$ is the reciprocal lattice vector. The neutron scattering intensity is directly related to the dynamical structure factor, which is given by[50]

$$S(\mathbf{Q}, E) = \sum_\alpha \frac{1}{E_\alpha} F_\alpha(\mathbf{Q}, E)(n_\alpha + 1)\delta(E - E_\alpha)\delta(\mathbf{Q} - \mathbf{q} - \mathbf{G_{HKL}}) \qquad (2.22)$$

where F is the scattering function,

$$F_\alpha(\mathbf{Q}, E) = \left| \sum_i \frac{b_i}{\sqrt{m_i}} e^{i\mathbf{Q}\cdot\mathbf{r_i} - W_i} (\mathbf{Q}\cdot\mathbf{e}_i^\alpha) \right|^2 \qquad (2.23)$$

The summations are over all phonon modes, α, and all atoms, i, in the unit cell. The factors b_i, m_i, $\mathbf{e}_i^\alpha$, and $\mathbf{r_i}$ are the coherent neutron scattering length, the mass, the polarization vector and the atomic position of the ith atom and phonon mode α, and n_α is the Bose-Einstein distribution function. The Debye-Waller factor, W_i, is the thermally averaged displacement of the atoms from equilibrium, and provides a thermally induced spread to the data. While inelastic neutron scattering can occur through both coherent and incoherent processes, it is the coherent processes that contain the relevant information about collective excitations such as phonons or magnons. The incoherent scattering results from the scattering of a neutron with the same atom at a different position and time, which results in an unwanted, continuous background signal.

The first step in understanding the neutron scattering data is to understand the variations in the scattering intensities for a given $\mathbf{Q}$. In a typical measurement of the 4-dimensional $S(\mathbf{Q}, E)$ from the ARCS spectrometer at ORNL, the data spans multiple Brillouin zones, i.e. multiple $\mathbf{G_{HKL}}$. The Bragg peak at the center of each zone has a scattering intensity that depends on the static structure factor determined from powder diffraction measurements. Likewise, the inelastic scattering intensity from a particular Bragg reflection also scales with that static structure factor for modes close to the Bragg reflection. For higher energy modes, the intensity is dictated entirely by the dynamical structure factor, which is a more complicated function of the thermal fluctuations of the atoms. Therefore, it is first necessary to determine the Brillouin zones from which the greatest signal to noise ratio is achieved. This requires slicing $S(\mathbf{Q}, E)$ along the principle directions, $\mathbf{q} = [H00], [0K0], [00L]$, for all $\mathbf{G_{HKL}}$, to manually find the data with the best signal.

Furthermore, because S scales as $|\mathbf{Q}\cdot\mathbf{e}_i^\alpha|^2$, the strength of a particular phonon mode will depend on the Brillouin zone, $\mathbf{G_{HKL}}$, and the momentum transfer di-

rection, $\mathbf{q}$. At small wavevectors, the polarization vectors for the transverse and longitudinal phonon modes will be perpendicular and parallel to $\mathbf{q}$, respectively. At higher wavevectors, this condition does not necessarily hold, as the polarization of the mode becomes more complicated and $\mathbf{e}_i^\alpha$ is no longer constant. Therefore, in the low wavevector limit, the intensity of longitudinal modes will be greatest when $\mathbf{G_{HKL}}$ is mostly parallel to $\mathbf{q}$. Likewise, the intensity of transverse modes will be greatest when $\mathbf{G_{HKL}}$ is mostly perpendicular to $\mathbf{q}$. For example, a momentum transfer of $\mathbf{G_{HKL}} = (400)$ and $\mathbf{q} = [H00]$ yields a very strong scattering intensity for longitudinal acoustic modes, while $\mathbf{G_{HKL}} = (400)$ and $\mathbf{q} = [0K0]$ yields a strong scattering intensity for transverse acoustic modes polarized in the (110) direction. The presence of only certain polarizations for a given $\mathbf{G_{HKL}}$ and $\mathbf{q}$ is useful in isolating the polarization of a given mode.

In addition to the INS measured dynamical structure factor, the dynamical structure factor can also be simulated from the phonon dispersion determined from lattice dynamics simulation, in which the polarization vectors of the phonon modes fall out directly from the eigenvectors of the dynamical matrix. The dynamical structure factor can be solved from Eqs. (2.22 - 2.23) with the known values of the coherent neutron scattering length, the mass of the atoms, the calculated phonon energies and wavevectors, and the temperature. This method is employed in Chapter 4, Figure 4.2 to verify the INS results from a bulk higher manganese silicide crystal.

2.4   Summary

Three important developments in the measurements of thermoelectric properties of suspended nanostructure have been accomplished in this work to improve the measurement sensitivity, resolution, and uncertainty. First, a differential measurement method has been developed to remove the background thermal conductance due to residual gas molecules and radiation heat transfer, and to improve the measurement resolution by approximately an order of magnitude to 0.1 nW/K. In addition, a

new device design has been fabricated that improves both the electrical and thermal contact resistance to the sample, which is a crucial problem in thermal transport measurements. Furthermore, a new transfer technique allows for electrical contact to be made to suspended nanostructures on a microfabricated device to high yield, which is a problem that has plagued the suspended device measurement techniques since their inception. These advancements have allowed for high sensitivity measurements of a number of samples,[75–77,104] including the work discussed in Chapters 3 and 4.

Furthermore, a μ-BLS system has been established in this work to probe the transport and dynamics of magnetic and lattice excitations at variable temperature and hydrodynamic pressures. The thermoelectric property measurements on suspended nanostructures in combination with BLS spectroscopy of the microscopic dynamics allows for powerful analysis of the variety of mechanisms of energy carrier transport at the nanoscale.

Chapter 3

Electronic Thermal Transport in the Conducting Polymer poly(3,4-ethylenedioxythiophene)[1]

Since the development of conducting polymers in the 1970s[105,106] there has been continuous advancement in their use for organic light emitting diodes,[107] organic transistors,[108] memory storage,[109] solar photovoltaics,[110] and more recently thermo-electric applications.[15] Conducting polymers offer a number of advantages over inorganic materials including mechanical flexibility, transparency, and material abundance, which make their fabrication comparatively less costly and offer additional applications in printed and flexible electronics.[111,112] Conjugated polymers contain an unsaturated carbon backbone, which is π bonded, allowing for a delocalization of unpaired electrons along the polymer chain and high mobility charge transport. The charge carriers in conjugated polymer systems are polarons, which are fermionic quasiparticles composed of a charge and a geometrical distortion of the bonding. A pair of like charged polarons is termed a bipolaron, which carries no net spin.[113] By oxidizing (p-type doping) or reducing (n-type doping) the polymer backbone, the system can be doped to a wide range of conductivities. The ability to tune their electronic properties by over 10 orders of magnitude offers significant variability in the electronic transport mechanisms of conducting polymers, which can be tuned to be insulating, semiconducting or metallic. Such variability depends significantly

---

[1]The content of this chapter was published in A. Weathers, Z.U. Khan, R. Brooke, D. Evans, M.T. Pettes, J.W. Andreasen, X. Crispin, L. Shi. Advanced Materials 27, 2101-2106 (2015). The samples were synthesized by Z.U. Khan, R. Brooke, D. Evans, and X. Crispin. X-ray diffraction analysis of the samples was performed by J.W. Andreasen. A. Weathers and M.T. Pettes performed the suspended device fabrication. A. Weathers performed the sample assembly, thermoelectric property measurements, data analysis, and theoretical analysis. The manuscript was written by A. Weathers and L. Shi, and edited by all co-authors.

on the material microstructure and processing conditions,[114] and offers a wealth of possibilities for their electronic applications.

Conducting polymers are a low-cost and non-toxic alternative to the standard inorganic thermoelectric materials. In addition to their intrinsically low thermal conductivity, conducting polymers also offer greater mechanical flexibility for use in non-planar and flexible thermoelectric modules, such as wearable electronics.[115] Furthermore, the synthesis of conducting polymers by solution processing and roll-to-roll production, is generally easier and cheaper than some of the high-cost, low-throughput fabrication methods of nanostructured inorganic materials.[116]

Because of these advantages, conducting polymers have recently become an active area of research within the field of thermoelectrics.[15,116] While conjugated polymer systems such as polyaniline, polypyrrole, and polycarbazole compounds have all been investigated for their thermoelectric properties,[117–119] poly(3,4-ethylenedioxythiophene) (PEDOT) has been demonstrated to be one of the best organic thermoelectric materials in recent years through precise engineering of the doping chemistry.[120–122] A recent report[121] has shown that PEDOT:Tosylate (PEDOT:Tos) thin films spin coated on insulating substrates can achieve a power factor, $S^2\sigma$, of 300 $\mu W\,m^{-1}\,K^{-2}$, which is only one order of magnitude lower than Bi_2Te_3. Similarly, PEDOT:polystyrene sulfonate (PEDOT:PSS) films have been found to have a similarly large power factor of 469 $\mu W\,m^{-1}\,K^{-2}$ at optimal doping concentration.[122] While inorganic semiconductors typically display a decrease in Seebeck coefficient with increasing electrical conductivity as a result of increasing carrier concentration, PEDOT:Tos films with a semi-metallic electronic structure have recently been shown to have the opposite trend due to a strong energy dependence of the density of states in this regime.[120] In that work, a maximum Seebeck coefficient of 55 $\mu V\,K^{-1}$ was found for the highest electrical conductivity of 1500 $S\,cm^{-1}$, corresponding to a power factor of 454 $\mu W\,m^{-1}\,K^{-2}$.

The thermoelectric figure of merit, zT, of conducting polymers is not yet competitive with the best inorganic systems. However, a zT value of 0.4 has recently been reported for PEDOT:PSS thin films, which is the highest reported value to date

for PEDOT.[122] The highest zT sample in that work was found to have an electrical conductivity of $900\,\mathrm{S\,cm^{-1}}$, a Seebeck coefficient of $73\,\mu\mathrm{V\,K^{-1}}$, and an in-plane thermal conductivity of $0.34\,\mathrm{W\,m^{-1}\,K^{-1}}$. Interestingly, the in-plane thermal conductivity was found to be nearly independent of electrical conductivity, which raises the question of how much heat is actually conducted by charge carriers in such a highly complex conducting polymer system. While the theory of electronic thermal transport in simple inorganic semiconductors and metals are relatively well known from the Wiedemann-Franz law, $\kappa_e = (k_b/q)^2 L\sigma T$, where k_b is the Boltzmann constant, q is the electronic charge, and L is the dimensionless Lorenz number equal to $\pi^2/3$ for a metal,[123] the theory of electronic thermal transport in complex conducting polymer systems is not well studied. Two previous measurements of the thermal conductivity of polyacetylene (PA) and polyaniline (PANI) films have found an increase in κ with σ,[124,125] however more complicated composite systems have not been studied because of the challenges in performing thermal conductivity measurements of conducting polymers, which have inherently low thermal conductivity and are often prepared as thin films on insulating substrates.

While the in-plane electrical conductivity and Seebeck coefficient can be readily obtained by depositing four-probe connections to a spin-coated PEDOT film, the measurement of the in-plane thermal conductivity of thin films requires more elaborate fabrication methods or more novel measurement procedures than electrical measurements. Furthermore, the transport properties of some conducting polymer systems like PEDOT can be highly anisotropic. PEDOT is typically synthesized by mixing ethylenedioxythiophene (EDOT) monomers with the charge countering ions PSS or Tos. The solution is then spin coated on a substrate either before or after polymerization, which results in a layering of PEDOT-rich and counterion-rich regions.[126] As a result, the electrical conductivity can vary by as much as three orders of magnitude between the in-plane and out-of-plane directions. Therefore, it is crucial to measure the thermal conductivity along the same transport direction as the electrical properties, in order to obtain an accurate zT along that direction.

One method for probing the in-plane thermal conductivity of anisotropic thin films is a modification of the 3ω method. In this modified method, a dielectric film such as SiN of Al_2O_3 is deposited on the thin film sample, and a gold metallic heater line is fabricated on top of the dielectric. While the 3ω voltage signal from the heater line yields the out-of-plane thermal conductivity of the thin film, $\kappa_\perp$, by varying the heater line width, it is possible to extract the ratio of the out-of-plane to in-plane thermal conductivity, $\kappa_\perp/\kappa_{//}$, from a two-dimensional (2D) analytical expression for the temperature distribution.[127] Previous reports of the in-plane thermoelectric properties of PEDOT thin films have relied on this method, which has yielded a $\kappa_\perp/\kappa_{//}$ ratio of approximately 1.5 for PEDOT:PSS samples and 1.11 for PEDOT:Tos films.[121,122] However this method requires measuring the electrical and thermal properties on samples that have undergone different processing conditions, which can have dramatic effects on the morphology and electrical properties of conducting polymers. In addition, while the modified 3ω method has been developed to measure the in-plane thermal conductivity of anisotropic, homogenous films such as polyimide[127] and muscovite mica sheets,[128] its validity has not been tested for anisotropic films with layered, inhomogenous structures of counterion and PEDOT rich lamellas. Therefore, an accurate measurement of the transport properties along the same in-plane direction on the same sample is crucial to understanding the applicability of the Wiedemann-Franz law in this and other conducting polymer systems, which is a fundamental question that is both timely and important for the development of organic electronic, optoelectronic, and thermoelectric materials.

3.1 Theory of Electronic Thermal Transport

For a bulk semiconductor with a single parabolic band, the charge and energy current densities, J_q and J_E, in the absence of lattice thermal conduction can be

expressed as

$$J_q = -L_{11}\frac{\nabla \mu}{q} - L_{12}\nabla T \tag{3.1}$$

$$J_E = -L_{21}\frac{\nabla \mu}{q} - L_{22}\nabla T \tag{3.2}$$

where μ is the electrochemical potential and L_{ij} are the phenomenological coefficients. The first term in Eq. (3.1) represents the charge carried by electrons (or holes) as a result of a gradient in their electrochemical potential – i.e., Ohms law. The second term represents the charge carried by electrons or holes diffusing along a temperature gradient – i.e., the thermoelectric effect. The energy current density (Eq. 3.2) is also composed of a Peltier heat term, and a term associated with the transport of energy as a result of charge carrier diffusion along a temperature gradient. The phenomenological coefficients can be expressed as a function of the band structure of the material for an isotropic, parabolic band according to[129]

$$L_{11} = -\frac{q^2}{3}\int v^2\tau\frac{\partial f_0}{\partial E}D(E)\,\mathrm{d}E \tag{3.3}$$

$$L_{12} = \frac{q}{3T}\int (E-E_F)v^2\tau\frac{\partial f_0}{\partial E}D(E)\,\mathrm{d}E \tag{3.4}$$

$$L_{22} = \frac{1}{3T}\int (E-E_F)^2 v^2\tau\frac{\partial f_0}{\partial E}D(E)\mathrm{d}E \tag{3.5}$$

where $D(E)$ is the electronic density of states, τ is the relaxation time of electrons or holes, v is the electron or hole group velocity, f_0 is the equilibrium Fermi-Dirac distribution, and E_F is the Fermi level. The Onsager reciprocity for L_{ij} requires that $L_{21} = TL_{12}$. The common transport coefficients, σ, S and κ_e, can be expressed as function of these phenomenological constants as

$$\sigma \equiv L_{11} \tag{3.6}$$

$$S \equiv L_{12}/L_{11} \tag{3.7}$$

$$\kappa_e \equiv L_{22} - L_{21}S \tag{3.8}$$

The origin of the definition of the Peltier coefficient, $\Pi = ST$, from the Onsager reciprocity relation is now clear from Eq. (3.7). The electronic thermal conductivity

of a single charge carrier type, κ_e, is composed of a term associated with the diffusion of charge carriers along a temperature gradient minus the heat generated by the Peltier effect. Occasionally, the transport coefficients are expressed as functions of the so-called transport integrals, K_i,[130]

$$\sigma = \frac{q^2}{T} K_0 \tag{3.9}$$

$$S = \pm \frac{1}{qT} \left(E_F - \frac{K_1}{K_2} \right) \tag{3.10}$$

$$\kappa_e = \frac{1}{T^2} \left(K_2 - \frac{K_1^2}{K_0} \right) \tag{3.11}$$

where

$$K_s = \frac{8\pi}{3} \left(\frac{2}{h^2} \right)^{3/2} (s + 3/2) \, (k_b T)^{s+3/2} \, (m^*)^{1/2} \, T\tau F_{s+r+1/2}(\zeta) \tag{3.12}$$

and m^* is the electron effective mass, F_n is the Fermi-Dirac integral, $F_n(\zeta) = \int x^n (e^{x-\zeta} + 1)^{-1} \, dx$, and $\zeta = E_F/k_b T$. The $\pm$ in Eq. (3.10) is for holes ($+$) and electrons ($-$).

The relaxation time for charge carriers in Eq. (3.12) originates from the collision integral in the Boltzmann transport equation (BTE),

$$\left(\frac{df}{dt} \right) = \left(\frac{\partial f}{\partial t} \right)_{diffusion} + \left(\frac{\partial f}{\partial t} \right)_{forced} + \left(\frac{\partial f}{\partial t} \right)_{collision} \tag{3.13}$$

The collision term is strictly calculated from Fermi's Golden Rule, but is often approximated by the linearized relaxation time approximation,

$$\left(\frac{\partial f}{\partial t} \right)_{collision} = -\frac{f - f_0}{\tau} \tag{3.14}$$

There may be many scattering processes that contribute in parallel to τ, and they may each be complicated functions of energy. Nonetheless, τ can often be expressed by a power law relationship, $\tau = \tau_0 (E/k_b T)^r$, where r depends on the dominant scattering mechanism for charge carriers. For example, for acoustic deformation potential scattering, $r = -1/2$, while for ionized impurity scattering $r = +3/2$.[130,131]

The ratio of the electronic thermal conductivity to the electrical conductivity for a single band represents the ratio of energy to charge carried by the electrons or

holes, and is given by

$$\frac{\kappa_e}{\sigma} = \frac{1}{q^2 T} \left(\frac{K_2}{K_0} - \frac{K_1^2}{K_0^2} \right) \tag{3.15}$$

This relationship is often expressed as the Wiedemann-Franz law,[132,133] which takes the simple form

$$\frac{\kappa_e}{\sigma} = \left(\frac{k_b}{q} \right)^2 LT \tag{3.16}$$

where L is the dimensionless Lorenz number, which is also a function of the transport integrals. The Wiedemann-Franz law in its original form was reported by Wiedemann and Franz for metallic systems, in which L was found be constant for a number of common metals. In this limit of degenerate metallic conduction, L takes the value of $\pi^2/3$, which is termed the Sommerfeld value.[132] This is derived by considering the limit of a degenerate metallic system, in which the Fermi level is well within the conduction or valence band for electrons or holes, respectively, and the Fermi-Dirac integrals can be expressed as the convergent series

$$F_n(\zeta) = \frac{\zeta^{n+1}}{n+1} + n\zeta^{n-1} + O(\zeta^{n-2}) + ... \tag{3.17}$$

Only the first two terms are needed to calculate the Lorenz number from Eq. (3.15), which is found to be independent of the scattering parameter, r,

$$\frac{\kappa_e}{\sigma} = TL_0 \left(\frac{k_b}{q} \right)^2 = T \left(\frac{\pi^2}{3} \right) \left(\frac{k_b}{q} \right)^2 \tag{3.18}$$

Presently, the term "Wiedemann-Franz law" is sometimes used to describe a general linear dependence of κ_e/σ with T, with a Lorenz number that may be vastly different than the metallic limit. For example, in the non-degenerate limit when the Fermi level is inside the band gap and sufficiently far from the band edge ($\zeta << 0$), the Fermi-Dirac integral can be approximated as an exponential and the general expression for the Lorenz number of a single parabolic band can be expressed as

$$L = \left(r + \frac{5}{2} \right) \left(\frac{k_b}{q} \right)^2 \tag{3.19}$$

Even for metals, there can be deviations in the Lorenz number from low to high temperatures. The expression in Eq. (3.18) has assumed that the relaxation times for electron energy relaxation (heat transport) is the same as the relaxation time for electron momentum relaxation (charge transport). At very low temperatures when the dominant scattering mechanism is elastic impurity scattering, this is indeed the case, and $L = L_0$. Similarly, at high temperatures relative to the phonon Debye temperature (typically $200 - 300$ K for common metals), the dominant scattering mechanism for electrons is large-angle inelastic scattering with phonons of relative large wavevectors compared to the Fermi wavevector, k_F. This results in a large relaxation of both electron energy and momentum, recovering the limit of $L = L_0$. However, at intermediate temperatures, the phonon wavevector can be small compared to k_F, and small-angle scattering with phonons results in greater electron energy relaxation compared to momentum relaxation. In this case, L_0 can be scaled by the ratio of the energy to momentum relaxation lengths, $L_0(\ell_e/\ell_m)$, which tends to drop off at temperatures around 25% of the Debye temperature.[123]

Besides the deviations in L for metals, semiconductors can show substantial deviations in the value of L and in the temperature dependence of κ_e/σ predicted by Eqs. (3.18 - 3.19). For example, in systems where two bands (holes and electrons) can contribute to transport, the total electronic thermal conductivity, κ_E, is composed of three terms

$$\kappa_E = \kappa_e + \kappa_h + \frac{\sigma_e \sigma_h}{\sigma_e + \sigma_h}(S_e - S_h)^2 T \qquad (3.20)$$

The first two terms are simply the energy carried by each set of charge carriers given by the single band expression, while the third term is the bipolar contribution associated with the Peltier heat carried by electron hole pairs. This term is proportional to the energy difference between the bands,[129] and is most evident in the regime of intrinsic conduction, such as at high temperatures. This additional term can result in a larger Lorenz number than predicted by Eq. (3.19). For example the bipolar contribution can increase the apparent Lorenz number by as much as a factor of 10 in intrinsic Bi_2Te_3.[87,134] Moreover, complex one-dimensional systems with strong

electron-electron interactions, such as materials that behave as Luttinger liquids, can display large deviations in the value and temperature dependence of the Lorenz number.[135–138] Such behavior of highly correlated systems is not expected to be relevant for the PEDOT samples studied here, which have a small degree of crystallinity, a three-dimensional structure, and no signature power law dependence of the current with voltage.[137] Nonetheless, deviations in the value and temperature dependence of the Lorenz number are not unusual, particularly for more complex systems with anisotropic properties and unusual conduction mechanisms.

In addition to the Wiedemann-Franz law, the Mott formula for the thermopower can also be derived from Eq. (3.7) for a system of non-interacting electrons with a single, parabolic band. When a temperature gradient is applied to a conductor, the charge carriers on the hotter side will have a greater occupation of higher energy states compared to the cold end. As a result, hot energy carriers will diffuse from the hot end to the cold end, producing entropy on the order of k_b/q. Meanwhile, charge carriers from the cold end diffuse to the hot end as a result of this build-up of charge on the cold end. The net current generated by this charge carrier diffusion as a result of a temperature gradient is precisely the term $L_{12}\nabla T = \sigma S \nabla T$ in Eq. (3.1). More fundamentally, in the high temperature limit, the expression for the Seebeck coefficient in Eq. (3.10) is approximately E_F/qT, which is related to the thermodynamic identity for entropy, s, as

$$\frac{E_F}{qT} = -\frac{1}{q}\left(\frac{\partial s}{\partial N}\right)_{E,V} \tag{3.21}$$

In other words, the Seebeck coefficient is approximately the entropy carried per carrier in the presence of a temperature gradient. The magnitude of the net charge current, $J = \sigma S \nabla T$, depends on the difference in the energy dependent conductivity of high energy carriers versus low energy carriers. The expression for the electrical conductivity, Eq. (3.3), suggests that this difference could be due to a difference in the density of states, the scattering rate, or the group velocity. The effect of these properties on the Seebeck coefficient can be more easily understood by expressing the

Seebeck coefficient as a function of the charge carrier energy. The Seebeck coefficient from Eq. (3.7) can be written explicitly as

$$S = \frac{1}{qT} \frac{\int \tau v^2 \frac{\partial f_0}{\partial E} D(E)(E - E_F) \mathrm{d}E}{\int \tau v^2 \frac{\partial f_0}{\partial E} D(E) \mathrm{d}E} \tag{3.22}$$

Substituting for the definition of σ from Eq. (3.3) in the denominator gives

$$S = \frac{k_b}{\sigma q} \int \frac{E - E_F}{k_b T} \tilde{\sigma}(E) \frac{\partial f_0}{\partial E} \mathrm{d}E \tag{3.23}$$

where the spectral conductivity, which is equivalent to the transmission coefficient in the Landauer formalism, is given by

$$\tilde{\sigma}(E) = q^2 \tau v^2 D(E)/3 \tag{3.24}$$

so that

$$\sigma = \int_0^\infty \tilde{\sigma}(E) \frac{\partial f_0}{\partial E} \mathrm{d}E \tag{3.25}$$

Eq. (3.23) is known as the general Mott formula.[139] For a degenerate system, where transport occurs close to the Fermi energy, $\partial f_0/\partial E$ is only non-negligable within a few $k_b T$ of E_F. Therefore, a first order Sommerfeld expansion of Eq. (3.23)[140] i.e. taking $\tilde{\sigma}(E) \approx \tilde{\sigma}(E_F) + \tilde{\sigma}`(E_F)(E - E_F) + ...$ yields,

$$S = \frac{1}{qT} \frac{\pi^2}{3} (k_b T)^2 \left. \frac{\sigma'}{\sigma} \right|_{E_F} \tag{3.26}$$

With the identity $\dfrac{\sigma'}{\sigma} = \dfrac{d}{dx} \log \sigma$, this gives the familiar Mott-Cutler formula for the metallic thermopower,[141]

$$S = \frac{1}{qT} \frac{\pi^2}{3} (k_b T)^2 \left. \frac{d \log \sigma}{dE} \right|_{E_F} \tag{3.27}$$

Evidently, the Seebeck coefficient scales with the derivative of the conductivity with respect to energy at the Fermi level. In other words, a sharply peaked, asymmetric conductivity (or transmission function) at the Fermi level will yield the highest thermopower. When the energy dependence in $\tilde{\sigma}$ is dominated by the energy dependence

in the density of states, $D(E)$, the Seebeck coefficient can be designed to be large by tuning the Fermi energy to a region of rapidly varying $D(E)$. Likewise, the energy dependence in $\tilde{\sigma}$ can also originate from a strong energy dependence of the relaxation time, τ, or the group velocity, v, which scales as $\sqrt{E}$ in the vicinity of a parabolic band.

On the other hand, for a non-degenerate semiconductor, the Seebeck coefficient of holes for a single, parabolic band can be expressed as

$$S = \frac{k_b}{q} \left[\frac{(r + 5/2)\, F_{r+3/2}(\zeta_h)}{(r + 3/2)\, F_{r+1/2}(\zeta_h)} - \zeta_h \right] \tag{3.28}$$

where ζ_h is the reduced Fermi level for holes measured from the valence band. The dependence of the Seebeck coefficient on the energy dependence of the scattering processes is again evident in Eq. (3.28).

3.2 Sample Growth and Fabrication

The synthesis of PEDOT:Tos and PEDOT:PSS thin films were performed by Zia Ullah Khan and Xavier Crispin from Linkping University and Robert Brooke and Dr. Drew Evans at the University of South Australia.[76] Vacuum vapor phase polymerization (VVPP) of PEDOT:Tos films were prepared from a mixture of 40 wt% Fe-Tosylate in butanol, the triblock copolymer poly(ethylene glycol-propylene glycol-ethylene glycol) (PEG-PPG-PEG), and ethanol. This solution was spin coated on a glass substrate and exposed to EDOT vapor in vacuum.[142,143] The VVPP PEDOT:Tos samples were released from the substrate while cleaning in ethanol. Chemically polymerized (ChP) PEDOT:Tos films were prepared from a mixture of Fe-Tosylate, EDOT, and pyridine, which was spin coated on a glass substrate and baked at 100 °C for five minutes and cleaned in butanol and water. PEDOT:PSS films were prepared from a mixture of 5 wt% dimethyl sulfoxide (DMSO) and 1.2 wt% silquest together with a PEDOT:PSS suspension. The solution was spin coated on a glass substrate and baked at 120 °C for five minutes. The PEDOT:Tos samples were spin coated before the polymerization step, so no polymer chains existed during spin

coating. Therefore, anisotropy in the polymer chain alignment is expected to be less severe than if polymerization occurred before spin coating. However, anisotropy in the VVPP PEDOT:Tos samples can still arise from the structure directing behavior of the PEG-PPG-PEG additive in the spin coated mixture, which is used to template the polymerization.

The placement of the PEDOT films on the measurement devices was achieved with a polymer carrier layer as discussed in Chapter 2. First, a piece of the sample, with lateral dimensions of approximately 20 μm, was removed from the growth substrate with either a razor blade or tweezers. Then, two different transfer methods were employed to ensure that each method did not result in pronounced change in the transport properties. Both methods are depicted in Figure 2.5 in Chapter 2. In the first method, the sample was placed on a Si/PMMA/PVA substrate. The PVA was dissolved by placing the substrate in water, releasing the PMMA/sample layer. The PMMA/sample carrier layer was transferred to the measurement device, as discussed in Chapter 2. Then, the PMMA was removed by placing the sample in acetone. In the second method, the sample was placed on a clean Si wafer and 8% PVA solution was drop cast onto the substrate and baked at 80 °C. The PVA was peeled from the Si substrate, which released the PEDOT film from the Si substrate. The PVA carrier layer carrying the sample was then transferred to the measurement device, and was dissolved by placing the measurement device in water.

Nine samples were prepared from either the VVPP PEDOT:Tos, ChP PE-DOT:Tos, or PEDOT:PSS growth methods using both transfer techniques. The samples were transferred to both the older and newer device designs, as discussed in Chapter 2 and shown in Figure 3.1 of this chapter. The newer device designs have serpentine platinum resistance thermometers that cover nearly the entire membrane area, thus reducing the contribution from thermal contact resistance. In addition, the larger Pd electrodes make it easier to achieve electrical contact to the sample. Because the older device design has smaller electrodes and generally larger thermal contact resistance, an additional Au layer was deposited on the electrodes through

Table 3.1: Summary of polymerization method, dimensions, device type, carrier layer, and number of supporting bars for the nine PEDOT samples studied in this work. Reproduced from Weathers et al.[76]

Symbol	Dopant and Polymerization Technique	Dimensions			Device Type	Carrier Layer	# of Bars
		w (μm)	L (μm)	t (nm)			
▼ S1	VVPP PEDOT:Tos	5.9 ± 0.3	15.0 ± 0.1	167 ± 5	Old	PMMA	1
★ S2	VVPP PEDOT:Tos	5.8 ± 0.5	15.6 ± 0.2	130 ± 10	New	PVA	0
◄ S3	VVPP PEDOT:Tos	6.0 ± 0.5	12.0 ± 0.2	130 ± 10	New	PVA	0
♦ S4	ChP PEDOT:Tos	6.4 ± 0.3	13.6 ± 0.3	135 ± 10	New	PMMA	0
► S5	ChP PEDOT:Tos	8.5 ± 0.3	14.2 ± 0.1	130 ± 10	New	PMMA	0
● S6	VVPP PEDOT:Tos	6.9 ± 0.6	14.4 ± 0.4	167 ± 5	New	PMMA	0
■ S7	VVPP PEDOT:Tos	8.7 ± 0.3	14.4 ± 0.6	165 ± 20	Old	PMMA	2
▲ S8	PEDOT:PSS	10.4 ± 0.5	10.4 ± 0.5	230 ± 10	Old	PMMA	1
● S9	VVPP PEDOT:Tos	4.8 ± 0.2	11.5 ± 0.2	130 ± 10	New	PVA	0

a SiN shadowmask to improve the electrical and thermal contact resistance. In addition, three of the samples (S1, S7, S8) contained one or two supporting SiN bars across the suspended region. The $\sim 1\ \mu$m thick bars were added in the device fabrication procedure to improve the rigidity of the device during exposure to liquid solvent, whose surface tension tends to bend the devices while drying. These supporting bars remained connected to the device during the thermal conductance measurements of S1, S7 and S8. A summary of the polymerization technique, dimensions, device type, polymer carrier layer and the number of supporting bars is shown in Table 3.1.

3.3 Thermoelectric Properties of PEDOT Thin Films

All three thermoelectric properties, S, σ, and κ, were measured along the same in-plane transport direction using the steady state thermoelectric property measurement technique discussed in Chapter 2. The thermal contact resistance was calculated from the thermoelectric voltages measured between the two inner and the two outer
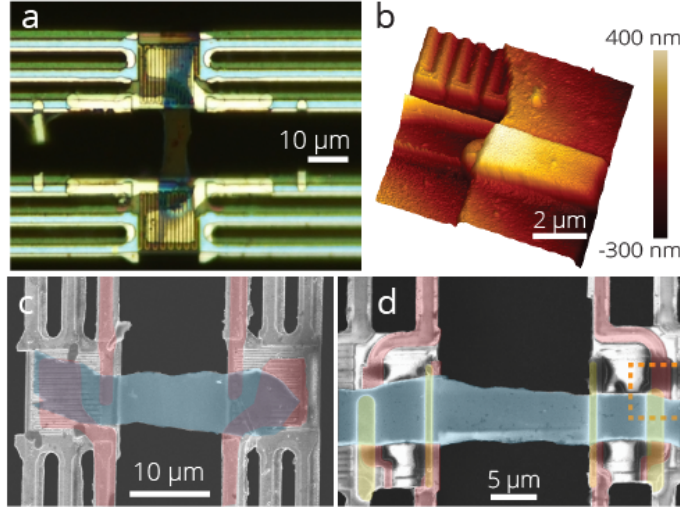
Figure 3.1: (a) Optical microscope image of S9. (b) Three-dimensional (3D) AFM map of an area of S1. (c,d) SEM images of S4 and S1 on the measurement device with false coloring of the electrodes (red), sample (blue), and Au shadowmask deposition (yellow). Partially reproduced from Weathers et al.[76]

electrodes, as discussed in Chapter 2. The thermal contact resistance for the samples assembled on the new device design was found to be negligible, while the thermal contact resistance for the samples prepared on the older device designs was found to be between 5 - 15% of the measured thermal resistance. This thermal contact resistance was eliminated from the measured thermal resistance to yield the intrinsic thermal conductivity of the sample. To remove the contribution to the thermal conductance from the supporting bars in S1, S7 and S8, the PEDOT film in S7 was removed from the device with oxygen plasma reactive ion etching (RIE), and the thermal conductance of just the supporting bars was measured and subtracted from the total measured thermal conductance. The thermal conductance of the supporting bars for S1 and S8 were calculated by assuming the same thermal conductance of the supporting bars as S7, scaled by the length of the bar.

The thermoelectric properties of the seven PEDOT:Tos (S1-S7) and one PE-DOT:PSS (S8) samples are shown in Figures 3.2-3.4. The Seebeck coefficient, shown
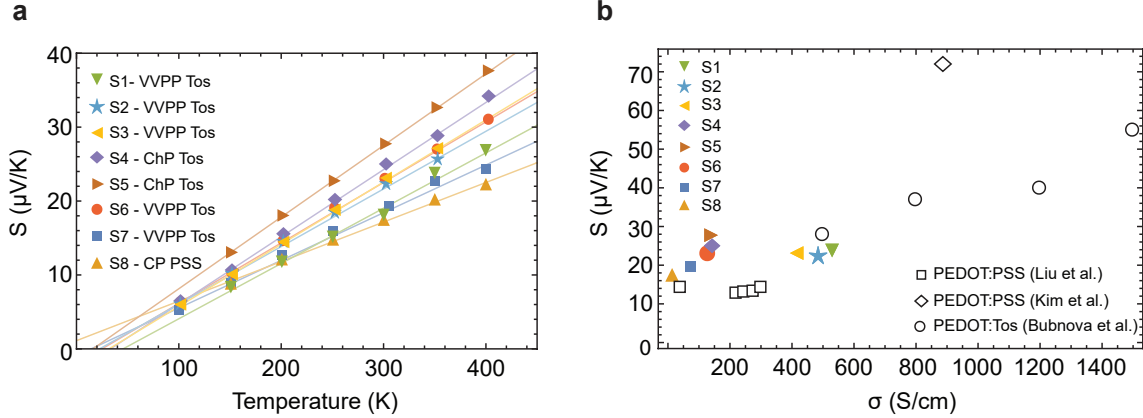
Figure 3.2: (a) Seebeck coefficient as a function of temperature for S1-S8 with linear trend lines. The counterion and polymerization technique are labeled for clarity. (b) Seebeck coefficient as a function of electrical conductivity. Previous results from Bubnova et al.,[120] Kim et al.,[122] and Liu et al.[144] as shown as open symbols. Reproduced from Weathers et al.[76]

in Figure 3.2a, is found to be positive, indicating conduction by positive charge carriers as reported for other PEDOT systems.[120–122] The Seebeck coefficient is linear with temperature in the temperature range studied, consistent with other reports of PEDOT:PSS,[144] but extrapolates to a non-zero value at $T = 0$. The $S \sim T$ behavior is typical of the diffusion thermopower of a metal or semi-metal, for which the Seebeck coefficient is described well by the first order expansion of the Mott formula, Eq. (3.26), in the limit that conduction occurs close to the Fermi level.

On the other hand, the electrical conductivity, shown in Figure 3.3a, of most samples shows non-metallic behavior of increasing σ with temperature as a result of thermal activation of hopping conduction. The Arrhenius plot of $\log \sigma$ versus $1/T$, shown in Figure 3.3b, can be used to estimate the activation energy (in dimensions of temperature) associated with this hopping transport, which ranges from approximately 30 K for the highest conductivity sample S1, to approximately 150 K for the lowest conductivity sample S8. The one exception to this hopping conduction behavior is S1, which shows the highest conductivity as well as a decrease in σ with
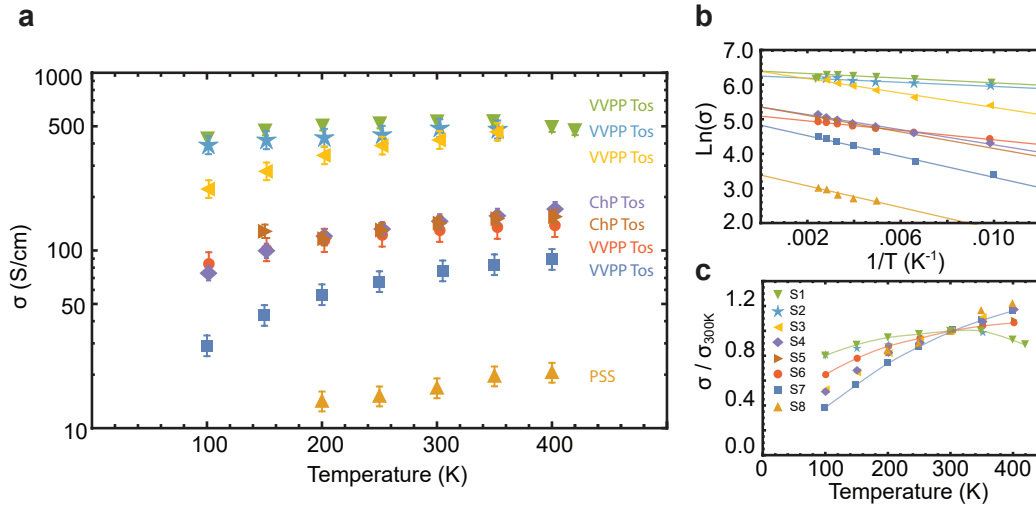
Figure 3.3: (a) In-plane electrical conductivity versus temperature. The counterion and polymerization technique are labeled for clarity. (b) Arrhenius plot of the electrical conductivity in (a). The slope is the activation energy for hopping conduction. (c) Normalized electrical conductivity versus temperature indicating the variation in temperature dependence between samples. Reproduced from Weathers et al.[76]

temperature above 300 K. This behavior is more pronounced in the linear plot of normalized σ versus T in Figure 3.3c. Highly doped PANI and PA have shown a similar maximum in σ at a temperature of approximately 200 K.[145] Furthermore, a previous report on PEDOT:Tos and PEDOT:PSS films has demonstrated that the doping and processing conditions can be used to tune the temperature dependence and magnitude of σ by adjusting the weight given to the hopping and metallic conduction mechanisms.[120] In addition, the σ versus T data for S1 and S2 extrapolates to a non-zero conductivity at zero temperature, indicating delocalized metallic conduction. The Seebeck coefficient is found to be fairly insensitive to the electrical conductivity, as shown in Figure 3.2b. This is in contrast to more highly conducting PEDOT:PSS and VVPP PEDOT:Tos samples studied in previous work,[120,122] which showed increasing S with increasing σ.

The in-plane thermal conductivity is shown in Figure 3.4, and increases ap-
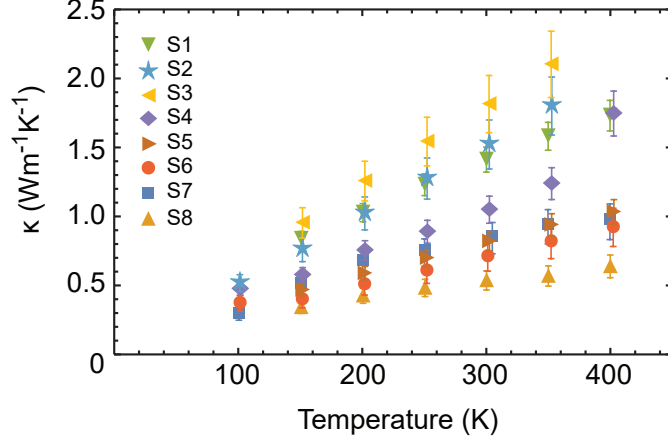
Figure 3.4: In-plane thermal conductivity of S1-S8 as a function of temperature with thermal contact resistance eliminated. Reproduced from Weathers et al.[76]

proximately linearly with T in the temperature range studied. The measured thermal conductivity is higher than previously reported for PEDOT:PSS and PEDOT:Tos samples of comparable σ values.[121,122] While these differences could be due to different processing conditions, variations in the strain, or because of different measurement methods, the measurements here have obtained all three transport properties of the same sample along the same transport direction, allowing for a consistent investigation of the Wiedemann-Franz law. Figures 3.5a-b show the thermal conductivity as a function of electrical conductivity at 300 K and 200 K. The lowest electrical conductivity sample, S8 (PEDOT:PSS), has a thermal conductivity of approximately $0.5 \, \mathrm{W \, m^{-1} \, K^{-1}}$ at room temperature, which is expected to be mainly from the lattice thermal conductivity. This value is consistent with the in-plane thermal conductivity measured by the 3ω method in previous reports, which are shown as open symbols in Figure 3.5a.[121,122] However, contrary to those reports, the thermal conductivity of the samples studied here show a clear increase with increasing electrical conductivity.

Deviations in this trend of increasing κ with σ are observed in S3, which shows slightly higher κ than S1 and S2, the latter of which is from the same growth substrate
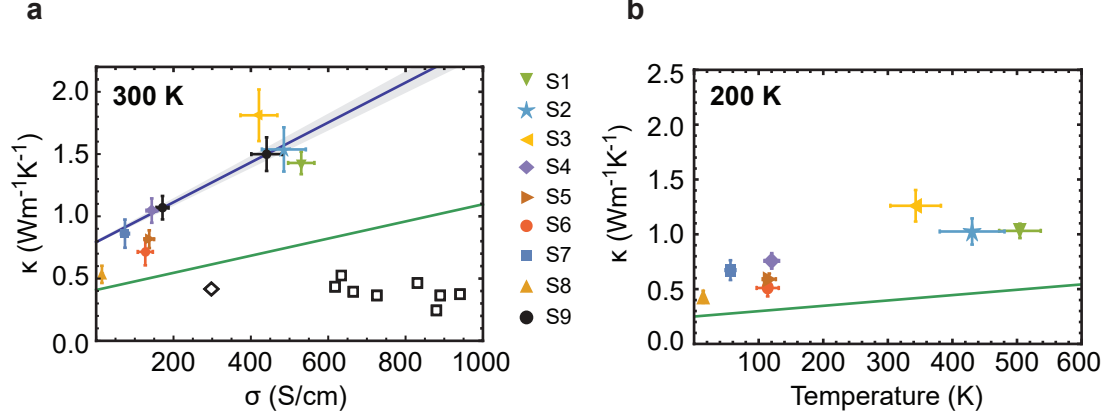
Figure 3.5: In-plane thermal conductivity versus in-plane electrical conductivity for S1-S9 at (a) 300 K and (b) 200 K. The top blue line in (a) is a linear fit to S9 before and after doping with HCl vapor. The bottom green line indicates the predicted slope based on a metallic Lorenz number of $L_0 = \pi^2/3$. The in-plane thermal conductivity measured by Bubnova et al.[121] for PEDOT:Tos films and by Kim et al.[122] for PEDOT:PSS films are shown as open diamond and square symbols, respectively. Reproduced from Weathers et al.[76]

as S1. This variation could be attributed to either differences in the Lorenz number between these samples or differences in the lattice thermal conductivity due to strain or morphology variations. Therefore, the variation in the lattice thermal conductivity was investigated by measuring another sample, S9, before and after doping the sample. The electrical properties of PEDOT:Tos films have been demonstrated to be sensitive to exposure to acidic and basic solutions of HCl and NaOH as a result of a change in the oxidation level of the polymer.[146] Therefore, the thermal and electrical conductivities of S9 were measured before and after placing the sample over a beaker of HCl for 2 minutes.

The results from doping S9 show a 50% increase in κ with the factor of two increase in σ, with a slope comparable to a linear fitting of the κ versus T data for all PEDOT:Tos samples (S1-S9). It is unlikely that the lattice thermal conductivity would increase by 50% as a result of brief exposure to HCl vapor. While high values of

thermal conductivity have been reported for stretched polyethylene nanofibers[47] and other high modulus polymer nanofibers,[147] the Young's modulus of those systems is two order of magnitude greater than that of spin coated PEDOT,[83,148] which is shown to have a nearly amorphous uniaxial alignment from X-ray data.[76] However, there are no known mechanisms by which a factor of two improvement in the crystalline texture or Young's modulus of PEDOT:Tos can be achieved with brief exposure to acidic vapor.

The slope of κ versus σ predicted by the metallic limit of the Wiedemann-Franz law is shown as a green line in Figure 3.5. The results from S1-S9 suggest a slope of κ versus σ that exceeds the Wiedemann-Franz law based on this Sommerfeld value for the Lorenz number. Two previous reports on the thermal and electrical conductivity of suspended bulk PANI and PA films have found a similar increase in κ with σ, with a slope that exceeds the metallic limit.[124,125] A recent report on the thermoelectric properties of PEDOT:PSS, which was published at the same time as this work, has measured both the in-plane and out-of-plane κ and σ in PEDOT:PSS films.[148] The out-of-plane thermal conductivity was found to be insensitive to σ, consistent with previous measurements using the 3ω method, while the in-plane κ was found to have a slope consistent with the metallic limit of the Lorenz number.

3.4   Heterogeneous Model of Charge and Heat Transport

The mixed metallic and non-metallic behavior of the Seebeck and electrical conductivity of the PEDOT:Tos films studied here is known to be characteristic of many conducting polymer systems. While the electrical conductivity of PA and PANI systems show a clear crossover from non-metallic ($d\sigma/dT > 0$) to metallic ($d\sigma/dT < 0$) conduction at approximately 200 K, the Seebeck coefficient remains linear from low temperature to room temperature, without a non-linear contribution from electron-phonon effects like phonon drag.[145] This contradictory behavior has been explained by a heterogeneous model of tunneling conduction between metallic

crystalline domains with a high degree of chain alignment separated by non-metallic disordered barrier regions.[145,149–151] Indeed, grazing incidence wide angle x-ray scattering (GIWAXS) data on VVPP PEDOT:Tos films studied by Bubnova et al. has suggested the presence of crystalline domains dispersed uniformly throughout the PEDOT film.[120] GIWAXS data on the VVPP PEDOT:Tos, ChP PEDOT:Tos, and PEDOT:PSS samples studied here have shown similar morphology.[76] Besides the segregation of PEDOT films into crystalline domains and disordered barriers, PEDOT:PSS and PEDOT:Tos are also known to segregate into counterion (PSS or Tos) rich regions with low electrical conductivity, and PEDOT rich regions with higher electrical conductivity.[120,152]

In heterogeneous structures of this kind, in which electrical transport occurs by tunneling conducting between metallic domains, the measured electrical voltage in the electrical conductivity measurement is dominated by the non-metallic, high-resistivity barrier regions. On the other hand, the difference in the thermal resistance between the metallic and non-metallic regions is expected to be less pronounced because the lattice thermal conductivity makes a significant contribution to the over thermal transport. Therefore, the temperature drop and the resulting thermoelectric voltage is not expected to vary as significantly between metallic and non-metallic domains, resulting in a relatively large contribution to the thermoelectric voltage from the metallic domains. More specifically, both metallic and non-metallic components to the transport are present simultaneously, but their weighting is different for thermoelectric voltage and electrical voltage measurements.

Similarly, the measured thermal conductivity should not be limited by the barrier regions because of the presence of parallel lattice thermal transport in these regions facilitates heat conduction in separated metallic domains. However, these barrier regions are expected to be important for the electronic thermal transport in PEDOT systems. There are two possible mechanisms by which a heterogeneous structure could produce a Lorenz number larger than the metallic value of L_0. First, a bipolar contribution to the thermal conductivity could be important in the non-

metallic barrier regions with low electrical conductivity characteristic of an intrinsic semiconductor. This bipolar contribution could result in an increase in L compared to L_0. Furthermore, the expression for the Lorenz number in the non-degenerate limit, $L = r + 5/2$, (Eq. 3.19), suggests that L can be larger than the metallic limit ($L = \pi^2/3$) as long as $r > 0.79$. A value of r greater than zero suggests that the scattering of electrons happens more easily with decreasing energy, such as for impurity scattering ($r = +3/2$). The tunneling conduction of charge carriers in the heterogenous PEDOT films, would also be expected to be limited by a scattering process that decrease in intensity with decreasing energy. Simply put, lower energy carriers are less likely to overcome the tunneling barrier. Therefore, r is expected to take a positive value, which can result in L being greater than L_0. Both mechanism could exist simultaneously, resulting in the relatively large L observed in the data in Figure 3.5. Because the thermoelectric efficiency scales as σ/κ, the electronic thermal conductivity and the Lorenz number is a crucial parameter in designing the best thermoelectric materials. In designing a PEDOT system with lower Lorenz number, it is still necessary to maintain a large Seebeck coefficient. This could perhaps be achieved by not only tuning the electronic band structure of PEDOT through variations in the doping, but also by tuning the morphology of the heterogeneous polymer system.

3.5   Summary

The thermoelectric properties of suspended PEDOT:Tos and PEDOT:PSS thin films were measured along the same in-plane transport direction simultaneously on the same sample. The thermal conductivity is found to increase with electrical conductivity with a slope exceeding that predicted by the Wiedemann-Franz law in the metallic limit. While variations in the strain and lattice thermal conductivity could explain some variation in the thermal conductivity of the PEDOT samples, the large increase in κ with σ is also explained by significant electronic thermal transport in this system. Both phonon assisted hopping conduction and a bipolar contribution to the

thermal conductivity are possible mechanisms by which the apparent Lorenz number of these samples exceeds that predicted by the metallic limit of the Wiedemann-Franz law.

The samples in this work have not been optimized for thermoelectric efficiency, and therefore the highest zT is only 0.005 at room temperature for S3. This low zT is primarily caused by a low power factor, as well as the higher thermal conductivity compared to previously reported work. While the power factor can be improved by engineering of the band structure through doping,[120,122] a significant electronic contribution to the thermal conductivity would still exist unless κ_e could be reduced in optimally doped samples. This work highlights the fact that the transport properties of PEDOT thin films are highly sensitive to the processing conditions, so that an accurate measurement of zT requires measuring all three properties along the same transport direction and under the same sample conditions. The advancement of polymer thermoelectrics is a nascent field with vast potential for producing low-cost and flexible thermoelectrics. The results from this work are expected to further motivate fundamental studies of the coupling of heat and charge transport in these complex materials, and to further advance the development of high efficiency polymer thermoelectrics and electronic devices.

Chapter 4

Heat and Charge Transport in Higher Manganese Silicide Nanostructures[1]

Among the candidates for non-toxic, low-cost silicon based thermoelectric materials for high temperature applications is the Nowotny chimney ladder phased higher manganese silicide (HMS) with the general chemical composition of $MnSi_{2-x}$. The thermoelectric properties of pure crystalline HMS are moderate, with a maximum zT of approximately 0.5 at 800 K.[17] While this material received little attention following extensive bulk crystal characterization in 1970s,[17,153] it has received a renewed interest in the past ten years, with the synthesis of HMS nanowires, nanocrystals and doped bulk composites,[154–161] and very recently a reported zT of approximately 1.0 with bulk-nanostructured rhenium doped HMS.[162,163] In fact, based on the results reported in those recent works, HMS has very recently begun to be used as the p-type leg in prototype commercial thermoelectric modules.[164]

While the bulk thermoelectric properties of crystalline HMS have been relatively well-known for years, a general understanding of the structure-property relationships in bulk and nanostructured HMS has been limited. In particular, the

nature of the low and anisotropic thermal conductivity in this complex crystal has remained elusive. The work in this chapter will address some of the open questions about the low and anisotropic thermal conductivity of HMS and the effects of size confinement on the thermoelectric properties of HMS nanoribbons. Clarifying these questions can help to further advance the understanding and engineering of HMS as a viable, low-cost, abundant thermoelectric material for widespread applications.

4.1 Structure and Properties of Bulk Higher Manganese Silicide

Within the general class of complex crystals with quasi-one dimensional substructures is the semimetallic, Nowotny chimney ladder HMS phase, which consist of a β-Sn tetragonal sublattice of Mn atoms surrounding coupled helices of Si aligned along the c-axis, as shown in Figure 4.1a. The term "chimney ladder phase" refers to the positioning of Si helical "ladders" inside a rigid Mn "chimney." The hard Mn sublattice maintains a nearly constant c-axis unit cell length of $c_{\mathrm{Mn}} = 4.3\,\text{Å}$ across all phases, while the softer Si sublattice length, c_{Si}, varies slightly depending on the stoichiometric composition. A commensurate HMS crystal follows the empirical formula $nc_{\mathrm{Mn}} = mc_{\mathrm{Si}}$, where n and m are integers, which requires that a single unit cell consist of an integer number of Mn and Si sublattice units. A number of crystal phases have been identified by x-ray diffraction (XRD) and transmission electron microscopy (TEM),[154,165,166] including the $\mathrm{Mn_4Si_7}$, $\mathrm{Mn_{15}Si_{26}}$, $\mathrm{Mn_{11}Si_{19}}$ and $\mathrm{Mn_{27}Si_{47}}$ phases. While XRD data has suggested that bulk crystals can be composed of commensurate phases, electron microscopy studies have suggested that these commensurate phases are a result of averaging over a large sampling area, and that only incommensurate structures exist in real crystals.[167] Figure 4.1a shows the sublattice and crystal structures of the simplest HMS phase, $\mathrm{Mn_4Si_7}$, which contains 44 atoms and is sometimes denoted by its stoichiometric ratio, $\mathrm{MnSi_{1.75}}$. While each HMS phase contains nearly identical a lattice parameter, the c lattice parameter varies widely depending on the composition, ranging from $17\,\text{Å}$ for the simplest phase to

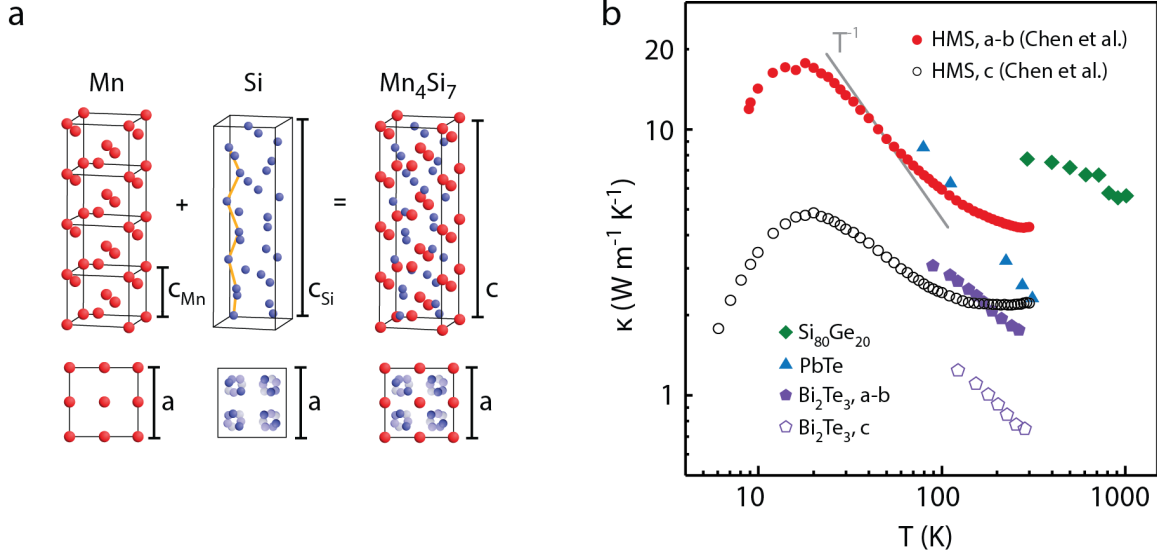approximately 118 Å for the $Mn_{27}Si_{47}$ phase, which also contains 296 atoms in a unit cell.

Figure 4.1: (a) Crystal structure of higher manganese silicide (HMS) showing the tetragonal Mn and helical Si sublattice which combine to form the commensurate Mn_4Si_7 structure. The yellow line guides the winding of one Si helix, and the top down view shows the four coupled helices contained within one unit cell. (b) Thermal conductivity of bulk HMS from Chen and Weathers et al.[168] The thermal conductivity of $Si_{80}Ge_{20}$, PbTe, and Bi_2Te_3 are shown for comparison. Reproduced from Chen and Weathers et al.[168]

Bulk HMS crystals are often grown with unintentional layers of metallic, manganese rich MnSi (monosilicide) phase precipitating perpendicular to the c-axis as a result of the peritectic reaction of HMS. Virtually all bulk single crystals of HMS have been reported to contain such striations of MnSi phase, which are a few hundred nanometers in thickness and spaced tens of microns apart. However, a recent report has shown that through melt-quenching, the size of these MnSi layers can be reduced to create MnSi islands, resulting in a zT of 0.64 at 823 K.[162] Furthermore, small HMS crystals without MnSi inclusions have been synthesized by chemical vapor transport.[155] These high purity HMS crystals exhibited slightly higher hole mobility

that HMS with MnSi as a result of their higher purity, but maintained nearly identical carrier concentration and lattice thermal conductivity as bulk HMS with MnSi.

The thermal conductivity of HMS is phenomenally low for a crystal made of relatively light elements, and is even comparable to the heavy element crystals commonly used for thermoelectric devices, including Bi_2Te_3 and PbTe, and is even lower than mass disordered, alloyed SiGe, as shown in Figure 4.1b. Indeed, HMS can be described within the context of quasiperiodic crystals with both long range order and short range disorder. Furthermore, the thermal conductivity of HMS is highly anisotropic, with a factor of two difference at room temperature between the poorly conducting ladder direction (c-axis) and the cross ladder direction (a-axis). In fact, the anisotropy is similar in magnitude to that of Bi_2Te_3, for which large bonding anisotropy exists between the covalently bonded in-plane direction, and the van der Waals bonded out-of-plane direction. However, the degree of anisotropy in the thermal conductivity of HMS is puzzling because the bonding anisotropy is not expected to be as dramatic as a two-dimensional (2D) layered material, as an HMS crystal is entirely covalently bonded.

The electrical conductivity of bulk HMS is also anisotropic, and is on the order of $500\,\mathrm{S\,cm^{-1}}$ and $200\,\mathrm{S\,cm^{-1}}$ along the a-axis and c-axis,[168] respectively, which is two orders of magnitude lower than poorly conducting metals like stainless steel. The band structure of HMS[169] calculated by DFT places the Fermi level inside the gap for the Mn_4Si_7 phase, and just inside the valence band at the Γ point for the $Mn_{11}Si_{19}$, $Mn_{15}Si_{26}$, and $Mn_{27}Si_{47}$ phases, making HMS a degenerate p-type semiconductor consistent with the decrease in electrical conductivity with temperature for bulk HMS.[168]

The Seebeck coefficient of bulk HMS is positive and highly anisotropic, with the poorly conducting c-axis direction displaying 50% higher Seebeck coefficient than the highly conducting a-axis.[168] An anisotropy in the Seebeck coefficient to this degree is unusual. Even for highly anisotropic materials like Bi_2Te_3, the Seebeck coefficient

is almost isotropic.[17] For a bulk degenerately doped crystal, the anisotropy in the Seebeck coefficient can be explained qualitatively as a directional variation in the energy dependence of the scattering rates for holes along different transport directions, as discussed in Section 3.2. For a non-degenerate semiconductor, the Seebeck coefficient for holes is often expressed as a function of the scattering parameter r, where the energy dependent charge carrier relaxation time is given by $\tau = \tau_0(E/k_bT)^r$,

$$S = \frac{k_b}{q}\left[\frac{(r+5/2)F_{r+5/2}(\zeta_h)}{(r+3/2)F_{r+1/2}(\zeta_h)} - \zeta_h\right] \tag{4.1}$$

where ζ_h is the dimensionless reduced Fermi level for holes, $E_{F,h}/k_bT$, and $F_j(\zeta)$ is the Fermi Dirac integral,

$$F_j(\zeta) = \int\limits_0^\infty \frac{\eta^j}{e^{\eta-\zeta}+1}\mathrm{d}\eta \tag{4.2}$$

In principle, r could be different between the two transport directions, depending on the nature of the scattering. For example, the semiconductor/metal interface at the HMS/MnSi boundaries could have an electron filtering effect that could increase the Seebeck coefficient along the c-axis, as demonstrated for other superlattice structures.[170] However, the relatively large spacing of ~ 50 μm between MnSi stripes suggests this effect could be small. Furthermore, in addition to boundaries between the MnSi and HMS phases, there can also be boundaries between different phases of HMS, which contain slightly different Si ladder arrangements. If the interaction strength between the Si and Mn sublattices is strong enough, it is possible that the Si ladder would not be able to relax enough to smooth out these phase boundaries. While crystal defects of this type would certainly affect the propagation of a phonon, it is unclear whether the hole scattering would be greatly affected. Experimentally, it has not been possible to control the HMS phase composition in the crystal growth or to resolve a substantial difference in phase between different areas of the sample. Therefore, determining the impact of phase boundaries on the Seebeck coefficient has remained elusive. The anisotropy in the Seebeck coefficient of bulk HMS could also be partly explained by the metallic MnSi stripes, with low Seebeck coefficient,

that precipitate perpendicular to the c-axis and can electrically short the measured thermoelectric voltage along the a-axis.[17]

4.2 Phonon Dispersion and Diffuson Model of Thermal Conductivity

In order to understand the anisotropic and low thermal conductivity of HMS, the phonon dispersion of HMS has recently been measured by Chen and Weathers, et al.[168] with inelastic neutron scattering (INS) on the wide angular range chopper spectrometer (ARCS) and triple-axis spectrometer at Oakridge National Lab (ORNL). In addition, density function theory (DFT)/lattice dynamics simulations were simultaneously performed by researchers in Natalio Mingo's group (CEA Grenoble) and Derek Stewart's group (Cornell) to provide further insights into the measured phonon dispersion. The DFT/lattice dynamics simulations were performed on the Mn_4Si_7 phase, which possesses nearly seven times fewer atoms per unit cell compared to the $Mn_{27}Si_{47}$ phase, the majority phase of the synthesized bulk crystal. Despite the much smaller unit cell, the general structure of these phases is nearly identical, aside from minor variations in the silicon helical arrangement.

Figure 4.2 shows the phonon dispersion measured with ARCS along the $\mathbf{q} = $ [H00], [0K0], and [00L] phonon wave vector direction from various Brillouin zones indexed by the reciprocal lattice vectors $\mathbf{G_{HKL}} = (400),(420),(427)$, and (4120) with respect to the Mn sublattice of the $Mn_{27}Si_{47}$ phase. The incident neutron energy is 40 meV. The scattering intensity scales with the neutron scattering length of the constituent elements, which is -3.73 and 4.15 fm for Mn and Si, respectively, which is relatively low compared to, for example, Pb with a scattering length of 9.40 fm. In addition to the relatively low scattering cross section for this material, it was not possible to synthesize HMS crystals in excess of 2 g, which further limits the resolution. Moreover, the scattering probability also drops off dramatically with increasing energy, so that only the modes with energies less than ~ 30 meV were detectable after four days of acquisition. These inherent limitations in the signal quality limit

the energy resolution to approximately 1 meV, which is much greater than the intrinsic linewidth of the branches determined from the phonon scattering time. To improve the appearance of the intensity maps in Figure 4.2, a rotationally symmetric Gaussian filter was applied to the experimental data with a standard deviation of 2 pixels and a filter size of 2×2 pixels.

As discussed in Section 2.3, because S scales as $|\mathbf{Q} \cdot \mathbf{e}_i^\alpha|^2$, the strength of the longitudinal and transverse phonon modes in the ARCS data depends on the Brillouin zone, $\mathbf{G}_{HKL}$, and the momentum transfer direction, $\mathbf{q}$. For example, the data for $\mathbf{G}_{\mathbf{HKL}} = (400)$ along [H00] (Figure 4.2a) is dominated by the longitudinal phonon modes, while the data from $\mathbf{G}_{HKL} = (400)$ along [00L] and [0K0] (Figures 4.2b and 4.2c) is dominated by the transverse phonon modes. Likewise, Figures 4.2d, 4.2e, and 4.2f display the TA polarized modes along the [0K0] direction from different Brillouin zones.

To the right of each ARCS data plot is the simulated dynamical structure factor according to Eqs. (2.22 - 2.23) for the Mn_4Si_7 structure analyzed by DFT, at a temperature of 300 K. The simulated structure factors show a mirror reflection across the [0K0] axis with respect to the experimental results, which could possibly be due to a difference in the chirality of the Si helices between the computational and experimental crystals. Therefore, in Figures 4.2d, 4.2e, and 4.2f, the simulated structure factors are plotted along the $\mathbf{G}_{\mathbf{H-KL}} + \mathbf{q}$ direction. The simulated structure factors are in general agreement with the experimental results, and confirm the polarizations of the modes observed in the ARCS data.

The ARCS data reveals the presence of very low energy, flat optical modes that cross the acoustic branches at energies in the range of $10 - 25$ meV, as seen in Figures 4.2a, 4.2b, and 4.2c, compared to the ~ 40 meV optical branches in a material like silicon. Along the [00L] direction, parallel to the c-axis, a broad linear band extends from the Γ point to approximately π/c_{Mn}, i.e., the zone boundary of the Mn sublattice. This suggests that along this direction, the neutron scattering
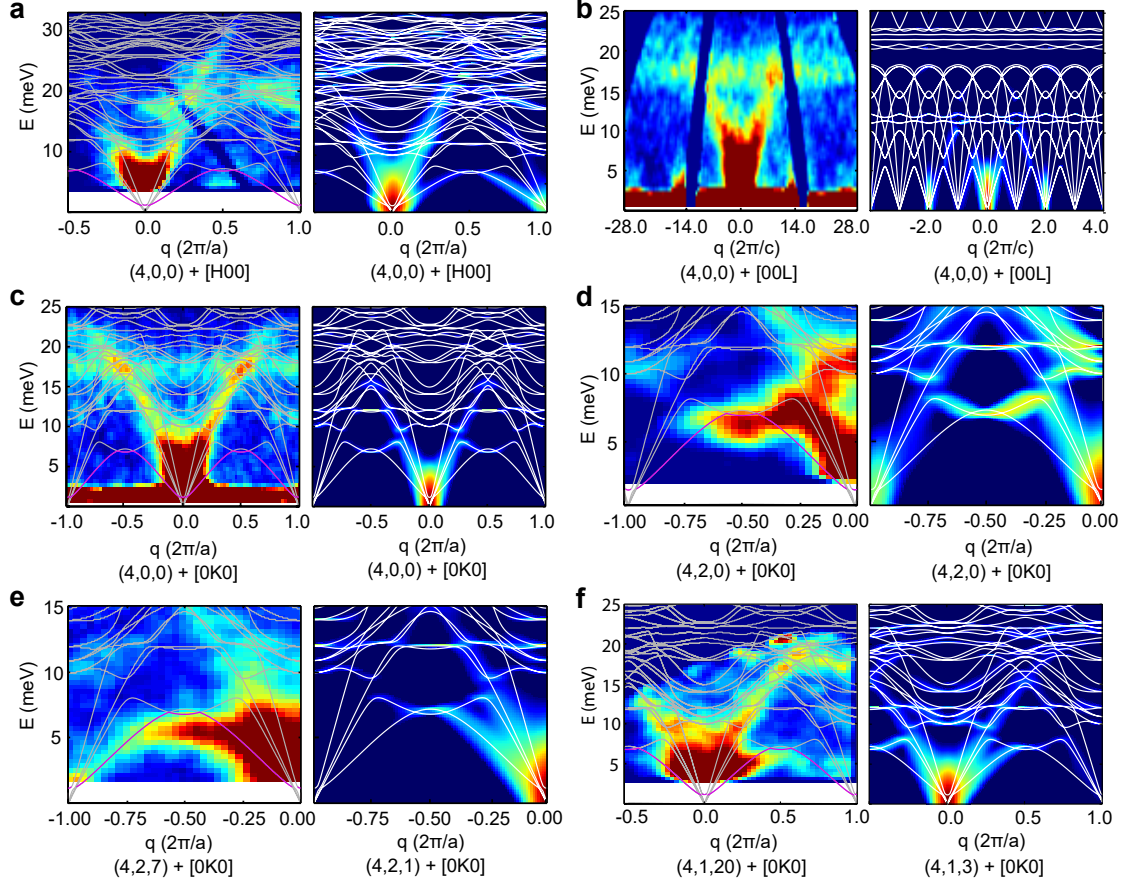
Figure 4.2: The neutron scattering intensity, $S(\mathbf{Q}, E)$, measured with ARCS (left figures), and the simulated dynamical structure factor for Mn_4Si_7 calculated from Eqs. (2.22 - 2.23) (right figures). The harmonic phonon dispersion determined from lattice dynamics simulations is overlaid for comparison, with the twisting polarization shown in (d,e,f) in purple. The dominant phonon modes observed are (a) the LA and LO modes along [H00], (b) the TA and TO modes along [00L], (c) the a-b polarized TA and TO modes along [0K0], (d) the a-b polarized TA and low lying optical modes along [0K0], and (e,f) the TA and twisting modes along [0K0]. Reproduced from Chen and Weathers et al.[168]

70

intensity is more sensitive to the periodicity of Mn sublattice, which is apparently partly decoupled from the Si sublattice.

The phonon dispersion calculated from DFT is overlaid on the experimental data in Figure 4.2, and is also plotted in Figure 4.3 along the principle axes. The DFT results show a very low lying optical mode that crossed the Γ point at approximately 1 meV and makes an avoided crossing with the LA and c-polarized TA modes along [H00]. Interestingly, this mode is associated with the twisting motion of the silicon helices and minor translations of the Mn atoms. Such twisting motion is reminiscent of the torsional mode in single walled carbon nanotubes, in which the mode is a purely acoustic mode in the absence of interactions with adjacent carbon nanotubes. The twisting polarization is observable in the ARCS data in Figures 4.2e and 4.2f, in which the energy is slightly lower than predicted by DFT. The discrepancy could be due to the difference in structure between the Mn_4Si_7 phase used in the simulations, and the $Mn_{27}Si_{47}$ phase determined for the bulk crystal. In particular, the total mass of the Si helix could increase with increasing c lattice parameter, which could have a measurable effect on the twisting mode frequency. The group velocity of the twisting polarization along the c- and a-axes is 20.8 and 1.59 $km\,s^{-1}$, respectively, which indicates a large anisotropy because of the strong interaction between adjacent Si atoms within each helix, compared to that between adjacent helices.

The twisting mode can also be understood within the context of phasons in incommensurate aperiodic crystals. The HMS structure has three conventional translational degrees of freedom, resulting in three conventional acoustic modes, as well as the relative translation of one sublattice relative to the other, which can give rise to a phason mode.[171] In the limit of zero interaction strength between the sublattices, this phason mode is a purely acoustic mode with zero energy associated with a $\mathbf{q} = 0$ translation. The small band gap of 1 meV at $\mathbf{q} = 0$ for the twisting mode suggested that the interaction strength is indeed finite, but apparently not very strong. However, while two independent acoustic-like phasons associated with the independent propagation of energy on each sublattice have been reported for some aperiodic in-
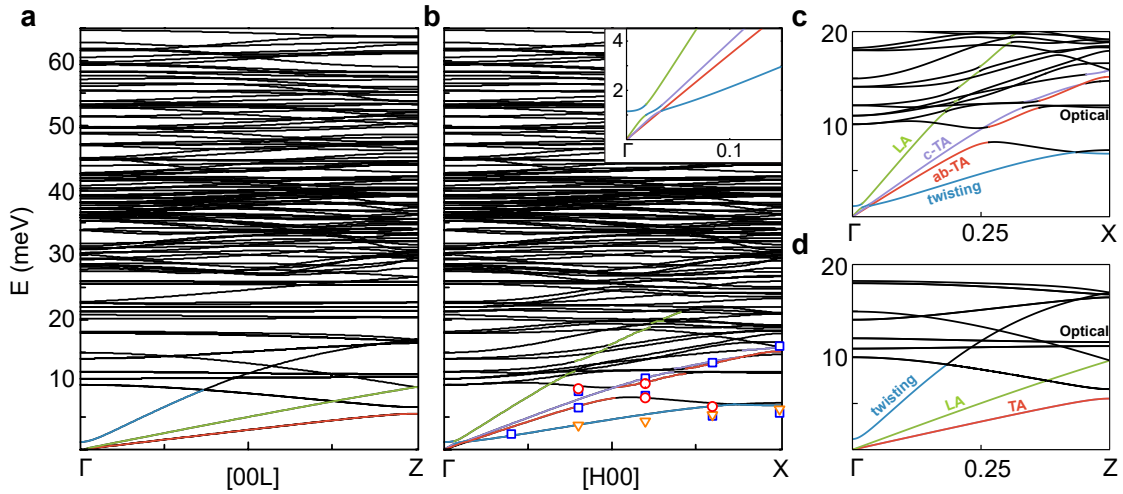
Figure 4.3: (a) Phonon dispersion calculated from DFT along the (a) $\mathbf{q} = [00L]$ and (b) $\mathbf{q} = [H00]$ principle directions. Open symbols are additional inelastic neutron scattering results from the triple axis spectrometer measured in the (200) zone (blue squares), (220) zone (red circles) and (227) zone (orange triangles). (c,d) Low energy phonon dispersion from (a) and (b) with labels and coloring of the polarizations. Reproduced from Chen and Weathers et al.[168]

commensurate systems,[172–174] this is not necessarily the case for HMS. The neutron scattering data suggests that both the LA mode and the twisting mode are found on the same reflection, suggesting that the sublattices remain coupled even in the high-q regime. A similar conclusion has been suggested by de Boissieu, Currat and Francoual[175] based on neutron scattering data from HMS. Further investigation of the low energy vibrational modes with ultrasonic or Brillouin light scattering measurements could provide some additional insights.

The calculated phonon dispersion in Figure 4.3 is overlaid with additional experimental results from the triple axis spectrometer, which agree well with the DFT results. Figure 4.3 also shows the vast number of optical modes found in this system, with particularly low group velocities along [00L]. While the low group velocity of most optical modes could result in each mode making a small contribution to the overall thermal conductivity, these modes play an important role in the scattering of low and intermediate energy phonons, because of the increased phonon scattering phase

space. As a result, the large number of optical modes are expected to contribute to the overall low thermal conductivity of HMS. On the other hand, the thermal conductivity displays a very weak temperature dependence in the range of $200 - 700$ K, with a slope much less than the expected T^{-1} dependence. In this case, optical phonons could make a substantial contribution to the heat transport at intermediate temperatures, which can result in the plateau in the thermal conductivity seen in Figure 4.1b.[17]

Because the thermal conductivity scales as $\kappa \sim v_\alpha^2 \tau_\alpha$, where v_α is the group velocity and τ_α is the scattering relaxation time of phonon mode α, the anisotropy in the thermal conductivity could be due to an anisotropy in the group velocity or due to an anisotropy in the scattering rate for phonons along the a- and c-axes. To investigate the former case, the group velocities for all modes along the two directions were calculated from the DFT results, and are plotted in Figure 4.4a as a function of energy. The c-axis has higher group velocity at energies below ~ 7 meV primarily as a result of the stronger bonding along the helical chains than between chains. However, at energies above ~ 7 meV, the group velocity anisotropy is reversed, and the c-axis displays an average group velocity approaching zero. The long c-axis lattice parameter results in a low group velocity for many optical modes along [00L] because of the greater degree of disorder between the incommensurate Mn and Si sublattices. High energy optical modes along this direction encounter a crystal with a large degree of short range disorder, and behave similarly to optical modes in an amorphous material.

The anisotropy in the scattering rate can also contribute to the anisotropy in the thermal conductivity, and can be considered by introducing a relaxation time approximation model for the thermal conductivity. For a complex crystal like HMS, in which the structure is characterized by short range disorder, the scattering of higher energy optical modes is expected to be very intense because of the local disorder within the unit cell. Modes in this regime are no longer well described by the classic Peierls-Boltzmann theory of weakly interacting phonon transport.[176,177] In a glass or
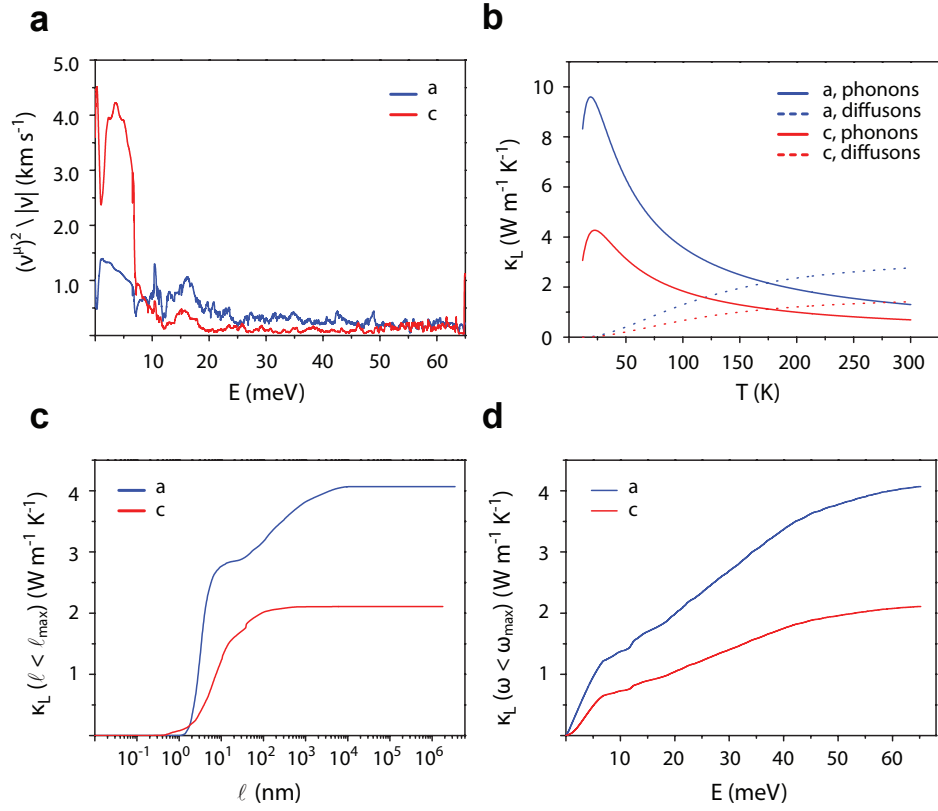
73

Figure 4.4: (a) The group velocity as a function of energy for all modes along the *a*- and *c*-axes. (b) The contribution to the lattice thermal conductivity from phonons and diffusons according to Eqs. (4.5 - 4.6). (c-d) The calculated lattice thermal conductivity accumulation as a function of mean free path and energy. Reproduced from Chen and Weathers et al.[168]

strongly disordered crystalline material, the definition of a phonon can be ambiguous, and instead, the vibrational modes can be better described by the Allen-Feldman theory of ballistic, diffusive and localized modes.[177,178] In this framework, vibrational modes are segregated into extended (E) and localized (L) modes separated in energy by a mobility edge. Very low-energy extended modes are termed propagons (P), which propagate ballistically for several atomic distances with a well-defined wavevector and mean free path, before being scattered. These are what are traditionally thought of as phonons in ordered crystals. Above what is called the Ioffe-Regel crossover,[179] extended modes are characterized by diffusive transport and no longer have a meaningful wavevector or mean free path. These extended modes are termed diffusons (D). Beyond the mobility edge, the modes are no longer extended and locons (L) are found to be localized near a single lattice site.
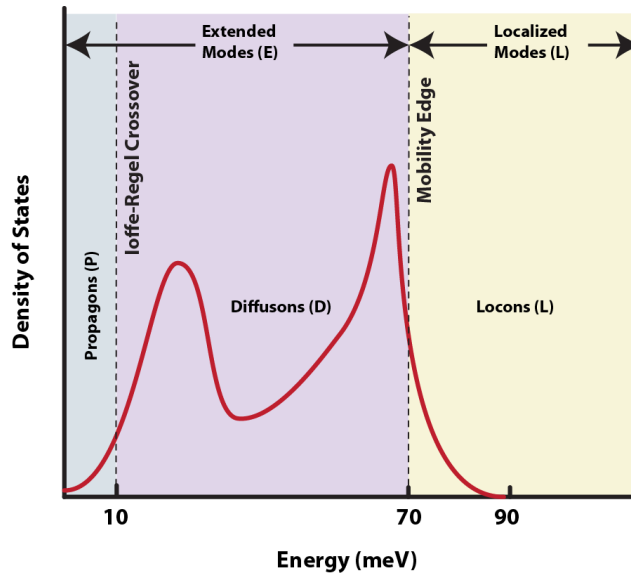

Figure 4.5: Approximate density of states of amorphous silicon with labels for the types of extended and localized vibrational modes. Recreated from Allen, Feldman, Fabian, and Wooten.[178]

Figure 4.5 shows a schematic of the types of vibrational mode with a sketch of the density of states for Stillinger-Weber amorphous silicon.[178] The Ioffe-Regel

75

crossover and the mobility edge are not necessarily close in energy, and their boundaries depend on the material system. The calculated inverse participation ratios of the atoms for a given mode can be used to determine the mobility edge,[180] which is generally near the high-energy region of the spectrum. The inverse participation ratio will typically increase by several orders of magnitude for localized modes above the mobility edge. On the other hand, the Ioffe-Regel crossover is not always as well defined, but should lie near the low-energy regime of vibrational modes in glass or disordered crystals.

While locons are characterized by an exponential decay in the eigenvector with radial distance from a central lattice site and only carry heat through anharmonic hopping interactions, the eigenvectors of diffusons remain non-zero even over several lattice sites. As Allen, Feldman, Fabian and Wooten note, the behavior of the temperature dependent thermal conductivity of glasses in the plateau region (> 20 K) can be described as a specific heat multiplied by a diffusion coefficient, D, which is on the order of $a^2 \omega_c/3$, where ω_c is the Ioffe-Regel crossover frequency.[178,181,182] Therefore, the contribution to the thermal conductivity from the diffuson modes is given by

$$\kappa = \frac{1}{V} \sum_i C_i D_i \tag{4.3}$$

where the diffusivity of the ith mode, D_i, is defined as

$$D_i = \frac{\pi V^2}{3\hbar^2 \omega_i^2} \sum_{i \neq j} |S_{ij}|^2 \delta(\omega_i - \omega_j) \tag{4.4}$$

and $S_{ij}(i \neq j)$ are the off-diagonal elements of the heat current operator for modes i and j, which describes the coupling of the harmonic eigenstates.[177,183]

The thermal conductivity of the HMS crystal along the direction μ, κ^μ, can then be expressed as two separate contributions from propagons (phonons) and diffusons[168]

$$\kappa^\mu \sum_{\alpha, q, \omega < \omega_c} \frac{\partial n}{\partial T} \hbar \omega \left(\frac{\Delta q}{2\pi} \right)^3 (v_\alpha^\mu)^2 \tau_\alpha + \int_{\omega_c}^{\infty} g_d(\omega) \frac{\partial n}{\partial T} D^\mu \hbar \omega \, d\omega \tag{4.5}$$

where n is the Bose-Einstein distribution at temperature T, τ_α is the relaxation time for a vibrational mode α, and v_α^μ is the group velocity projection along μ for mode α. The diffuson density of states, g_d, is determined from the standard density of states expression, $g_d = 1/N_q \sum_q \delta(E - E_q)$, where q sums over all lattice vectors in the Brillouin zone and N_q is the total number of lattice vectors in the Brillouin zone. The Ioffe-Regel crossover separating propagons and diffusons, ω_c, can be empirically determined from the behavior of the dispersion. The INS results suggest that well-defined phonon branches exist up to approximately 20 meV. While at higher energies, only flat, broad bands are observable. Similarly, the DFT results show a high concentration of flat optical modes above 20 meV, which are consistent with the behavior of diffusons. Therefore, ω_c is empirically chosen to be 20 meV. The relaxation time for phonons is composed of a boundary scattering term as well as an anharmonic phonon-phonon scattering term according to

$$\tau^{-1}(\omega) = \frac{v}{L} + \min(Bg_p(\omega)T, \omega/\pi) \tag{4.6}$$

where the phonon density of states, g_p, is calculated in the same way as the diffuson density of states for modes below 20 meV. The boundary scattering length scale, L, and the phonon-phonon scattering intensity B, are left as fitting parameters. The min() function ensures that the relaxation time for phonon-phonon scattering is smaller than π/ω. That is, that the mode has time to exist for at least half of the oscillation period. The diffusivity, D^μ, takes the functional form $D_0\omega_c/\omega$, where D_0 is a third adjustable parameter.

It is worth noting that the relaxation time of a propagon mode is required to be long enough that the propagon exists for a meaningful amount of time, i.e., for longer than at least one-half of an oscillation. Otherwise, an extended plane-wave can no longer be properly defined. However, the diffusons require no such limitation, as the concept of a lifetime, mean free path, or wavevector are no longer meaningful when the scattering is so intense. Nonetheless, a pseudo-mean free path can be defined as $D/|\partial\omega/\partial q|$, which is on the order of $2 - 3$ nm and corresponds to a pseudo-lifetime

on the order of picoseconds. In addition, a thorough justification for the use of the diffuson framework to describe intermediate energy modes in HMS would require a full calculation of the diffusivity from Eq. (4.4) either from first principles with a large disordered supercell or by molecular dynamics with a suitable potential. However, this is computationally unrealistic because of the enormous number of atoms in the HMS unit cell and the lack of an appropriate parameterized potential. Therefore, the diffuson model is employed here as an assumption, in order to investigate its feasibility in recreating the temperature dependence of κ_L for an incommensurate complex crystal like HMS. However, the plateau in the thermal conductivity above 200 K can also be well explained simply by the presence of a large number of localized modes in this temperature range, without the need for defining a "diffuson" state. In this case, at temperatures above the plateau region in the thermal conductivity ($\gtrsim 200$ K), these localized modes would contribute to the thermal conductivity through an anharmonic hopping mechanism.[184]

With the three adjustable parameters, the thermal conductivity according to Eqs. (4.5 - 4.6) was fit to the bulk thermal conductivity determined experimentally. This yielded the following values for the fitting parameters: $B = 0.610$ and 4.85 rad ps^{-2}, $D_0 = 3.50$ and 1.79 nm^2 ps^{-1}, and $L = 18041$ and 923 nm, along the a and c-axes, respectively. The values of the fitting parameters suggest a large degree of anisotropy in the phonon boundary scattering length scales. This anisotropy can be explained by disorder in the silicon helix as a result of stacking of different phases of HMS with slightly different silicon helical arrangements along the ladder direction, which could result in more stacking faults along the c-axis. Likewise, the stronger boundary scattering along the c-axis can also be explained by the MnSi layers that precipitate perpendicular to the c-axis. The anisotropy in the phonon-phonon scattering rates are equally large between the two transport directions, which could be a result of the much larger umklapp scattering rates along the c-axis, which has a very narrow Brillouin zone. The anisotropy in D is smaller, but could be a result of anisotropy in the bonding arrangements of the Mn and Si sublattices along the a-
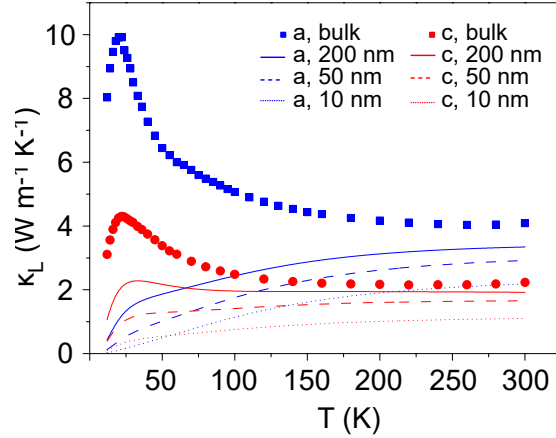
78

Figure 4.6: The calculated lattice thermal conductivity as a function of temperature according to Eqs. (4.5 - 4.6) with various boundary scattering mean free paths, ℓ_b. The bulk data from Chen and Weathers et al. is shown as blue and red symbols. Reproduced from Chen and Weathers et al.[168]

and c- axes. The lattice thermal conductivity contributions from the phonons and diffusons are shown in Figure 4.4b, which indicates that phonons are the primary heat carriers at low temperatures, and diffusions become more dominant at temperatures above 200 K, when the optical modes become more highly populated and the total thermal conductivity plateaus.

The lattice thermal conductivity accumulation as a function of energy and mean free path are shown in Figures 4.4c and 4.4d, respectively. Diffusons with energies as high as 50 meV make considerable contributions to the thermal conductivity in this system, which is consistent with the temperature dependence of the thermal conductivity. However, the majority of the heat is carried by modes with mean free paths between $1 - 20$ nm, with only 32% of the heat current being carried by modes above 10 nm along the a-axis and 40% of the heat current being carried by modes above 10 nm along the c-axis.

The effects of size confinement can also be investigated with the model described in Eqs. (4.5 - 4.6). An additional term, v/ℓ_b can be incorporated into relaxation time given by Eq (4.6) to account for scattering at a nanostructure surface.

Figure 4.6 shows the calculated size confined thermal conductivity using the fitted values of L, B, and D_0, with ℓ_b set as either 200, 50, or 10 nm. When the grain size is as small as 10 nm, the thermal conductivity is reduced by approximately a factor of 2 along both directions at room temperature, which correspond to as much as a factor of 2 improvement in the thermoelectric efficiency as long as the charge carrier transport is less sensitive to size confinement at this length scale. Indeed, a two-band semi-classical model has estimated the hole mean free path be on the order of $1 - 2$ nm,[158] which suggests that nanostructured HMS with grain size on the 10 nm scale could result in significant improvements in the thermoelectric efficiency.

The work discussed in this section (4.2) was a collaboration between researchers at CEA Grenoble, Cornell, and UT Austin. The work in the following section is solely the work of this author.

4.3   Thermoelectric Properties of HMS Nanoribbons

Further understanding of the effects of size confinement on the thermoelectric properties of HMS can be found by investigating the properties of HMS nanostructures with the use of the suspended resistance thermometer devices described in Chapter 2. HMS nanowires (NWs) and nanoribbons (NRs) were grown by chemical vapor deposition (CVD) by Jeremy Higgins and Jack Degrave in Professor Song Jin's group at the University of Wisconsin at Madison. Details of the synthesis method can be found elsewhere.[154] Both NWs and NRs were found on the Si growth substrates, and could be picked up with a sharp tungsten tip.

Because the NWs and NRs are surrounded by approximately $2-4$ nm of native oxide, it is not possible to make electrical connection by directly placing the sample on the suspended device electrodes. Therefore, electrical connection was made by the Pd electrode transfer method discussed in Chapter 2.1.2. First, the sample was transferred to Pd contact pads on a silicon substrate with the use of the tungsten tip. Following electron beam lithography (EBL) exposure of the contact region of the HMS

nanostructure, the sample was placed in a 1 : 6 buffered oxide etch (BOE) solution for 5 seconds to remove the native oxide. This was followed immediately by deposition of 60 nm of Pd metal with e-beam deposition. The sample and Pd contact pads were transferred to the measurement device with an 11% PMMA carrier layer, which was later removed by placing the measurement device in a tube furnace at 350 °C for 3 hours while flowing argon and hydrogen gas. Figure 4.7 shows scanning electron microscopy (SEM) images of two NR samples suspended across the measurement device.
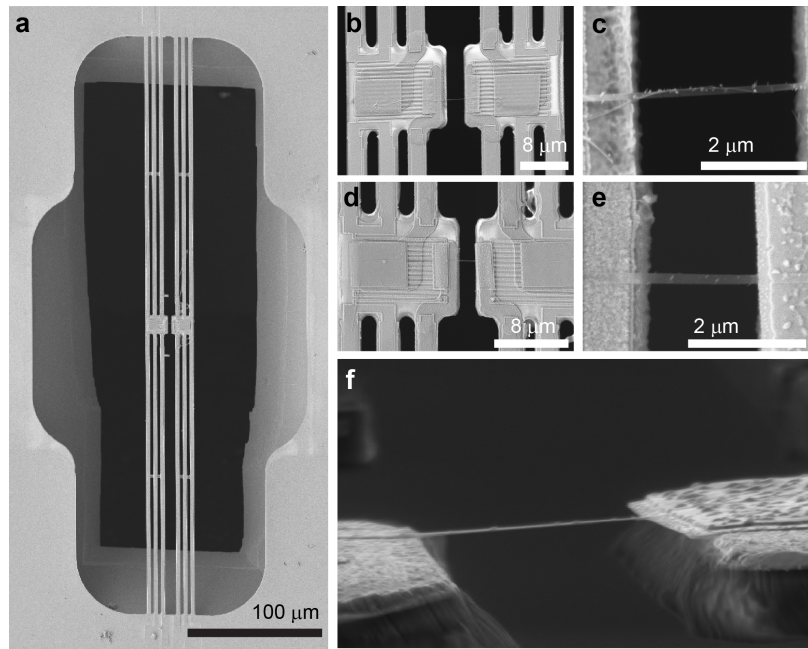

Figure 4.7: (a) Scanning electron microscopy (SEM) images of the suspended measurement devices with 200 μm long suspended beams. (b-c) SEM images of NR2, and (d-e) NR1. (f) 85° tilted SEM image of NR2.

Because the thermal conductance of the sample was expected to be on the order of the background thermal conductance of ~ 0.1 nW/K, the thermal conductance of the sample was measured with the differential background subtraction method discussed in Chapter 2.1.1. In that method, the thermal conductance of the sample is measured relative to a blank device with no sample. Under the assumption that

the background thermal conductance is the same on both devices, the measurement yields the thermal conductance of the sample alone. During the thermal conductance measurements, the thermoelectric voltage was measured between the inner and outer electrodes, in order to determine the thermal contact resistance between the sample and the device membrane according to the four-probe thermal conductance method discussed in Chapter 2.1.1. In addition, the Seebeck coefficient and the four-probe electrical resistance of the same sample, along the same transport direction, was measured with the four electrical connections to the sample.

Following the thermoelectric property measurements, the dimensions and crystalline structure of the sample were measured with SEM, TEM, and atomic force microscopy (AFM). Both samples studied here were found to be NRs with widths of 195 nm (NR1) and 95 nm (NR2), and thicknesses of 24 and 28 nm, respectively. The widths of both samples were determined with TEM, and confirmed with SEM analysis. The thickness of NR1 was measured with AFM while the sample was on the suspended measurement device. The thickness of NR2 was determined from an 85° tilted SEM image. AFM analysis was not possible for NR2 because the NR was twisted on the device membrane.

Following SEM and AFM measurements, the sample was imaged by TEM (FEI Tecnai G2 F30) with a beam voltage of 200 keV. Because the measurement device contains an etched through-hole below the sample, the TEM imaging can be performed while the sample remains on the measurement device.[70] This eliminates any unnecessary handling of the delicate samples. Figures 4.8a-c show high resolution TEM (HRTEM) images of NR1 and NR2, with the indicated crystal axis. The contrast modulation bands observed in Figures 4.8b-c are associated with the mismatch between the Mn and Si sublattice along the c-axis, which results in a long range ordering on the scale of several nanometers. These modulation bands have been observed elsewhere in bulk HMS and HMS nanowires.[154,168] The diffraction pattern from NR1 is shown in Figure 4.8d, which shows bright central peaks associated with the Mn tetragonal sublattice, and closely spaced satellite peaks along the c-axis associated
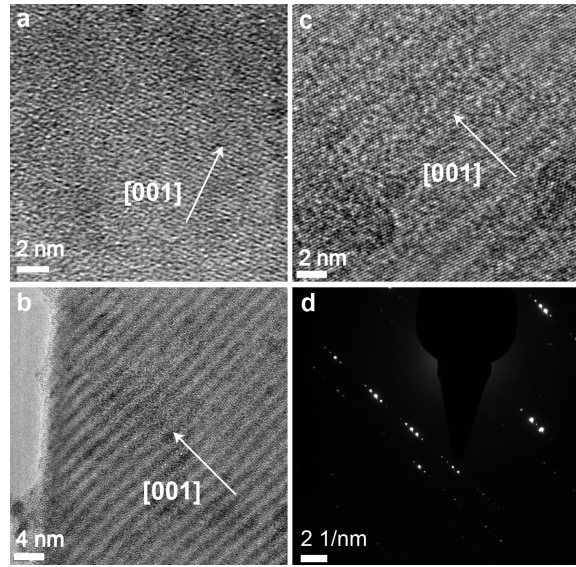
Figure 4.8: Transmission electron microscopy (TEM) analysis of the nanoribbon (NR) samples. (a) High resolution transmission electron microscopy (HRTEM) image of NR2 and (b,c) NR1. (d) Selected area diffraction (SAD) image of NR1 showing the closely spaced satellite peaks associated with the c-axis configuration of the Si sublattice.

with the Si sublattice. The TEM images are used to determine the crystal direction of NR1 and NR2 along the NR axis, which is found to be 32° and 26° from the c-axis, respectively.

It is useful to mention that the TEM imaging of the sample on the suspended measurement device is limited in its resolution and analysis. First of all, with the FEI Tecnai system, the 500 μm thickness of the measurement device permits only the use of the single-tilt holder, which greatly reduces the observable zone axes. In addition, the thickness of the device requires the use of a TEM system with relatively large pole spacing, which limits the resolution compared to higher resolution systems like the JEOL 2010F or the FEI Titan. Furthermore, vibrations of the sample on the SiN suspended membrane are expected to be more pronounced compared to a more heavily damped carbon TEM grid. Under more favorable conditions, it is possible to determine the crystal phase of HMS by determining the position of the satellite

peaks.[154] However, such detailed analysis has not been possible for the HMS samples suspended on the measurement device.

From the TEM images, the thickness of the native oxide is found to be between $2-4$ nm on the lateral sides of the NR. However, the thickness of the oxide on the top and bottom of the NR is not able to be measured. A reasonable assumption is that the oxide thickness on the top and bottom is of comparable thickness as the sides. This would reduce the HMS portion of the NR by approximately $4-8$ nm on the top and bottom. While the thermal conductivity of the oxide is expected to be comparable to the thermal conductivity of HMS, the electrical conductivity of the oxide layer will be zero. Nonetheless, the boundary between the HMS and oxide regions could be an important scattering boundary for phonons.

The thermal conductivities of NR1 and NR2 are shown in Figure 4.9, together with the results from the bulk HMS crystal reported by Zaitsev et al.[17] The reported bulk thermal conductivities along the a- and c-axes are used to calculate the bulk thermal conductivity along the transport direction of the NR, which is at an angle $\theta = 26-32°$ from the c-axis. The bulk thermal conductivities along the NR transport directions are shown as the shaded grey region in Figure 4.9. The thermal conductivities of the NRs, shown as orange and blue symbols, are calculated from the thermal resistance of the sample following the subtraction of the contact thermal resistance according to the four-probe method described in Section 2.1.1. This effective thermal conductivity of the sample consists of both a contribution from the HMS core as well as the native oxide shell. An upper bound to the intrinsic thermal conductivity of the HMS core is calculated by assuming that all sides of the NR have an oxide thickness of 4 nm with negligable thermal conductivity. This upper bound is shown as the upper limit of the orange and blue shaded regions in Figure 4.9. Because a finite thermal conductivity on the order of $\sim 0.1 \, \mathrm{W \, m^{-1} \, K^{-1}}$ is expected for the native oxide, the true thermal conductivity of the HMS portion of the NR should lie somewhere within the shaded region.

The thermal conductivities of the NRs show an increase with temperature, but
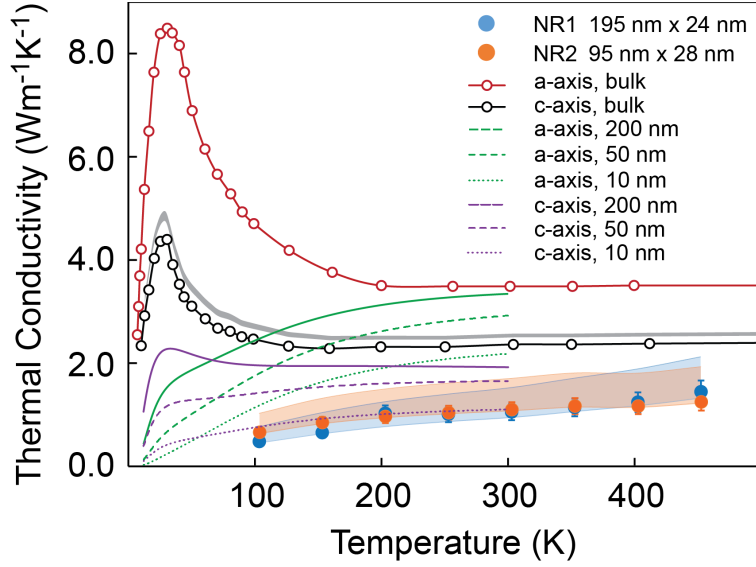
Figure 4.9: Thermal conductivities of NR1 and NR2 (blue and orange symbols) determined from the suspended resistance thermometer measurements with upper bounds (blue and orange shaded regions) for an oxide thickness of 4 nm on all sides and an oxide thermal conductivity of zero. The thermal conductivities of bulk crystalline HMS along the a- and c-axes from Zaitsev et al.[17] are shown as red and black solid lines, respectively. The thermal conductivity along the transport direction of the NRs is shown as the gray shaded region. The lattice thermal conductivity predicted from the diffuson model with various boundary scattering length scales, ℓ_b, is shown for comparison.

are found to be a factor of 1.5 - 2.3 lower than the bulk value at room temperature. In addition, the characteristic low temperature peak in the thermal conductivity of bulk HMS is absent from the NR data. This is indicative of boundary scattering limited transport at low temperature, which tends to suppress the low temperature thermal conductivity peak. The thermal conductivities predicted by the phonon-diffuson model of Eqs. (4.5 - 4.6) are shown as green (a-axis) and purple (c-axis) lines for ℓ_b values of 200, 50, and 10 nm. The thermal conductivities of the NRs agree qualitatively with the model for ℓ_b between $10 - 50$ nm along the c-axis. This is in comparison to the approximately 20 nm thickness of the HMS core of the NRs. Hence, the thermal conductivity of the size-confined NRs is in general agreement with
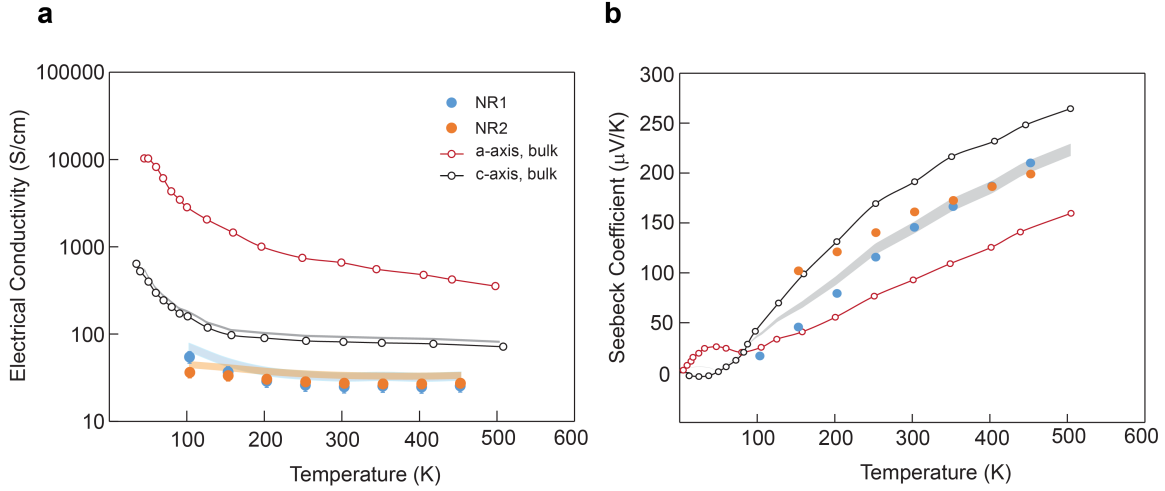
Figure 4.10: (a) Electrical conductivities and (b) Seebeck coefficients of NR1 and NR2. The values for bulk crystalline HMS are shown as black and red solid lines, and the bulk values along the transport direction of the NRs are shown as the gray shaded region. The shaded blue and orange regions in (a) are the ranges in the electrical conductivity for NR1 and NR2, respectively, when an oxide thickness of 2 - 4 nm is assumed for the top and bottom surfaces of the NR.

the boundary scattering effect predicted by the phonon-diffuson model. Nonetheless, defect scattering in the HMS portion of the NR due to crystalline defects and charged impurities could also play a role in the reduced phonon lifetime.

The electrical conductivities and Seebeck coefficients of NR1 and NR2 are shown in Figures 4.10a and 4.10b, respectively, together with the bulk values along the a-axis, c-axis, and along the transport direction of the NR. The Seebeck coefficient agrees well with the bulk values, while the electrical conductivity is approximately an order of magnitude lower than the bulk values along the transport direction of the NR.

To further investigate the electrical properties of the NRs, the Seebeck coefficient and electrical conductivity were used to extract the carrier concentration and mobility. For a two band model in which charge and heat is carried by both holes

and electrons, the Seebeck coefficient for electrons is given by[86,160]

$$S_e = -\frac{k_b}{q}\left[\frac{(r_e + 5/2)F_{r_e+3/2}(\zeta_e)}{(r_e + 3/2)F_{r_e+1/2}(\zeta_e)} - \zeta_e\right] \tag{4.7}$$

where $F_j(\zeta)$ is the Fermi-Dirac integral, $F_n(\zeta) = \int x^n(e^{x-\zeta} + 1)^{-1}\,\mathrm{d}x$, r_e is the exponent in the energy dependent relaxation time of electrons, $\tau_e = \tau_{0,e}(E/k_bT)^{r_e}$, and ζ_e is the reduced electron Fermi level, $\zeta_e = E_F/k_bT$. Likewise, the Seebeck coefficient for holes is given by

$$S_e = \frac{k_b}{q}\left[\frac{(r_h + 5/2)F_{r_h+3/2}(\zeta_h)}{(r_h + 3/2)F_{r_h+1/2}(\zeta_h)} - \zeta_h\right] \tag{4.8}$$

where ζ_h is the reduced hole Fermi level, $\zeta_h = E_{F,h}/k_bT = -(E_F + E_g)/k_bT$, where E_g is the band gap. Again, r_h is the exponent in the energy dependent relaxation time of holes, $\tau_h = \tau_{0,h}(E/k_bT)^{r_h}$. The values of E_F and $E_{F,h}$ are both negative inside the band gap, and are measured from the conduction and valence band, respectively. Electronic band structure calculations from DFT have determined the band gap of HMS to be approximately 0.77 eV.[169] The total Seebeck coefficient considering both electron and hole transport is then found from

$$S = \frac{S_e n\mu_e + S_h p\mu_h}{n\mu_e + p\mu_h} \tag{4.9}$$

which is a function of the carrier mobilities, μ_e and μ_h, and the carrier concentrations, n and p, of electrons and holes, respectively. The carrier concentrations are also functions of the Fermi levels,

$$n = \frac{4\pi}{h^3}(2m_e^*k_bT)^{3/2}F_{1/2}(\zeta_e) \tag{4.10}$$

$$p = \frac{4\pi}{h^3}(2m_h^*k_bT)^{3/2}F_{1/2}(\zeta_h) \tag{4.11}$$

The carrier effective masses, m_h^* and m_e^*, for polycrystalline HMS have previously been found to be $12m_0$ and $9.3m_0$,[160] respectively, where m_0 is the electron mass, while the anisotropy in the effective mass is approximately 35% higher along the c-axis.[153] The mobility ratio, μ_e/μ_h was previously reported to be 0.02 from bulk

mobility measurements.[153,166] Finally, the electrical conductivity can be expressed as separate contributions from electrons and holes,
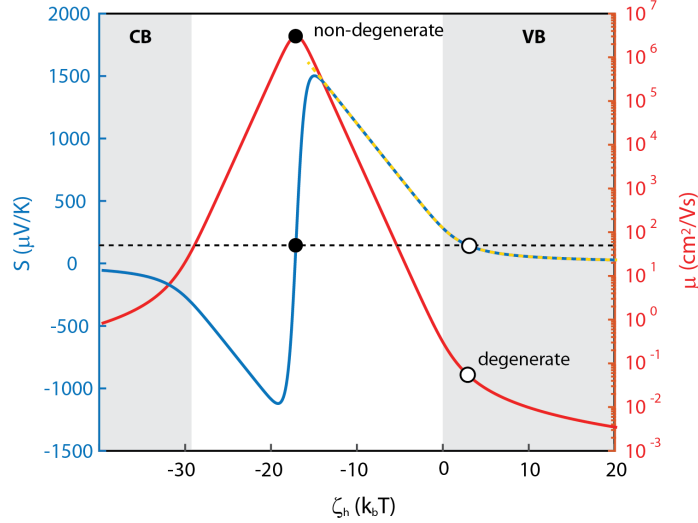
$$\sigma = q(n\mu_e + p\mu_h) \tag{4.12}$$

Figure 4.11: The Seebeck coefficient (left axis, blue curve), and hole mobility (right axis, red curve) as a function of hole Fermi level, ζ_h, at room temperature with $r = +1/2$, and $\sigma = 27$ S/cm. Positive ζ_h is inside the valence band. An experimental Seebeck coefficient of approximately 150 μV/K at room temperature can be obtained from either a non-degenerate or degenerate solution, indicated by solid black circles and open circles, respectively. The solution to the Seebeck coefficient from the single band model for hole transport in shown as the dotted yellow line, which agrees exactly with the two band model in the degenerate limit.

Under the assumption that the mobility ratio in the HMS NRs is comparable to the bulk value, Equations (4.9) and (4.12) are functions of only two variables, E_F and μ_h. Figure 4.11 shows the Seebeck coefficient and hole mobility as a function of ζ_h according to Eqs. (4.9) and (4.12) at $T = 300$ K, $r_e = r_h = +1/2$, and $\sigma = 27$ S/cm. For an experimental Seebeck coefficient of 150 μV/K, there are two solutions to this system of equations, a degenerate solution with a low mobility, and non-degenerate

solution with a high mobility. The plot in Figure 4.11 clearly indicates that the non-degenerate solution is not physical, as the mobility would be seven orders of magnitude higher than the bulk value ($\sim 1\ \mathrm{cm^2\,V^{-1}\,s^{-1}}$).[160] Indeed, the temperature dependence of the electrical conductivity of bulk HMS indicates that it behaves as a degenerate semiconductor. Furthermore, a previous analysis of the Fermi level in bulk HMS nanocomposites has confirmed that the Fermi level is approximately 0.05 eV inside the valence band,[160] which is supported by previous DFT calculations of the band structure of bulk HMS for various phases.[169] The degenerate solution can be determined from a simple single band model in which

$$\sigma = q p \mu_h \tag{4.13}$$

$$S = \frac{k_b}{q}\left[\frac{(r_h + 5/2)F_{r_h+3/2}(\zeta_h)}{(r_h + 3/2)F_{r_h+1/2}(\zeta_h)} - \zeta_h\right] \tag{4.14}$$

The Seebeck coefficient determined from the single band model is plotted as a dotted yellow line in Figure 4.11, which agrees exactly with the two band model in the degenerate limit. Therefore, only the single band model is necessary for this HMS system.

The experimental values of S for NR1 and NR2 at room temperature are used to solve for $E_{F,h}$ according to Eq. (4.14). The Seebeck coefficient in Eq. (4.14) depends on the exponent in the energy dependent relaxation time, r_h, which can range between $-1/2$ to $+3/2$ depending on the scattering mechanism. When the mobility is limited by boundary scattering, the relaxation time is given by $\tau_b = \ell_b/v$, where ℓ_b is the boundary scattering mean free path, and v is the group velocity of holes. The value ℓ_b is generally independent of temperature and energy, as the crystal boundary tends to scatter all charge carriers with equal intensity. In the limit of a quadratic dispersion for holes near the valence band edge, $v \sim E^{1/2}$, which yields $r_h = -1/2$.[185] This value is also applicable to the case of dominant phonon scattering of charge carriers, in which case the mobility scales as $T^{-3/2}$. On the other hand, in the limit of dominant impurity scattering of charge carriers, r_h takes a value of $+3/2$.[74] The

dominant scattered mechanism in the HMS NRs studied here is not known *a priori*, and therefore values between $-1/2$ and $+3/2$ could be possible.

At room temperature, the hole Fermi level, $E_{F,h}$, ranges between $0.02 - 0.11$ eV for NR1 and between $0.03 - 0.12$ eV for NR2, where the ranges correspond to $r = -1/2$ and $r = +3/2$, respectively. Therefore, the Fermi level is inside the valence band and between 1 to 5 $k_b T$ from the band edge, confirming the degenerate nature of HMS. With these values of the Fermi level, the carrier concentration is calculated to be between $0.96 - 5.02 \times 10^{21}$ cm^{-3} for NR1 and between $1.11 - 5.72 \times 10^{21}$ cm^{-3} for NR2. This is comparable to the carrier concentration in bulk HMS, reported to be approximately 2×10^{21} cm^{-3} in bulk, crystalline samples.[153,160,162,186]

The carrier mobility is calculated from $\mu_h = \sigma/pq$, which yields values between $0.034 - 0.20$ cm^2 V^{-1} s^{-1} for NR1 and between $.027 - .14$ cm^2 V^{-1} s^{-1} for NR2, where the ranges now correspond to $r = +3/2$ and $r = -1/2$, respectively. The Hall mobility of holes in bulk HMS has previously been reported to be approximately 2 cm^2 V^{-1} s^{-1} for polycrystalline HMS[160] and approximately 2 cm^2 V^{-1} s^{-1} along the a-axis and 0.3 cm^2 V^{-1} s^{-1} along the c-axis in crystalline HMS.[153] This corresponds to a bulk mobility of approximately 0.4 cm^2 V^{-1} s^{-1} along the transport direction of the NRs. Therefore, the NR carrier mobility is reduced by as much as much as an order of magnitude compared to the bulk value. The reduction in the carrier mobility in the NRs is likely due to defects introduced into the NR system through the addition of charged or neutral impurities. A previous report on the mobility calculated from DFT simulations suggests that the hole mobility can decrease by an order of magnitude when the concentration of neutral impurities is increased by two orders of magnitude.[169] In addition to the reduction in the carrier mobility, the addition of neutral and charged impurities can also contribute to a lower phonon lifetime, which can also partly explain the reduction in the thermal conductivity compared to bulk HMS.

4.4   Summary

The thermal conductivity, electrical conductivity and Seebeck coefficient were measured simultaneously on the same HMS NR samples, and along the same transport direction, using a steady state resistive thermometry method, in which the background thermal conductance and the contact thermal resistance were eliminated in the measurement. The Seebeck coefficient was found to be comparable to the bulk values of crystalline HMS, while the electrical conductivity was approximately an order of magnitude lower than the bulk values. The carrier concentration and hole mobility were solved from the measured Seebeck coefficient and electrical conductivity. The carrier concentration was found to be comparable to the bulk values, while the mobility was reduced by up to one order of magnitude, resulting in an order of magnitude reduction in the electrical conductivity. The low carrier mobility is most likely attributable to the unintentional addition of charged and neutral impurities introduced either in the synthesis of the NRs or in the fabrication of the devices.

The thermal conductivity of the HMS NRs is approximately a factor of two lower than the bulk value along the same transport direction, which indicates that the zT of nanostructured HMS can be improved by a similar factor when the grain size is reduced to be on the order of 10 nm, as long as the charge carrier mobility is not reduced. The highest zT values for HMS have recently been reported to be 0.64 at 823 K and 1.04 at 920 K, in rhenium doped and supersaturated rhenium samples, respectively.[162,163] The HMS grain sizes achieved in the rhenium doped work were on the order of 100 nm. However, the reduction in the lattice thermal conductivity in that work was minimal, as predicted by the phonon-diffuson model results in Figure 4.6. Therefore, reducing the grain size further to the 10 nm scale could result in even further increase in zT. However, the effects of size confinement are expected to be less significant for heavily doped HMS samples with rhenium inclusions, with inherently lower phonon mean free paths compared to pure HMS.[187] A zT greater than 1.0 is necessary to make HMS commercially competitive with the state-of-the-art thermoelectric materials based on PbTe and Bi_2Te_3. While it is unlikely that the

zT of HMS will achieve the values of PbTe and Bi_2Te_3 based systems, the benefit from using abundant and low-cost elements could offer a competitive advantage.

Chapter 5

Use of Brillouin Light Scattering to Investigate the Strain-Dependent Dispersion of Magnons and Phonons

In addition to the heat carried by lattice vibrations and charge carries, magnetic excitations can also carry heat in both magnetic conductors and insulators. For the case of insulators, the electron spins on adjacent lattice sites are coupled via exchange coupling and the dipolar field, and spin transport occurs through the propagation of quantized spin waves, i.e. magnons, which carry an energy ω, a momentum q, and integer spin of $S = -1$. Qualitatively, a magnon is a local reduction in the magnetization distributed over a chain of atoms, and is often schematically drawn as a complete spin precession over adjacent spin sites. The coupling between magnon, phonon, and electron heat carriers is the basis of the emerging field of spincaloritronics,[29,30] which offers new directions in designing thermoelectric energy conversion devices[18,19,188] and spin based logic devices.[23,26]

Like phonons, the contribution to the magnon thermal conductivity in 3-dimensions along the μ direction is given by

$$\kappa_m^\mu = \sum_{\alpha,q} \frac{\partial n}{\partial T} \hbar\omega \left(\frac{\Delta q}{2\pi}\right)^2 v_\alpha^\mu v_\alpha^\mu \tau_\alpha \qquad (5.1)$$

where α sum over all modes with wavevector q, v_α^μ is the mode dependent group velocity along the μ direction, and τ_α is a magnon scattering rate associated with magnon-magnon scattering, elastic magnon-phonon scattering, and elastic magnon-impurity scattering. The inelastic scattering of magnons occurs mostly through the scattering of magnons with phonons, which relaxes the magnon population to local equilibrium

with the phonon bath. This magnon-phonon energy exchange is not generally incorporated into the relaxation time, and is instead treated as a coupling parameter in the magnon-phonon two temperature model.[189,190] The scattering of magnons with phonons can occur through both spin-conserving processes and non-spin-conserving processes. In inelastic spin-conserving processes, such as 4-magnon scattering processes, the magnon energy can equilibrate with the phonon energy through direct energy exchange with the lattice. However, such processes do not relax the magnon spin, only the energy. The relaxation of magnon spin occurs through non-spin-conserving processes, such as 3-magnon scattering processes, in which a nuclear spin interacts with the magnon spin through the spin-orbit interaction.[191] Presumably, the magnon energy relaxation through spin-conserving processes happens much more readily than spin relaxation through the spin-orbit interaction, so that while the magnon energy can rapidly equilibrate with the lattice over $10-100$ nm, the magnon spin diffusion length can be orders of magnitude longer.[66,192,193] Therefore, while the magnon energy distribution may relax very rapidly to the phonon energy distribution, the magnon population can remain out of equilibrium with the phonon population over a much longer distance, with a finite chemical potential.

The heat transported by magnons can be significant in some quasi-one -dimensional ferromagnetic (FM) insulators, such as cuprate spin chain and spin ladder compounds.[22,62,172,194,195] For example, in $Sr_{14}Cu_{24}O_{41}$, the magnons are found to carry as much as 85% of the heat at 150 K.[22] In fact, the magnon thermal conductivity at that temperature is comparable to the room-temperature lattice thermal conductivity of Si.

While the magnitude of the magnon thermal conductivity scales with the magnon group velocity and specific heat, $C_m = \int \hbar \omega D(E)(\partial n/\partial T)\,dE$, the latter of which is typically very small, the amount of heat that can actually be transported by magnons depends strongly on the magnon-phonon coupling. In a material with very strong magnon-phonon coupling, magnon scattering can be very intense and the magnon thermal conductivity can be inherently low. On the other hand, when

magnon-phonon coupling is very weak, it can be difficult to pump enough energy into the magnon population for a significant magnon heat current. Materials with the greatest magnon thermal conductivity probably reside somewhere in between these limits.

Furthermore, the recently discovered spin Seebeck effect (SSE) and reciprocal spin Peltier effect (SPE)[21] are inherently governed by the degree of magnon-phonon and magnon-electron coupling. The spin Seebeck effect occurs in both a longitudinal (LSSE)[20] and transverse (TSSE)[18,19,188,196] geometry, the latter of which has a number of different explanation for the origins of the observed effect. The LSSE is an interfacial effect in which spins are transferred across the interface between a FM insulator and a normal metal (NM) as a result of a temperature gradient across the interface. A NM, such as Pt or Au, is deposited on top of a FM insulator, such as yttrium iron garnet (YIG), and a temperature difference is established between the top and bottom of the device, as shown in Figure 5.1a. A magnetic field is applied along the in-plane direction so that spins are polarized parallel to the NM/FM interface. The temperature gradient generated in the FM generates a magnon heat and spin flux along the temperature gradient as a result of the magnon thermal conductivity or as a result of magnon-phonon drag. At the FM/NM interface, the spin flux in the FM is injected into the NM and converted to a transverse "spin Seebeck" voltage along the y-direction in the NM through the inverse spin Hall effect (ISHE). In addition to the spin Hall angle and resistivity of the NM, and the interfacial quality of the FM/NM interface,[197] the magnitude of the SSE signal also depends on the magnitude of the spin flux, which is inherently related to the magnon-phonon coupling through the magnon decay length.[198]

The SPE, is the spincaloritronic analog to the traditional Peltier effect, and has been observed in nearly the same geometry as the LSSE, except that a current is injected into a Pt transducer on a YIG film. Through the ISHE, a spin accumulation is generated at the Pt/YIG interface, which is absorbed into the YIG through a spin transfer torque.[21] The addition of spins into the YIG either creates or annihilates

95
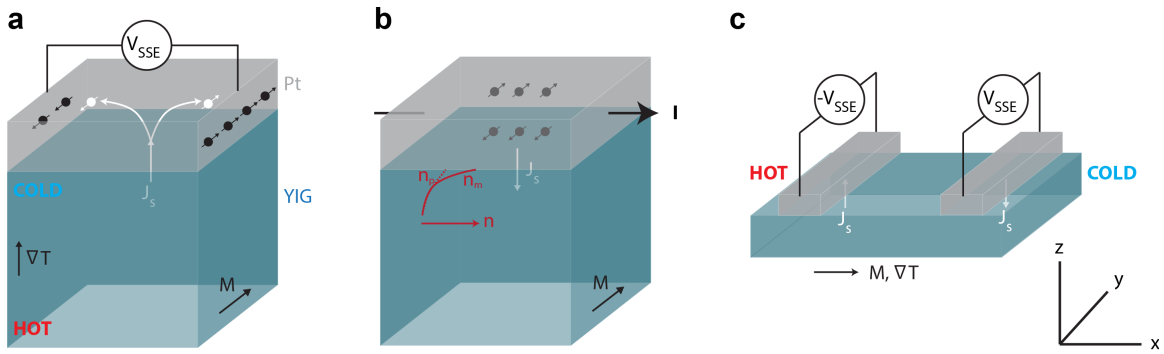
Figure 5.1: Schematic of the (a) longitudinal spin Seebeck effect (LSSE), (b) longitudinal spin Peltier effect (SPE), and (c) transverse spin Seebeck effect (TSSE). (a) A temperature gradient along the z-direction in the YIG generates a voltage along the x direction in the Pt metal as a result of the inverse spin Hall effect (ISHE). (b) A charge current in the Pt transducer generates a spin flux into the YIG, which increases or decreases the local magnon population, n_m, near the interface. This also generates a non-equilibrium in the phonon population, n_p, over the length scale of the magnon-phonon coupling. (c) A temperature gradient along x generates a spin flux along $+z$ or $-z$ depending on the x location, which generates a voltage along y in the Pt metal detector.

a magnon (depending on the direction of the magnetization), thereby heating or cooling the magnon population near the interface, as shown in Figure 5.1b. The magnon energy relaxes to the local phonon energy over a distance on the order of the magnon-phonon energy relaxation length, which depends on the magnon-phonon coupling strength.

The SSE can also be observed in the transverse geometry by applying a temperature gradient transverse to the resulting spin flux. The TSSE is illustrated in Figure 5.1c, which shows a temperature gradient and magnetic field applied along the x-direction of a bulk FM insulator or metal, and NM detection lines patterned on top of the FM along the y-direction. A heat current and resulting spin current are generated in the x-direction as a result of the temperature gradient. If the magnon population in the FM can be pushed out of local equilibrium with the electron temperature in the NM contacts, then some spins will diffuse into the NM contacts, generating a net spin flux in the $\pm$ z-direction. Through the ISHE, this interfacial spin flux is converted to a spin Seebeck voltage along the y-direction. The TSSE was first observed in metallic FM films such as Py,[19] and later in insulating YIG.[188] It has also been observed in semiconducting GaMnAs[18] and the non-magnetic spin-polarized semiconductor InSb,[199] which has no exchange interactions and no magnons. However, unlike the LSSE and SPE, the microscopic origins of the TSSE are not well understood, and have been the subject of debate since its discovery. Namely, the origin of the non-equilibrium in the magnon distribution and driving force of the spin flux in the z-direction is puzzling. A number of theories have suggested that the TSSE depends on a non-equilibrium between the magnon and phonon populations in the FM,[32,196,200] although this has yet to be confirmed experimentally.

Furthermore, the TSSE experiments can be complicated by an unintended temperature gradient in the z-direction as a result of parasitic heat loss from wires or the substrate, or radiation or convective heat loss from the top surface. This temperature gradient in the z-direction can create a spin Seebeck voltage through the LSSE or the anomalous Nernst effect as a result of the magnetic proximity effect

in the Pt.[201,202] In fact, Schreier et al.[203] have shown computationally that parasitic heat loss from the Pt layer that results in a 1 K temperature drop at the top of the Pt can produce an order of magnitude increase in the magnon-electron temperature difference at the YIG/Pt interface, giving rise to unwanted LSSE and Nernst signals. This suggests that the TSSE requires very precise control of unwanted heat loss, and is easily contaminated by a small vertical temperature gradient.

Despite these experimental difficulties, there are a number of interesting observations from SSE measurement. For one, the magnitude of the TSSE voltage depends on the x position along the sample and has odd symmetry about the center of the sample – i.e., the TSSE voltage flips signs at the center of the sample, indicating the direction of the spin flux changes sign. This x-dependence is even observed when the sample, mounted on a non-magnetic substrate, is cut in the middle so that no magnons can propagate along the length of the sample.[18] Although, magnons in each segment can still be out of local equilibrium if the spin relaxation length is long compared to the segments. Indeed, the centimeter length scale over which the TSSE occurs is much greater than the micron length scale of the magnon diffusion, which suggests that the driving mechanism for the TSSE could be explained by phonon mediated transport through the substrate. This was later supported by the fact that the long range TSSE disappears when the magnetic film is deposited on an amorphous substrate, in which localized vibrational modes cannot achieve a long range non-equilibrium distribution of phonons.[204]

Still, the origin of the magnon-phonon non-equilibrium in the FM is further complicated by both experimental and computational studies that have shown that the magnon and phonon populations along the length scale of the sample have nearly identical equivalent temperatures, and therefore, their energies are not out of local equilibrium.[64,203] However, a very small difference in the temperatures of the magnons and phonons, beyond the resolution of the measurements in those works, could be sufficient to generate a magnon-phonon drag effect which can give rise to the induced spin flux. Further insights into the origin of the TSSE effect can be found by consid-

ering the fact that the energy relaxation of phonons is likely mode dependent. The high energy thermal phonons that carry most of the heat can have very short energy relaxation lengths compared to subthermal phonons, with energies less than $k_b T$.[32] These subthermal phonons could deviate from local equilibrium as a result of their long energy relaxation lengths, and therefore can generate long range distributions across the sample. However, this theory has yet to be supported experimentally as it requires spectral resolution of the local phonon population.

Micro-Brillouin light scattering (μ-BLS) provides a powerful method of probing the local magnon and phonon populations at spatial resolutions on the order of the laser spot size, which is typically on the order of 1 μm for a 532 nm laser focused through a 100x objective. This allows for an investigation of the local non-equilibrium between magnon and phonon modes, which is an important component of the SSE theory. A number of recent measurements have demonstrated the use of μ-BLS to measure the local phonon temperature in glass,[65] silicon,[95] and YIG,[66] and the local magnon temperature or magnon population in Py[65] and YIG.[64,66] These measurements have used the temperature dependence of the magnon and phonon peak frequency, intensity or linewidth as a local temperature sensor for the magnon and phonon populations. For example, the phonon frequency is found to downshift with increasing temperature for most materials because of increased bond softening and anharmonic coupling between phonon modes. Likewise, because the magnon frequency scales as the local magnetization, which decreases with temperature, the magnon peak frequency is also found to downshift with temperature for Py and YIG samples.

In previous work that used BLS as a temperature sensor for magnons and phonons, the peak frequencies of the magnon and phonon modes were first calibrated under uniform stage heating, in which all magnon and phonon modes are in equilibrium with a well-defined Bose-Einstein distribution function and zero chemical potential. Then, the system is driven out of equilibrium with the application of a thermal gradient. The local magnon and phonon frequency measured with the

μ-BLS in the presence of this thermal gradient can be converted to an equivalent phonon temperature or magnon population density from the calibrated data. For the case of the magnon population, a finite chemical potential of the non-equilibrium magnon population makes it difficult to extract an equivalent temperature from the distribution function. Therefore, only the magnon population density is considered.

While the change in intensity of a given phonon mode peak is related to the population of just that particular mode, the frequency shift should depends on the population of a range of modes that interact with that mode through anharmonic interactions. Therefore, the peak frequency shift is expected to represent the equivalent temperature of a broadband of thermally excited phonon modes. Likewise, the saturation magnetization depends on the population of all magnon modes in the material, so that the magnon frequency shift will represent the population of all magnon modes in the laser spot.

A very recent measurement by An et al.[66] has used this method to show that when the length scale of this thermal gradient is a few microns in YIG, the order of the magnon diffusion length, the phonon and magnon populations can be driven out of equilibrium. A red laser with a wavelength of 660 nm was used to generate a thermal gradient on the order of $10^6 \, \mathrm{K\,m^{-1}}$ in a bulk YIG cystal. It was is found that at the highest red laser heating values, the magnon population was not relaxed to the equilibrium value at the local phonon temperature. This measurement provides a direct observation of local non-equilibrium in the magnon and phonon populations in YIG, and benefits from being a non-contact method without parasitic thermoelectric effects. However, the effect of laser heating induced strain on the magnon and phonon frequencies remains an important consideration.

5.1 Pressure Dependent Magnon and Phonon Spectra in Yttrium Iron Garnet

In the recent work by An et al.,[66] the magnon population under a $\sim 10^6$ K m^{-1} thermal gradient was found to deviate from the equilibrium value at the local phonon population determined from a uniform stage heating measurement. However, the application of a large laser induced thermal gradient can also cause a difference in strain between the equilibrium calibration at uniform stage heating and the laser heating case. This can cause a systematic error in the magnon and phonon frequency shifts through the associated change in the magneto-optic constants with applied stress. For example, it is well known that the local phonon frequency depends on strain because of a change in the bond stiffness. A previous report has measured the YIG phonon frequency, f_p, under hydrostatic pressure, and has shown that the magnitude of this effect scales as $\Delta f_p/f_p = -\Delta\sigma \times 0.938 \times 10^{-11}$ Pa^{-1} for the [110] longitudinal mode in YIG,[205] where $\Delta\sigma$ is an applied hydrostatic stress. Simulations of the stress and strain tensors by An et al. have determined a nearly hydrostatic stress of 21 MPa at a red laser heating power of 13.2 mW, which corresponds to a phonon frequency shift of approximately 12.7 MHz.[66] The stress induced by the stage heating measurement is found to be an order of magnitude smaller.

Similarly, the magnon frequency also depends on the local strain because of a change in the magneto-elastic energy with crystal deformation. In particular, the values of the magnetization, anisotropy energy, exchange stiffness, and the direction of the magnetization all depends on the volume expansion.[66] From literature values of the stress dependence of the magneto-elastic properties, An et al. determined the total frequency shifts from these strain induced phenomenon to be -0.0089 GHz in the stage heating case and 0.0092 GHz in the laser heating case with a laser power of 13.2 mW. The difference, 0.0003 GHz, is approximately 10 times smaller than the random uncertainty in the magnon peak frequency.

However, to verify the validity of these theoretical calculations, it is necessary to experimentally measure the contribution to the peak shift from applied uniform

stress. Fortunately, this can be achieved by measuring the peak frequency shift under hydrostatic pressure with the variable pressure BLS system described in Chapter 2.2.1. To measure the pressure dependent magnon and phonon frequencies under hydrostatic stress, a YIG sample with the [110] direction normal to the top surface was placed inside a pressure cell with an internal pressure rating up to $10,000$ psi and a sight glass made of 8 mm thick c-axis sapphire. The pressure cell was connected to a 6000 psi argon cylinder through a single-stage regulator that was used adjust the pressure from 0 to 6000 psi (41 MPa).

A 532 laser with an incident power on the pressure cell window of 10.8 mW was used to probe the magnon signal through the sapphire sight glass. An external magnetic field of 600 Oe was applied along the in-plane [110] equivalent direction. The quarter-waveplate was not installed, so that only the scattered light whose polarization was rotated by $90°$ was collected and sent to the interferometer. The Fabry-Perot interferometer was set to a mirror spacing of 12 mm, and 512 channels were scanned between -9.325 GHz and $+9.325$ GHz, corresponding to a spectral resolution of 0.036 GHz. In general, the wavevector of the inelastic magnon mode being probed is equal to the difference in the wavevector of the incident and scattered light, averaged over the light cone from the objective, $\mathbf{q} = \mathbf{k}_s - \mathbf{k}_i$. In the backscattering geometry of this measurement, $\mathbf{k}_s$ was nearly parallel to $\mathbf{k}_i$, and therefore $q = 4\pi n/\lambda = 5.53 \times 10^7$ m^{-1}, compared with the wavevector as the edge of the Brillouin zone of approximately 5×10^9 m^{-1}. Therefore, the magnon mode being probed was a low-wavevector mode, with a corresponding wavelength of 114 nm. That is, a spin wave whose wavelength extends over approximately 100 lattice sites.

Because of the 8 mm thick sapphire sight window, the collected magnon signal was attenuated by approximately a factor of 10 compared to the signal from outside the pressure cell. Therefore, two windows with widths of 2 GHz centered at approximately -7.8 GHz and 7.8 GHz (the Stokes and anti-Stokes magnon peak frequencies) were scanned for 10 times longer than the rest of the spectrum, to make up for a portion of the signal loss.
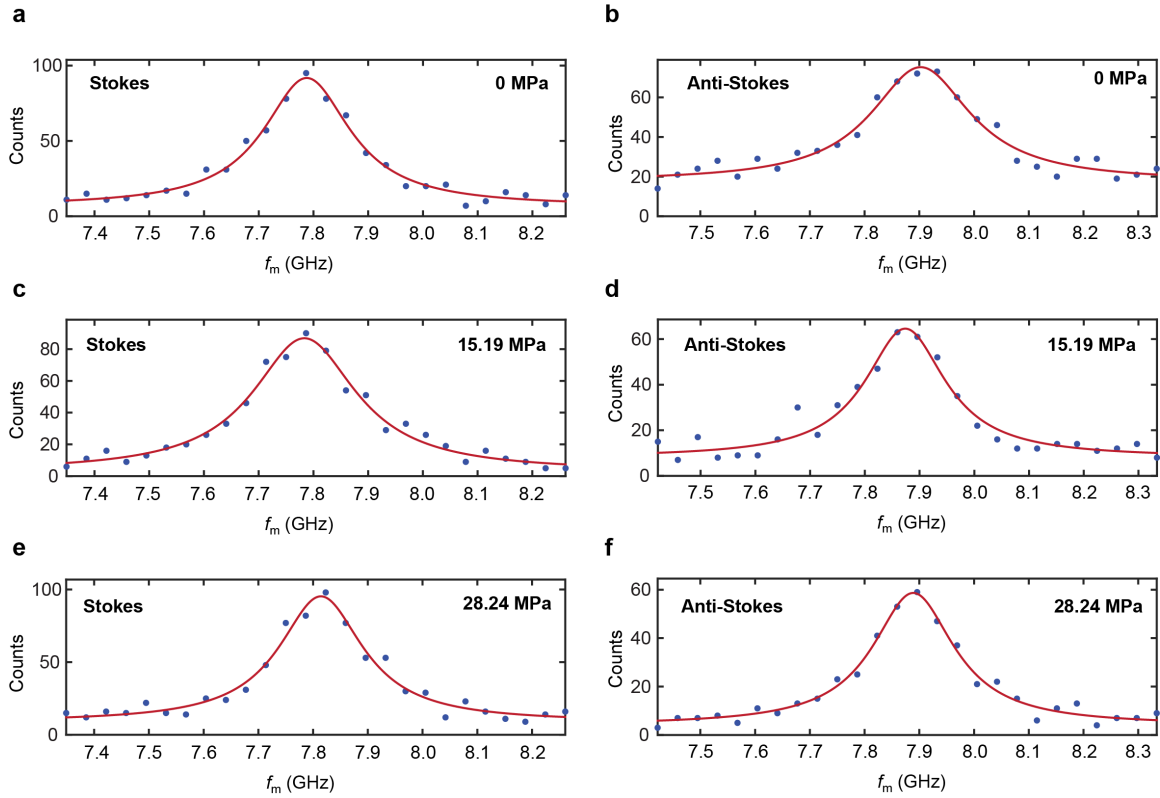
Figure 5.2: Representative Brillouin light scattering spectra of magnons in YIG under hydrostatic pressure. (a) Stokes and (b) anti-Stokes signal at 0 MPa, (c) Stokes and (d) anti-Stokes signal at 15.19 MPa, (e) Stokes and (f) anti-Stokes signal at 28.24 MPa. Red lines are Lorentzian fits to the raw data.
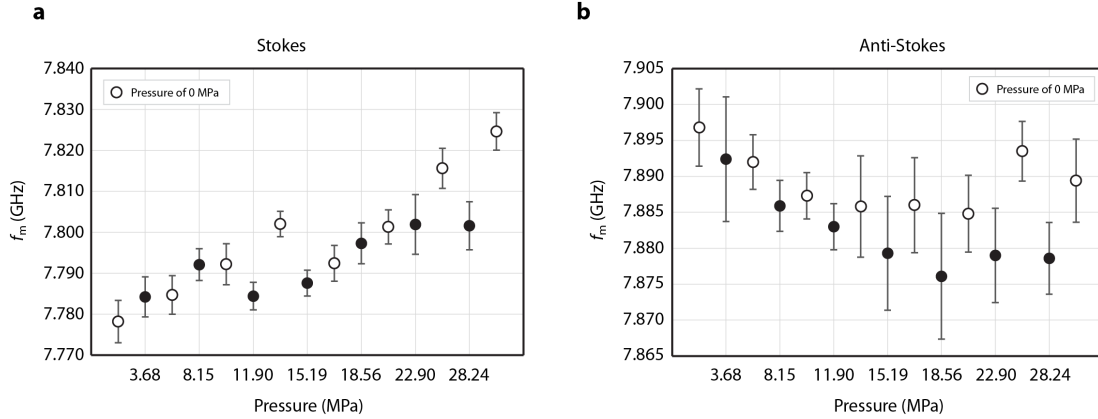
Figure 5.3: Absolute values of the (a) Stokes and (b) anti-Stokes peak frequencies as a function of pressure. The open symbols in between each high pressure measurement were performed at 0 MPa to determine any drift in the frequency over time.

At each pressure, $8 - 17$ two minute acquisitions were recorded for the Stokes and anti-Stokes signals. Representative spectra are shown in Figure 5.2. The frequencies of the Stokes and anti-Stokes signals were determined by fitting a constant background Lorentzian function to the raw data.[206] For each data set, two peak fitting trials were done, and the one with the lowest fitting error was selected. The fitting error, i.e, the percent root mean squared (RMS) difference between the fit and the raw data, was between $4 - 7\%$ for all data sets. At a particular pressure, the Stokes and anti-Stokes peak frequencies of all of the two minute acquisitions were averaged, and the error was determined according to a Student's t-distribution as, $A_{n-1}S/\sqrt{n}$, where A is the critical value of the Students t-distribution for the 95% confidence interval, S is the standard deviation of the peak frequencies, and n is the number of acquisitions (between $8 - 17$). The averaged Stokes and anti-Stokes frequencies are shown in Figure 5.3.

In order to account for any long term drift in the Stokes or anti-Stokes frequencies, a measurement at zero gauge pressure was performed in between each high pressure measurement. These zero pressure measurements are displayed as open symbols in between the high pressure measurements in Figures 5.3 and 5.4. The drift in
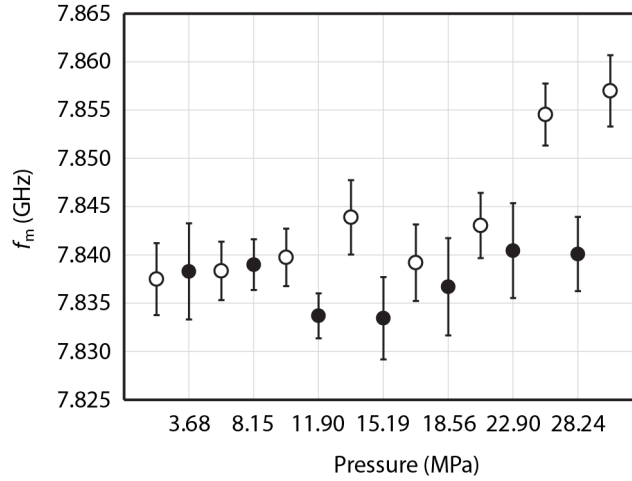
Figure 5.4: The average of the absolute values of the Stokes and anti-Stokes magnon peak frequencies from Figures 5.3a and 5.3b. The open symbols in between each high pressure measurement were performed at 0 MPa to determine any drift in the frequency over time.

the Stokes and anti-Stokes signals is noticeable from Figure 5.3, which show a drift of approximately 0.045 GHz and 0.01 GHz for the Stokes and anti-Stokes signals, respectively, over the course of approximately 12 hours. This drift could be due to thermal expansion (or compression) of the mirror cavities, which could cause the Stokes and anti-Stokes signals to both drift in the same direction of increasing or decreasing frequency magnitude. In addition, there could also be a source of drift that could cause the Stokes and anti-Stokes signals to drift in opposite directions, as evidenced by the data in Figure 5.3. To account for this drift, the average of the absolute values of the Stokes and anti-Stokes frequencies is plotted in Figure 5.4, with an error calculated as $\sqrt{\delta f_S^2 + \delta f_{AS}^2}$, where δf_S and δf_{AS} are the absolute errors in the Stokes and anti-Stokes peak frequencies. This random error in the peak frequency is approximately 0.01 GHz.

The shift in frequency with pressure is within the 0.01 GHz measurement uncertainty, except at the highest pressures of 22.90 and 28.24 MPa. At these pressures, the magnon frequency decreases by approximately 0.02 GHz compared to the other

high pressure measurements and compared to the neighboring zero pressure measurements. This frequency shift was found by An et al.[66] to be less than 12% of the total measured frequency shift under a laser heating power of 19.1 mW. Correcting for this effect results in an even more pronounced non-equilibrium between magnons and phonons measured in that work.

A similar measurement was performed for the phonon peak frequency shift as a function of pressure. Because the phonon signal is about an order of magnitude weaker than the magnon signal, the power incident on the pressure cell was increased to 26 mW. To measure the phonon peak at approximately 63 GHz, the mirror spacing was decreased to 1.4 mm, and the mirrors were scanned from -75 GHz to $+75$ GHz. In order to improve the spectral resolution, 1024 channels were scanned in this frequency range, corresponding to a spectral resolution of 0.15 GHz. The quarter-waveplate was added so that only the scattered signal whose polarization had *not* been rotated by 90° was collected by the interferometer. Because this includes the inelastically scattered light from phonons as well as the strong elastically scattered light reflected from the sample, the sample was tilted inside the pressure cell at an angle of approximately 20° to decrease the contribution from the elastically scattered light.

To achieve a signal-to-noise ratio of approximately 2 to 1, one 20 minute scan was performed at each pressure of 0, 13.8, 0, 27.6, and again 0 MPa. A constant background Lorentzian function was fit to the Stokes and anti-Stokes data by taking the best of six trial fits, and the average of the absolute values of the Stokes and anti-Stokes frequencies, $\bar{f}$, were calculated. Representative spectra of the phonon peak at approximately 63 GHz for the Stokes and anti-Stokes signals are shown in Figure 5.5. To improve the random uncertainty in the measurement, this measurement sequence was performed 13 times. The values of $\bar{f}$ from all 13 data sets are shown in Figure 5.6a. By performing the 0, 13.8, 0, 27.6, 0 MPa measurement sequence 13 isolated times, the overall time between measurements at different pressures was minimized. This ensures that minimal drift in the mirror cavity spacing occurs between different pressure points. While a shift in the mirror cavity spacing may occur between each
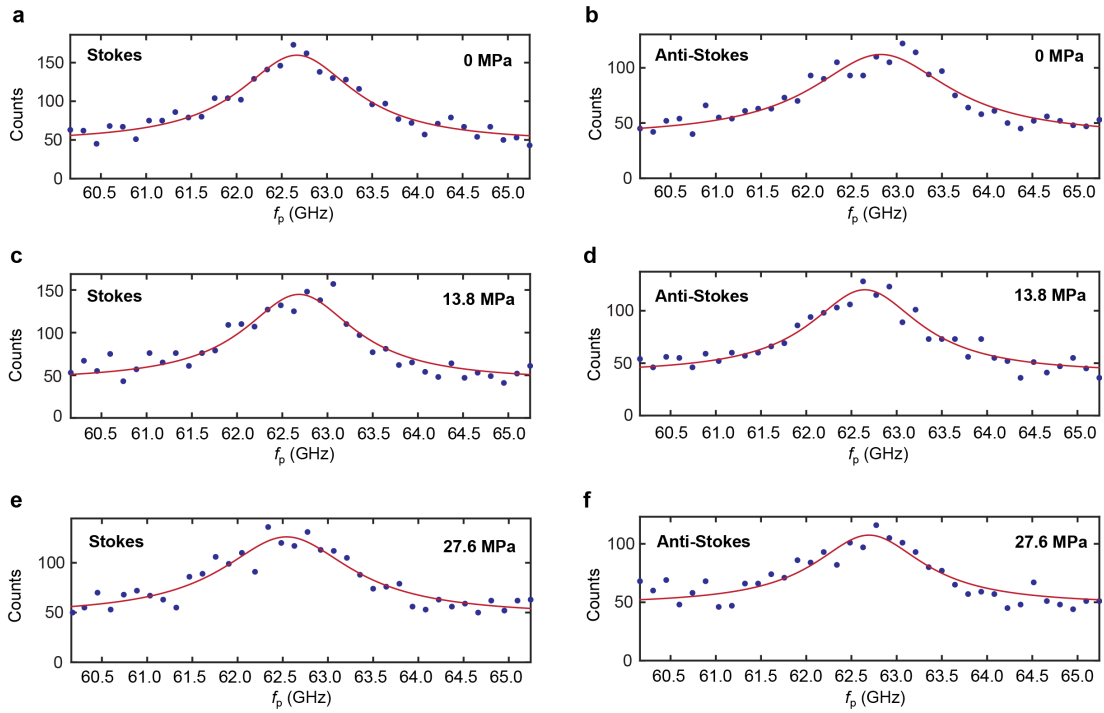
Figure 5.5: Representative Brillouin light scattering spectra of phonons in YIG under hydrostatic pressure. (a) Stokes and (b) anti-Stokes signal at 0 MPa, (c) Stokes and (d) anti-Stokes signal at 13.8 MPa, (e) Stokes and (f) anti-Stokes signal at 27.6 MPa. Red lines are Lorentzian fits to the raw data.
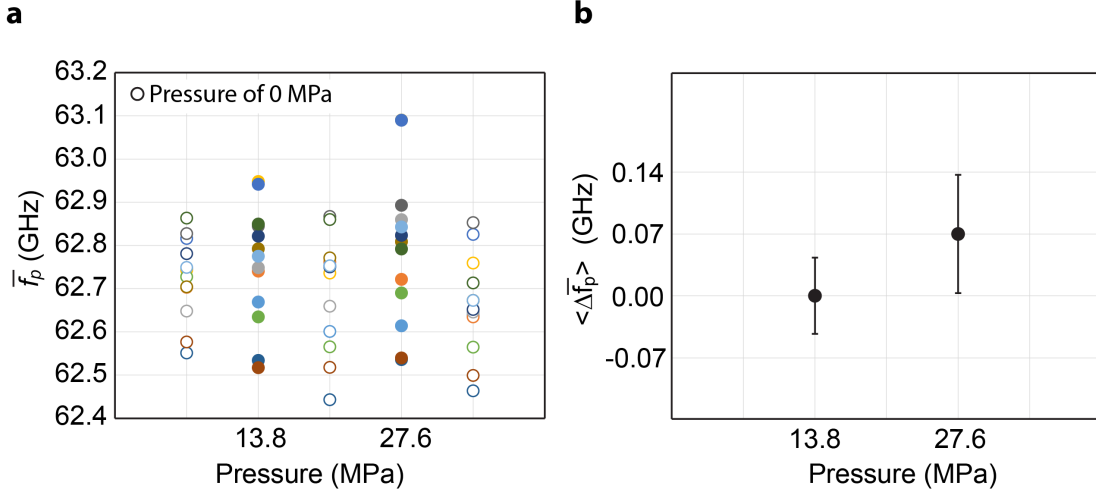
Figure 5.6: (a) Average of the absolute values of the Stokes and anti-Stokes phonon frequencies in YIG under hydrostatic pressure for 13 data sets. The open symbols are measurements at zero gauge pressure. (b) The average frequency shift, $\langle \Delta \bar{f} \rangle$, from 13.8 to 27.8 MPa calculated by taking the average of the 13 measurements shown in (a).

of the 13 data sets, by only considering the change in frequency from zero gauge pressure, this drift can be eliminated.

For each of the 13 data sets, the shift from zero gauge pressure at 13.8 and 27.6 MPa were calculated as $\Delta \bar{f} = \bar{f}_i - \dfrac{\bar{f}_{i-1}(0MPa) + \bar{f}_{i+1}(0MPa)}{2}$, where f_i corresponds to f at 13.8 or 27.6 MPa, and $f_{i-1}(0MPa)$ and $f_{i+1}(0MPa)$ correspond to the zero gauge pressure measurements on either side of f_i. The averages of the $\Delta \bar{f}_i$ over all 13 data sets, $\langle \Delta \bar{f} \rangle$, are plotted in Figure 5.6b, with their values shifted so that $\langle \bar{f} \rangle (13.8MPa) = 0$. The error in the frequency shift is determined from the Student's t-distribution error for the 13 sets of $\Delta \bar{f}_i$. The phonon frequency is found to shift by 0.07 GHz when the pressure is changed by 13.8 MPa. However, this shift is within the random uncertainty between $0.08 - 0.13$ GHz.

5.2 Summary

A variable temperature and pressure μ-BLS system was built in order to investigate the transport and coupling of magnons and phonons in magnetic materials. The hydrostatic pressure dependence of the magnon and phonon frequencies in YIG were investigated to determine the influence of stress induced from localized laser heating. After accounting for systematic drift in the measurements, the magnon frequency was found to decrease by approximately 0.02 GHz at the highest pressures of 22.90 and 28.24 MPa. This frequency shift was found to be less than 12% of the total frequency shift measured by An et al.[66] at the highest laser heating power of 19.1 mW. The results from this work provided important verification of the observed non-equilibrium between the magnon and phonon populations under intense local laser heating. In addition, the establishment of a pressure dependent BLS system allows for further measurements of the effects of hydrostatic stress on the dispersion of magnons and phonons, which can be important in other systems with large thermal gradients or mechanically induced strain.

The variable temperature and pressure μ-BLS system developed in this work is expected to provide a powerful method of probing phonon and magnon transport in magnetic materials with complex magnon-phonon interactions and important applications for spincaloritonic devices. In particular, the combination of high sensitivity resistance thermometry methods and the μ-BLS system provides a unique platform for further measurements of the magnon and phonon populations in spin Seebeck and spin Peltier based devices, and can provide additional insights into the spectral and spatial properties of the non-equilibrium magnon and phonon distributions thought to the drive these phenomena.

Chapter 6

Conclusion

The intent of this work has been to address some of the fundamental questions about the interactions between heat, charge, and spin carriers in complex structured materials, and to understand how these interactions influence the functional properties of materials. In particular, this work has investigated the applicability of the Wiedemann-Franz law and the ratio of heat to charge transport in the conducting polymer poly(3,4-ethylenedioxythiophene) (PEDOT); the dynamics of low energy phonons and high energy diffusons and their influence on the thermal conductivity in higher manganese silicide (HMS) nanostructured samples; and the interactions between heat and spin carriers in the magnetic insulator yttrium iron garnet (YIG).

An understanding of the underlying transport dynamics of these quasiparticles requires sensitive measurement techniques for probing the carrier dispersions and the transport properties, particularly for nanoscale samples. In this work, inelastic neutron scattering (INS) and Brillouin light scattering (BLS) were used to investigate the dispersion of phonons in HMS and the populations of magnons and phonons in YIG bulk crystals. In addition, a variable temperature and pressure BLS system was built for examining the influence of hydrostatic stress on the magnon and phonon frequencies. In addition, microfabricated measurement platforms were further developed to measure all three thermoelectric properties of nanostructured HMS and PEDOT samples along the same transport direction to high resolution with the use of a differential thermal conductance measurement scheme. These experiments have advanced thermal and thermoelectric transport measurements and techniques.

In this work, the Seebeck coefficient, electrical conductivity, and thermal conductivity of PEDOT thin films measured along the same transport direction and on

the same sample were reported. The thermal conductivity was found to increase with electrical conductivity from a minimum of $0.5 \, \mathrm{W \, m^{-1} \, K^{-1}}$, associated with the lattice thermal conductivity for a low electrically conducting sample, to a maximum of $1.8 \, \mathrm{W \, m^{-1} \, K^{-1}}$ for a sample with an electrical conductivity of 350 S/cm. Both the total thermal conductivity and the electronic thermal conductivity of the thin films were found to be significantly larger compared to previous 3ω measurements of PEDOT thin films on insulating substrates that required the deposition of a dielectric and metal film on the sample. In addition, the Lorenz number was found to be greater than that predicted by the Wiedemann-Franz law in the metallic limit. The larger Lorenz number can be explained as a result of hopping conduction of charge carriers through a heterogeneous matrix composed of metallic domains separated by insulating barriers. A structure of this type can also explain the contradictory metallic Seebeck coefficient and non-metallic electrical conductivity measured in these samples. In addition, a bipolar contribution to the thermal conductivity can also contribute to a larger Lorenz number than predicted based on single band transport. These results are expected to motivate further fundamental studies of the complex heat transport mechanisms in conducting polymer systems, which are often characterized by complex heterogeneous structures, quasi-one-dimensional electrical transport, and glassy phonon dynamics.

The thermoelectric properties of suspended higher manganese silicide nanoribbons were also measured along the same transport direction and were analyzed with transmission electron microscopy. The thermal conductivities of nanoribbons with thicknesses of 24 and 28 nm were found to be approximately $1.0 \, \mathrm{W \, m^{-1} \, K^{-1}}$ at room temperature, which is qualitatively consistent with the thermal conductivity predicted from the phonon-diffuson model of thermal transport in bulk HMS nanocomposites with a boundary scattering length scale of 10 nm. The Seebeck coefficient was found to be comparable to bulk HMS, while the electrical conductivity was approximately an order of magnitude lower. From a two band conduction model, the reduction in the electrical conductivity was attributed to a reduced carrier mobility compared

to bulk crystals, likely as a result of increased impurity scattering in the nanostructured samples, which can also explain a reduced phonon lifetime. The reduction in the lattice thermal conductivity by a factor of two compared to bulk is important for optimizing the thermoelectric efficiency of HMS, which is a low-cost, materially abundant alternative to costly, toxic thermoelectric materials.

Lastly, a variable temperature and pressure micro-BLS system was developed for probing the magnetic and vibrational excitations in both magnetic and non-magnetic materials. The magnon and phonon spectra in the magnetic insulator YIG were investigated with BLS under hydrostatic pressure to determine the influence of strain on the magnon and phonon frequencies. After accounting for systematic drift in the measurements, the magnon frequency was found to decrease by approximately 0.02 GHz at the highest pressures of 22.90 and 28.24 MPa.

Future measurements related to the work presented here can provide additional insights into the coupling of energy, charge and spin carriers in these materials. For example, the heterogenous metallic and non-metallic structure of PEDOT and other conducting polymers presents an interesting model system to study the spatial dependence of the thermoelectric properties across crystalline domains. It is possible that the electronic thermal conductivity could be suppressed or the Seebeck coefficient could be improved by designing heterogenous PEDOT films in which charge carrier filtering across grain boundaries could reduce the efficiency of energy transport by the charge carriers, which in turn could also improve the Seebeck coefficient.

In addition, a number of fundamental questions still remain about the complicated lattice dynamics in HMS. Namely, because of the enormous computational expense of *ab initio* calculations of even the simplest HMS phase, it is not yet possible to determine details of the phonon dynamics in larger, disordered structures with multiple HMS phases. The boundaries between HMS phases could provide an important scattering mechanism that influences both the phonon and hole mobilities, as well as provide an energy filtering effect that influences the Seebeck coefficient. Finding the proper parameterized potentials for simulations of larger scale systems

could be important. Such computational advances would also allow for further theoretical investigations to better understand whether high energy modes in HMS are best characterized by diffuson or localized modes. Furthermore, while HMS has become increasingly commercially viable with Re substituted nanocomposites, further improvements in the thermoelectric efficiency could perhaps be achieved with nanostructuring on the 10 nm scale, either through top-down or bottom-up synthesis of bulk nanocomposites.

Finally, the emerging field of spincaloritronics provides a host of promising research directions in understanding the interplay between heat and magnetic transport at microscopic scales. Namely, the use of thermal spin pumping in spin based logic and energy conversion devices and the design of material systems with large magnon thermal conductivity, e.g. for use as a thermal switch, are still in their early stages. Even within the specific subset of this field concerned with the spin Seebeck effect, a number of unanswered questions remain about the long-range driving force for spin injection in macroscale samples. Brillouin light scattering offers a powerful non-contact tool for probing both phonon and magnon dynamics in these systems, to high spectral, spatial, and even temporal resolution. In particular, the combination of the high sensitivity resistance thermometry methods discussed in Chapter 2.1.1 and the micro-Brillouin light scattering technique provides a very powerful measurement platform for studying heat and spin interactions at the microscale. For example, through microwave pumping, it has been demonstrated that a magnon condensate can possibly be formed in YIG.[207] However, the effects of this condensate on the thermal conductivity and on the magnon transport have never been measured, but could provide a fascinating model system for understanding magnon-phonon coupling in a highly non-equilibrium regime. Future efforts in this direction could provide unique solutions to energy conversion technologies and thermal management applications, which is a timely and essential problem to the steadily increasing energy consumption of electronic devices.

Bibliography

1. Pop, E. Energy Dissipation and Transport in Nanoscale Devices. *Nano Research* **3,** 147–169 (2010).
2. Lindsay, L., Broido, D. A. & Reinecke, T. L. First-Principles Determination of Ultrahigh Thermal Conductivity of Boron Arsenide: A Competitor for Diamond? *Physical Review Letters* **111,** 025901 (2013).
3. Jagannadham, K. Multilayer diamond heat spreaders for electronic power devices. *Solid-State Electronics* **42,** 2199–2208 (1998).
4. Seol, J. H., Jo, I., Moore, A. L., Lindsay, L., Aitken, Z. H., Pettes, M. T., Li, X., Yao, Z., Huang, R., Broido, D., Mingo, N., Ruoff, R. S. & Shi, L. Two-Dimensional Phonon Transport in Supported Graphene. *Science* **328,** 213–216 (2010).
5. Cahill, D. G., Braun, P. V., Chen, G., Clarke, D. R., Fan, S., Goodson, K. E., Keblinski, P., King, W. P., Mahan, G. D., Majumdar, A., Maris, H. J., Phillpot, S. R., Pop, E. & Shi, L. Nanoscale thermal transport. II. 2003-2012. *Applied Physics Reviews* **1** (2014).
6. Orr, B., Akbarzadeh, A., Mochizuki, M. & Singh, R. A Review of Car Waste Heat Recovery Systems Utilising Thermoelectric Generators and Heat Pipes. *Applied Thermal Engineering,* in press (2015).
7. Dresselhaus, M. S., Chen, G., Tang, M. Y., Yang, R. G., Lee, H., Wang, D. Z., Ren, Z. F., Fleurial, J. P. & Gogna, P. New Directions for Low-Dimensional Thermoelectric Materials. *Advanced Materials* **19,** 1043–1053 (2007).
8. Snyder, G. J. & Toberer, E. S. Complex thermoelectric materials. *Nature Materials* **7,** 105–114 (2008).
9. Vineis, C. J., Shakouri, A., Majumdar, A. & Kanatzidis, M. G. Nanostructured Thermoelectrics: Big Efficiency Gains from Small Features. *Advanced Materials* **22,** 3970–3980 (2010).
10. Toberer, E. S., Zevalkink, A. & Snyder, G. J. Phonon engineering through crystal chemistry. *Journal of Materials Chemistry* **21,** 15843–15852 (2011).
11. Pei, Y., Wang, H. & Snyder, G. J. Band Engineering of Thermoelectric Materials. *Advanced Materials* **24,** 6125–6135 (2012).
12. Heremans, J. P., Jovovic, V., Toberer, E. S., Saramat, A., Kurosaki, K., Charoenphakdee, A., Yamanaka, S. & Snyder, G. J. Enhancement of Thermoelectric Efficiency in PbTe by Distortion of the Electronic Density of States. *Science* **321,** 554–557 (2008).

13. Zhao, L.-D., Tan, G., Hao, S., He, J., Pei, Y., Chi, H., Wang, H., Gong, S., Xu, H., Dravid, V. P., Uher, C., Snyder, G. J., Wolverton, C. & Kanatzidis, M. G. Ultrahigh power factor and thermoelectric performance in hole-doped single-crystal SnSe. *Science* **351,** 141–144 (2016).

14. Biswas, K., He, J., Blum, I. D., Wu, C.-I., Hogan, T. P., Seidman, D. N., Dravid, V. P. & Kanatzidis, M. G. High-performance bulk thermoelectrics with all-scale hierarchical architectures. *Nature* **489,** 414–418 (2012).

15. Dubey, N. & Leclerc, M. Conducting polymers: Efficient thermoelectric materials. *Journal of Polymer Science Part B: Polymer Physics* **49,** 467–475 (2011).

16. Amatya, R. & Ram, R. J. Trend for Thermoelectric Materials and Their Earth Abundance. *Journal of Electronic Materials* **41,** 1011–1019 (2011).

17. Rowe, D. *CRC Handbook of Thermoelectrics* chap. 25 (CRC Press, 1995).

18. Jaworski, C. M., Yang, J., Mack, S., Awschalom, D. D., Heremans, J. P. & Myers, R. C. Observation of the spin-Seebeck effect in a ferromagnetic semiconductor. *Nature Materials* **9,** 898–903 (2010).

19. Uchida, K., Takahashi, S., Harii, K., Ieda, J., Koshibae, W., Ando, K., Maekawa, S. & Saitoh, E. Observation of the spin Seebeck effect. *Nature* **455,** 778–781 (2008).

20. Uchida, K.-i., Adachi, H., Ota, T., Nakayama, H., Maekawa, S. & Saitoh, E. Observation of longitudinal spin-Seebeck effect in magnetic insulators. *Applied Physics Letters* **97,** 172505 (2010).

21. Flipse, J., Dejene, F. K., Wagenaar, D., Bauer, G. E. W., Youssef, J. B. & van Wees, B. J. Observation of the Spin Peltier Effect for Magnetic Insulators. *Physical Review Letters* **113,** 027601 (2014).

22. Hess, C., Baumann, C., Ammerahl, U., Bchner, B., Heidrich-Meisner, F., Brenig, W. & Revcolevschi, A. Magnon heat transport in $(Sr, Ca, La)_{14}Cu_{24}O_{41}$. *Physical Review B* **64,** 184305 (2001).

23. Choi, G.-M., Moon, C.-H., Min, B.-C., Lee, K.-J. & Cahill, D. G. Thermal spin-transfer torque driven by the spin-dependent Seebeck effect in metallic spin-valves. *Nature Physics* **11,** 576–581 (2015).

24. Hatami, M., Bauer, G. E. W., Zhang, Q. & Kelly, P. J. Thermal Spin-Transfer Torque in Magnetoelectronic Devices. *Physical Review Letters* **99,** 066603 (2007).

25. Yu, H., Granville, S., Yu, D. P. & Ansermet, J. P. Evidence for Thermal Spin-Transfer Torque. *Physical Review Letters* **104,** 146601 (2010).

26. Choi, G.-M., Min, B.-C., Lee, K.-J. & Cahill, D. G. Spin current generated by thermally driven ultrafast demagnetization. *Nature Communications* **5,** 1 (2014).

27. Weiler, M., Althammer, M., Schreier, M., Lotze, J., Pernpeintner, M., Meyer, S., Huebl, H., Gross, R., Kamra, A., Xiao, J., Chen, Y.-T., Jiao, H., Bauer, G. E. W. & Goennenwein, S. T. B. Experimental Test of the Spin Mixing Interface Conductivity Concept. *Physical Review Letters* **111,** 176601 (2013).

28. Jiang, W., Upadhyaya, P., Fan, Y., Zhao, J., Wang, M., Chang, L.-T., Lang, M., Wong, K. L., Lewis, M., Lin, Y.-T., Tang, J., Cherepov, S., Zhou, X., Tserkovnyak, Y., Schwartz, R. N. & Wang, K. L. Direct Imaging of Thermally Driven Domain Wall Motion in Magnetic Insulators. *Physical Review Letters* **110,** 177202 (2013).

29. Bauer, G. E., Saitoh, E. & van Wees, B. J. Spin caloritronics. *Nature Materials* **11,** 391–399 (2012).

30. Boona, S. R., Myers, R. C. & Heremans, J. P. Spin caloritronics. *Energy & Environmental Science* **7,** 885–910 (2014).

31. Boona, S. R. & Heremans, J. P. Magnon thermal mean free path in yttrium iron garnet. *Physical Review B* **90,** 064421 (2014).

32. Tikhonov, K. S., Sinova, J. & Finkelstein, A. M. Spectral non-uniform temperature and non-local heat transfer in the spin Seebeck effect. *Nature Communications* **4,** 1 (2013).

33. Jo, I., Pettes, M. T., Lindsay, L., Ou, E., Weathers, A., Moore, A. L., Yao, Z. & Shi, L. Reexamination of basal plane thermal conductivity of suspended graphene samples measured by electro-thermal micro-bridge methods. *AIP Advances* **5,** 053206 (2015).

34. Cao, Q., Han, S.-J., Tersoff, J., Franklin, A. D., Zhu, Y., Zhang, Z., Tulevski, G. S., Tang, J. & Haensch, W. End-bonded contacts for carbon nanotube transistors with low, size-independent resistance. *Science* **350,** 68–72 (2015).

35. Pop, E. & Goodson, K. E. Thermal Phenomena in Nanoscale Transistors. *Journal of Electronic Packaging* **128,** 102–108 (2006).

36. Chen, Z.-G., Han, G., Yang, L., Cheng, L. & Zou, J. Nanostructured thermoelectric materials: Current research and future challenge. *Progress in Natural Science: Materials International* **22,** 535–549 (2012).

37. Weathers, A. & Shi, L. Thermal transport measurement techniques for nanowires and nanotubes. *Annual Review of Heat Transfer* **vol. 16,** 101–134 (2013).

38. Cahill, D. G. Thermal conductivity measurement from 30 to 750 K: the 3ω method. *Review of Scientific Instruments* **61,** 802–808 (1990).

39. Dhara, S., Solanki, H. S., R, A. P., Singh, V., Sengupta, S., Chalke, B. A., Dhar, A., Gokhale, M., Bhattacharya, A. & Deshmukh, M. M. Tunable thermal conductivity in defect engineered nanowires at low temperatures. *Physical Review B* **84,** 121307 (2011).

40. Lu, L., Yi, W. & Zhang, D. L. 3ω method for specific heat and thermal conductivity measurements. *Review of Scientific Instruments* **72,** 2996–3003 (2001).

41. Ou, M. N., Yang, T. J., Harutyunyan, S. R., Chen, Y. Y., Chen, C. D. & Lai, S. J. Electrical and thermal transport in single nickel nanowire. *Applied Physics Letters* **92,** 063101 (2008).

42. Choi, T.-Y., Poulikakos, D., Tharian, J. & Sennhauser, U. Measurement of the Thermal Conductivity of Individual Carbon Nanotubes by the Four-Point Three-ω Method. *Nano Letters* **6,** 1589–1593 (2006).

43. Guo, J., Wang, X. & Wang, T. Thermal characterization of microscale conductive and nonconductive wires using transient electrothermal technique. *Journal of Applied Physics* **101,** 063537 (2007).

44. Cahill, D. G. Analysis of heat flow in layered structures for time-domain thermoreflectance. *Review of Scientific Instruments* **75,** 5119–5122 (2004).

45. Balandin, A. A., Ghosh, S., Bao, W., Calizo, I., Teweldebrhan, D., Miao, F. & Lau, C. N. Superior Thermal Conductivity of Single-Layer Graphene. *Nano Letters* **8,** 902–907 (2008).

46. Regner, K. T., Sellan, D. P., Su, Z., Amon, C. H., McGaughey, A. J. H. & Malen, J. A. Broadband phonon mean free path contributions to thermal conductivity measured using frequency domain thermoreflectance. *Nature Communications* **4,** 1 (2013).

47. Shen, S., Henry, A., Tong, J., Zheng, R. & Chen, G. Polyethylene nanofibres with very high thermal conductivities. *Nature Nanotechnology* **5,** 251–255 (2010).

48. Fujii, M., Zhang, X., Xie, H., Ago, H., Takahashi, K., Ikuta, T., Abe, H. & Shimizu, T. Measuring the Thermal Conductivity of a Single Carbon Nanotube. *Physical Review Letters* **95,** 065502 (2005).

49. Shi, L., Li, D., Yu, C., Jang, W., Kim, D., Yao, Z., Kim, P. & Majumdar, A. Measuring Thermal and Thermoelectric Properties of One-Dimensional Nanostructures Using a Microfabricated Device. *Journal of Heat Transfer* **125,** 881–888 (2003).

50. Delaire, O., Ma, J., Marty, K., May, A. F., McGuire, M. A., Du, M. H., Singh, D. J., Podlesnyak, A., Ehlers, G., Lumsden, M. D. & Sales, B. C. Giant anharmonic phonon scattering in PbTe. *Nature Materials* **10,** 614–619 (2011).

51. Damascelli, A. Probing the electronic structure of complex systems by ARPES. *Physica Scripta* **2004,** 61 (2004).

52. Minnich, A. J. Advances in the measurement and computation of thermal phonon transport properties. *Journal of Physics: Condensed Matter* **27,** 053202 (2015).

53. Minnich, A. J., Johnson, J. A., Schmidt, A. J., Esfarjani, K., Dresselhaus, M. S., Nelson, K. A. & Chen, G. Thermal Conductivity Spectroscopy Technique to Measure Phonon Mean Free Paths. *Physical Review Letters* **107,** 095901 (2011).

54. Koh, Y. K. & Cahill, D. G. Frequency dependence of the thermal conductivity of semiconductor alloys. *Physical Review B* **76,** 075207 (2007).

55. Griffiths, J. H. E. Anomalous High-frequency Resistance of Ferromagnetic Metals. *Nature* **158,** 670–671 (1946).

56. Hicken, R. J., Barman, A., Kruglyak, V. V. & Ladak, S. Optical ferromagnetic resonance studies of thin film magnetic structures. *Journal of Physics D: Applied Physics* **36,** 2183 (2003).

57. Fleury, P. A., Porto, S. P. S., Cheesman, L. E. & Guggenheim, H. J. Light Scattering by Spin Waves in FeF$_2$. *Physical Review Letters* **17,** 84–87 (1966).

58. Shen, Y. R. Scattering of Light by Magnons. *Journal of Applied Physics* **38,** 1490–1495 (1967).

59. Konstantinovic, M. J. M., Popovi, Z. V., Isobe, M. & Ueda, Y. Raman scattering from magnetic excitations in the spin-ladder compounds CaV$_2$O$_5$ and MgV$_2$O$_5$. *Physical Review B* **61,** 15185–15188 (2000).

60. Popovic, Z., Konstantinovic, M., Ivanov, V., Khuong, O., Gajic, R, Vietkin, A & Moshchalkov, V. Optical properties of the spin-ladder compound Sr$_{14}$Cu$_{24}$O$_{41}$. *Physical Review B* **62,** 4963–4972 (2000).

61. Demidov, V. E., Demokritov, S. O., Hillebrands, B., Laufenberg, M. & Freitas, P. P. Radiation of spin waves by a single micrometer-sized magnetic element. *Applied Physics Letters* **85,** 2866–2868 (2004).

62. Hess, C., Bchner, B., Ammerahl, U., Colonescu, L., Heidrich-Meisner, F., Brenig, W. & Revcolevschi, A. Magnon Heat Transport in Doped La$_2$CuO$_4$. *Physical Review Letters* **90,** 197002 (2003).

63. Hofmann, M., Lorenz, T., Berggold, K., Grninger, M., Freimuth, A., Uhrig, G. S. & Brck, E. Evidence for a large magnetic heat current in insulating layered cuprates. *Physical Review B* **67,** 184502 (2003).

64. Agrawal, M., Vasyuchka, V. I., Serga, A. A., Karenowska, A. D., Melkov, G. A. & Hillebrands, B. Direct Measurement of Magnon Temperature: New Insight into Magnon-Phonon Coupling in Magnetic Insulators. *Physical Review Letters* **111,** 107204 (2013).

65. Birt, D. R., An, K., Weathers, A., Shi, L., Tsoi, M. & Li, X. Brillouin light scattering spectra as local temperature sensors for thermal magnons and acoustic phonons. *Applied Physics Letters* **102,** 082401 (2013).

66. An, K., Olsson, K. S., Weathers, A., Sullivan, S., Chen, X., Li, X., Marshall, L. G., Ma, X., Klimovich, N., Zhou, J., Shi, L. & Li, X. Magnons and Phonons Optically Driven Out of Local Equilibrium in a Magnetic Insulator. *arXiv preprint arXiv:1601.01982* (2016).

67. Shi, L. *Thermophysical measurements of microstructures and carbon nanotubes* PhD Thesis (The University of California - Berkeley, 2001).

68. Kim, P, Shi, L., Majumdar, A & McEuen, P. Thermal transport measurements of individual multiwalled nanotubes. *Physical Review Letters* **87,** 215502 (2001).

69. Xu, X., Pereira, L. F. C., Wang, Y., Wu, J., Zhang, K., Zhao, X., Bae, S., Tinh Bui, C., Xie, R., Thong, J. T. L., Hong, B. H., Loh, K. P., Donadio, D., Li, B. &

zyilmaz, B. Length-dependent thermal conductivity in suspended single-layer graphene. *Nature Communications* **5,** 1 (2014).

70. Pettes, M. T. & Shi, L. Thermal and Structural Characterizations of Individual Single-, Double-, and Multi-Walled Carbon Nanotubes. *Advanced Functional Materials* **19,** 3918–3925 (2009).

71. Mavrokefalos, A., Pettes, M. T., Zhou, F. & Shi, L. Four-probe measurements of the in-plane thermoelectric properties of nanofilms. *Review of Scientific Instruments* **78** (2007).

72. Moore, A. L., Cummings, A. T., Jensen, J. M., Shi, L. & Koo, J. H. Thermal conductivity measurements of nylon 11-carbon nanofiber nanocomposites. *Journal of Heat Transfer* **131,** 091602 (2009).

73. Zhou, F., Moore, A. L., Bolinsson, J., Persson, A., Frberg, L., Pettes, M. T., Kong, H., Rabenberg, L., Caroff, P. & Stewart, D. A. Thermal conductivity of indium arsenide nanowires with wurtzite and zinc blende phases. *Physical Review B* **83,** 205416 (2011).

74. Zhou, F., Szczech, J., Pettes, M. T., Moore, A. L., Jin, S. & Shi, L. Determination of Transport Properties in Chromium Disilicide Nanowires via Combined Thermoelectric and Structural Characterizations. *Nano Letters* **7,** 1649–1654 (2007).

75. Bi, K., Weathers, A., Matsushita, S., Pettes, M. T., Goh, M., Akagi, K. & Shi, L. Iodine doping effects on the lattice thermal conductivity of oxidized polyacetylene nanofibers. *Journal of Applied Physics* **114,** 194302 (2013).

76. Weathers, A., Khan, Z. U., Brooke, R., Evans, D., Pettes, M. T., Andreasen, J. W., Crispin, X. & Shi, L. Significant Electronic Thermal Transport in the Conducting Polymer Poly (3, 4-ethylenedioxythiophene). *Advanced Materials* **27,** 2101–2106 (2015).

77. Weathers, A., Bi, K., Pettes, M. T. & Shi, L. Reexamination of thermal transport measurements of a low-thermal conductance nanowire with a suspended micro-device. *Review of Scientific Instruments* **84,** 084903 (2013).

78. Kim, J., Ou, E., Sellan, D. P. & Shi, L. A four-probe thermal transport measurement method for nanostructures. *Review of Scientific Instruments* **86,** 044901 (2015).

79. Wingert, M. C., Chen, Z. C. Y., Kwon, S., Xiang, J. & Chen, R. Ultra-sensitive thermal conductance measurement of one-dimensional nanostructures enhanced by differential bridge. *Review of Scientific Instruments* **83,** 024901 (2012).

80. Weathers, A. *Thermal and Thermoelectric Transport in Organic and Inorganic Nanostuctures* MSE Thesis (The University of Texas at Austin, 2012).

81. Moore, A. L. & Shi, L. On errors in thermal conductivity measurements of suspended and supported nanowires using micro-thermometer devices from low to high temperatures. *Measurement Science and Technology* **22,** 015103 (2011).

82. Jo, I., Pettes, M. T., Kim, J. H., Watanabe, K., Taniguchi, T., Yao, Z. & Shi, L. Thermal Conductivity and Phonon Transport in Suspended Few-Layer Hexagonal Boron Nitride. *Nano Letters* **13,** 550554 (2013).

83. Greco, F., Zucca, A., Taccola, S., Menciassi, A., Fujie, T., Haniuda, H., Takeoka, S., Dario, P. & Mattoli, V. Ultra-thin conductive free-standing PEDOT/PSS nanofilms. *Soft Matter* **7,** 10642–10650 (2011).

84. Moore, A. L., Pettes, M. T., Zhou, F. & Shi, L. Thermal conductivity suppression in bismuth nanowires. *Journal of Applied Physics* **106,** 034310 (2009).

85. Nam, C. Y., Kim, J. Y. & Fischer, J. E. Focused-ion-beam platinum nanopatterning for GaN nanowires: Ohmic contacts and patterned growth. *Applied Physics Letters* **86,** 193112 (2005).

86. Mavrokefalos, A., Moore, A. L., Pettes, M. T., Shi, L., Wang, W. & Li, X. Thermoelectric and structural characterizations of individual electrodeposited bismuth telluride nanowires. *Journal of Applied Physics* **105,** 104318 (2009).

87. Pettes, M. T., Maassen, J., Jo, I., Lundstrom, M. & Shi, L. Effects of Surface Band Bending and Scattering on Thermoelectric Transport in Suspended Bismuth Telluride Nanoplates. *Nano Letters* **13,** 53165322 (2013).

88. Li, X., Zhu, Y., Cai, W., Borysiak, M., Han, B., Chen, D., Piner, R. D., Colombo, L. & Ruoff, R. S. Transfer of Large-Area Graphene Films for High-Performance Transparent Conductive Electrodes. *Nano Letters* **9,** 4359–4363 (2009).

89. Ferrari, A. C. Raman spectroscopy of graphene and graphite: Disorder, electron-phonon coupling, doping and nonadiabatic effects. *Solid State Communications* **143,** 47–57 (2007).

90. Pettes, M. T., Sadeghi, M. M., Ji, H., Jo, I., Wu, W., Ruoff, R. S. & Shi, L. Scattering of phonons by high-concentration isotopic impurities in ultrathin graphite. *Physical Review B* **91,** 035429 (2015).

91. Richter, H., Wang, Z. P. & Ley, L. The one phonon Raman spectrum in microcrystalline silicon. *Solid State Communications* **39,** 625–629 (1981).

92. Cai, W. W., Moore, A. L., Zhu, Y., Li, X., Chen, S., Shi, L. & Ruoff, R. S. Thermal Transport in Suspended and Supported Monolayer Graphene Grown by Chemical Vapor Deposition. *Nano Letters* **10,** 16451651 (2010).

93. Sullivan, S., Kholmanov, I. & Shi, L. Optical Generation and Detection of Local Non-equilibrium Phonons in Suspended Graphene. *In preparation* (2016).

94. Wettling, W., Cottam, M. G. & Sandercock, J. R. The relation between one-magnon light scattering and the complex magneto-optic effects in YIG. *Journal of Physics C: Solid State Physics* **8,** 211 (1975).

95. Olsson, K. S., Klimovish, N., An, K., Sullivan, S., Weathers, A., Shi, L. & Li, X. Temperature Dependence of Brillouin Light Spectra of Acoustic Phonons in Silicon. *Applied Physics Letters* **106,** 051906 (2015).

96. Mock, R., Hillebrands, B. & Sandercock, R. Construction and performance of a Brillouin scattering set-up using a triple-pass tandem Fabry-Perot interferometer. *Journal of Physics E: Scientific Instruments* **20,** 656 (1987).

97. Demokritov, S. O. & Demidov, V. E. Micro-Brillouin Light Scattering Spectroscopy of Magnetic Nanostructures. *IEEE Transactions on Magnetics* **44,** 6–12 (2008).

98. Lee, S. A., Pinnick, D. A., Lindsay, S. M. & Hanson, R. C. Elastic and photoelastic anisotropy of solid HF at high pressure. *Physical Review B* **34,** 2799–2806 (1986).

99. Nayak, A. P., Bhattacharyya, S., Zhu, J., Liu, J., Wu, X., Pandey, T., Jin, C., Singh, A. K., Akinwande, D. & Lin, J.-F. Pressure-induced semiconducting to metallic transition in multilayered molybdenum disulphide. *Nature Communications* **5,** 1 (2014).

100. Nayak, A. P., Pandey, T., Voiry, D., Liu, J., Moran, S. T., Sharma, A., Tan, C., Chen, C.-H., Li, L.-J., Chhowalla, M., Lin, J.-F., Singh, A. K. & Akinwande, D. Pressure-Dependent Optical and Vibrational Properties of Monolayer Molybdenum Disulfide. *Nano Letters* **15,** 346–353 (2015).

101. Nayak, A. P., Yuan, Z., Cao, B., Liu, J., Wu, J., Moran, S. T., Li, T., Akinwande, D., Jin, C. & Lin, J.-F. Pressure-Modulated Conductivity, Carrier Density, and Mobility of Multilayered Tungsten Disulfide. *ACS Nano* **9,** 9117–9123 (2015).

102. Shimizu, H., Brody, E. M., Mao, H. K. & Bell, P. M. Brillouin Measurements of Solid n-H_2 and n-D_2 to 200 kbar at Room Temperature. *Physical Review Letters* **47,** 128–131 (1981).

103. Polian, A. Brillouin scattering at high pressure: an overview. *Journal of Raman Spectroscopy* **34,** 633–637 (2003).

104. Singh, V., Bougher, T. L., Weathers, A., Cai, Y., Bi, K., Pettes, M. T., McMenamin, S. A., Lv, W., Resler, D. P., Gattuso, T. R., Altman, D. H., Sandhage, K. H., Shi, L., Henry, A. & Cola, B. A. High thermal conductivity of chain-oriented amorphous polythiophene. *Nature Nanotechnology* **9,** 384–390 (2014).

105. Chiang, C. K., Fincher, C. R., Park, Y. W., Heeger, A. J., Shirakawa, H., Louis, E. J., Gau, S. C. & MacDiarmid, A. G. Electrical Conductivity in Doped Polyacetylene. *Physical Review Letters* **39,** 1098–1101 (1977).

106. Shirakawa, H., Louis, E. J., MacDiarmid, A. G., Chiang, C. K. & Heeger, A. J. Synthesis of electrically conducting organic polymers: halogen derivatives of polyacetylene, (CH). *Journal of the Chemical Society, Chemical Communications* **16,** 578–580 (1977).

107. Burroughes, J. H., Bradley, D. D. C., Brown, A. R., Marks, R. N., Mackay, K., Friend, R. H., Burns, P. L. & Holmes, A. B. Light-emitting diodes based on conjugated polymers. *Nature* **347,** 539–541 (1990).

108. Bao, Z., Dodabalapur, A. & Lovinger, A. J. Soluble and processable regioregular poly(3-hexylthiophene) for thin film fieldeffect transistor applications with high mobility. *Applied Physics Letters* **69,** 4108–4110 (1996).

109. Yang, Y., Ouyang, J., Ma, L., Tseng, R. J. H. & Chu, C. W. Electrical Switching and Bistability in Organic/Polymeric Thin Films and Memory Devices. *Advanced Functional Materials* **16,** 1001–1014 (2006).

110. Li, G., Zhu, R. & Yang, Y. Polymer solar cells. *Nature Photonics* **6,** 153–161 (2012).

111. Yan, H., Chen, Z., Zheng, Y., Newman, C., Quinn, J. R., Dotz, F., Kastler, M. & Facchetti, A. A high-mobility electron-transporting polymer for printed transistors. *Nature* **457,** 679–686 (2009).

112. deGans, B. J., Duineveld, P. C. & Schubert, U. S. Inkjet Printing of Polymers: State of the Art and Future Developments. *Advanced Materials* **16,** 203–213 (2004).

113. Kaiser, A. B. Systematic Conductivity Behavior in Conducting Polymers: Effects of Heterogeneous Disorder. *Advanced Materials* **13,** 927–941 (2001).

114. Salleo, A., Kline, R. J., DeLongchamp, D. M. & Chabinyc, M. L. Microstructural Characterization and Charge Transport in Thin Films of Conjugated Polymers. *Advanced Materials* **22,** 3812–3838 (2010).

115. Park, T., Park, C., Kim, B., Shin, H. & Kim, E. Flexible PEDOT electrodes with large thermoelectric power factors to generate electricity by the touch of fingertips. *Energy & Environmental Science* **6,** 788–792 (2013).

116. He, M., Qiu, F. & Lin, Z. Towards high-performance polymer-based thermoelectric materials. *Energy & Environmental Science* **6,** 1352–1361 (2013).

117. Jun, L., Lian-meng, Z., Li, H. & Xin-feng, T. Synthesis and thermoelectric properties of polyaniline. *Journal of Wuhan University of Technology-Mater. Sci. Ed.* **18,** 53–55 (2003).

118. Kemp, N. T., Kaiser, A. B., Liu, C. J., Chapman, B., Mercier, O., Carr, A. M., Trodahl, H. J., Buckley, R. G., Partridge, A. C., Lee, J. Y., Kim, C. Y., Bartl, A., Dunsch, L., Smith, W. T. & Shapiro, J. S. Thermoelectric power and conductivity of different types of polypyrrole. *Journal of Polymer Science Part B: Polymer Physics* **37,** 953–960 (1999).

119. Aich, R. B., Blouin, N., Bouchard, A. & Leclerc, M. Electrical and Thermoelectric Properties of Poly(2,7-Carbazole) Derivatives. *Chemistry of Materials* **21,** 751–757 (2009).

120. Bubnova, O., Khan, Z. U., Wang, H., Braun, S., Evans, D. R., Fabretto, M., Hojati-Talemi, P., Dagnelund, D., Arlin, J.-B., Yves H. Geerts, S. D., Breiby, D. W., Andreasen, J. W., Lazzaroni, R., Chen, W. M., Zozoulenko, I., Fahlman, M., Murphy, P. J., Berggren, M. & Crispin, X. Semi-metallic polymers. *Nature Materials* **13,** 190–194 (2014).

121. Bubnova, O., Khan, Z. U., Malti, A., Braun, S., Fahlman, M., Berggren, M. & Crispin, X. Optimization of the thermoelectric figure of merit in the conducting polymer poly(3,4-ethylenedioxythiophene). *Nature Materials* **10,** 429 –433 (2011).

122. Kim, G.-H., Shao, L., Zhang, K. & Pipe, K. P. Engineered doping of organic semiconductors for enhanced thermoelectric efficiency. *Nature Materials* **12,** 719 –723 (2013).

123. Tritt, T. M. *Thermal Conductivity: Theory, Properties, and Applications* (Kluwer Academic / Plenum Publishers, New York, 2004).

124. Moses, D. & Denenstein, A. Experimental determination of the thermal conductivity of a conducting polymer: Pure and heavily doped polyacetylene. *Physical Review B* **30,** 2090–2097 (1984).

125. Yoon, H., Jung, B. S. & Lee, H. Correlation between electrical conductivity, thermal conductivity, and ESR intensity of polyaniline. *Synthetic Metals* **41,** 699–702 (1991).

126. Nardes, A. M., Kemerink, M., Janssen, R. A. J., Bastiaansen, J. A. M., Kiggen, N. M. M., Langeveld, B. M. W., vanBreemen, A. J. J. M. & deKok, M. M. Microscopic Understanding of the Anisotropic Conductivity of PEDOT:PSS Thin Films. *Advanced Materials* **19,** 1196–1200 (2007).

127. Ju, Y. S., Kurabayashi, K. & Goodson, K. E. Thermal characterization of anisotropic thin dielectric films using harmonic Joule heating. *Thin Solid Films* **339,** 160–164 (1999).

128. Mishra, V., Hardin, C. L., Garay, J. E. & Dames, C. A 3 omega method to measure an arbitrary anisotropic thermal conductivity tensor. *Review of Scientific Instruments* **86,** 054902 (2015).

129. Tian, Z., Lee, S. & Chen, G. A comprehensive review of heat transfer in thermoelectric materials and devices. *Annual Review of Heat Transfer* **17,** 425–483 (2014).

130. Nolas, G., Sharp, J. & Goldsmid, J. *Thermoelectrics: Basic Principles and New Materials Developments* (Springer Berlin Heidelberg, 2001).

131. Seeger, K. *Semiconductor Physics: An Introduction* 6th ed. (Springer, Berlin, 1997).

132. Kumar, G. S., Prasad, G. & Pohl, R. O. Experimental determinations of the Lorenz number. *Journal of Materials Science* **28,** 4261–4272 (1993).

133. Chester, G. V. & Thellung, A. The Law of Wiedemann and Franz. *Proceedings of the Physical Society* **77,** 1005 (1961).

134. Huang, B.-L. & Kaviany, M. *Ab initio* and molecular dynamics predictions for electron and phonon transport in bismuth telluride. *Physical Review B* **77,** 125209 (2008).

135. Kane, C. L. & Fisher, M. P. A. Thermal Transport in a Luttinger Liquid. *Physical Review Letters* **76,** 3192–3195 (1996).

136. Li, M. R. & Orignac, E. Heat conduction and Wiedemann-Franz law in disordered Luttinger liquids. *EPL (Europhysics Letters)* **60,** 432 (2002).

137. Voit, J. One-dimensional Fermi liquids. *Reports on Progress in Physics* **58,** 977 (1995).

138. Aleshin, A. N., Lee, H. J., Park, Y. W. & Akagi, K. One-Dimensional Transport in Polymer Nanofibers. *Physical Review Letters* **93,** 196601 (2004).

139. Mott, N. & Davis, E. *Electronic Processes in Non-Crystalline Materials* (OUP Oxford, 2012).

140. Ashcroft, N. & Mermin, N. *Solid State Physics* (Holt, Rinehart and Winston, 1976).

141. Cutler, M. & Mott, N. F. Observation of Anderson Localization in an Electron Gas. *Physical Review* **181,** 1336–1340 (1969).

142. Winther-Jensen, B. & West, K. Vapor-Phase Polymerization of 3,4- ethylenedioxythiophene: A Route to Highly Conducting Polymer Surface Layers. *Macromolecules* **37,** 4538–4543 (2004).

143. Evans, D., Fabretto, M., Mueller, M., Zuber, K., Short, R. & Murphy, P. Structure-directed growth of high conductivity PEDOT from liquid-like oxidant layers during vacuum vapor phase polymerization. *Journal of Materials Chemistry* **22,** 14889–14895 (2012).

144. Liu, C., Lu, B., Yan, J., Xu, J., Yue, R., Zhu, Z., Zhou, S., Hu, X., Zhang, Z. & Chen, P. Highly conducting free-standing poly(3,4-ethylenedioxythiophene)/ poly(styrenesulfonate) films with improved thermoelectric performances. *Synthetic Metals* **160,** 2481–2485 (2010).

145. Kaiser, A. B. Electronic transport properties of conducting polymers and carbon nanotubes. *Reports on Progress in Physics* **64,** 1 (2001).

146. Khan, Z. U., Bubnova, O., Jafari, M. J., Brooke, R., Liu, X., Gabrielsson, R., Ederth, T., Evans, D. R., Andreasen, J. W., Fahlman, M. & Crispin, X. Acido-basic control of the thermoelectric properties of poly(3,4- ethylenedioxythiophene)tosylate (PEDOT-Tos) thin films. *Journal of Materials Chemistry C* **3,** 10616–10623 (2015).

147. Wang, X., Ho, V., Segalman, R. A. & Cahill, D. G. Thermal Conductivity of High-Modulus Polymer Fibers. *Macromolecules* **46,** 4937–4943 (2013).

148. Liu, J., Wang, X., Li, D., Coates, N. E., Segalman, R. A. & Cahill, D. G. Thermal Conductivity and Elastic Constants of PEDOT:PSS with High Electrical Conductivity. *Macromolecules* **48,** 585–591 (2015).

149. Aleshin, A. N., Williams, S. R. & Heeger, A. J. Transport Properties of Poly(3,4-ethylenedioxythiophene)/poly(styrenesulfonate). *Synthetic Metals* **94,** 173–177 (1998).

150. Sheng, P. Fluctuation-induced tunneling conduction in disordered materials. *Physical Review B* **21,** 2180–2195 (1980).

151. Phillips, P. J. Polymer crystals. *Reports on Progress in Physics* **53,** 549 (1990).

152. Nardes, A. M., Kemerink, M. & Janssen, R. A. J. Anisotropic hopping conduction in spin-coated PEDOT:PSS thin films. *Physical Review B* **76,** 085208 (2007).

153. Kawasumi, I, Sakata, M, Nishida, I & Masumoto, K. Crystal growth of manganese silicide, $MnSi_{1.73}$ and semiconducting properties of $Mn_{15}Si_{26}$. *Journal of Materials Science* **16,** 355–366 (1981).

154. Higgins, J. M., Schmitt, A. L., Guzei, I. A. & Jin, S. Higher Manganese Silicide Nanowires of Nowotny Chimney Ladder Phase. *Journal of the American Chemical Society* **130,** 16086–16094 (2008).

155. Girard, S. N., Chen, X., Meng, F., Pokhrel, A., Zhou, J., Shi, L. & Jin, S. Thermoelectric Properties of Undoped High Purity Higher Manganese Silicides Grown by Chemical Vapor Transport. *Chemistry of Materials* **26,** 5097–5104 (2014).

156. Pokhrel, A., Degregorio, Z. P., Higgins, J. M., Girard, S. N. & Jin, S. Vapor Phase Conversion Synthesis of Higher Manganese Silicide ($MnSi_{1.75}$) Nanowire Arrays for Thermoelectric Applications. *Chemistry of Materials* **25,** 632–638 (2013).

157. Luo, W., Li, H., Yan, Y., Lin, Z., Tang, X., Zhang, Q. & Uher, C. Rapid synthesis of high thermoelectric performance higher manganese silicide with in-situ formed nano-phase of MnSi. *Intermetallics* **19,** 404–408 (2011).

158. Norouzzadeh, P., Zamanipour, Z., Krasinski, J. S. & Vashaee, D. The effect of nanostructuring on thermoelectric transport properties of p-type higher manganese silicide $MnSi_{1.73}$. *Journal of Applied Physics* **112,** 124308 (2012).

159. Kaga, H., Kinemuchi, Y., Watari, K., Tanaka, S., Makiya, A., Kato, Z. & Uematsu, K. Fabrication of c-axis oriented higher manganese silicide by a high-magnetic-field and its thermoelectric properties. *Journal of Materials Research* **22,** 2917–2923 (2007).

160. Chen, X., Weathers, A., Salta, D., Zhang, L. B., Zhou, J. S., Goodenough, J. B. & Li, S. Effects of (Al,Ge) Double Doping on the Thermoelectric Properties of Higher Manganese Silicides. *Journal of Applied Physics* **114,** 173705 (2013).

161. Ikuto, A., Hiromasa, K., Lutz, R., Toshio, K., Mika, M., Seijiro, S. & Toshihide, T. Doping Effects on Thermoelectric Properties of Higher Manganese Silicides (HMSs, $MnSi_{1.74}$) and Characterization of Thermoelectric Generating Module using p-Type (Al, Ge and Mo)-doped HMSs and n-Type $Mg_2Si_{0.4}Sn_{0.6}$ Legs. *Japanese Journal of Applied Physics* **44,** 4275 (2005).

162. Chen, X., Zhou, J., Goodenough, J. B. & Shi, L. Enhanced thermoelectric power factor of Re-substituted higher manganese silicides with small islands of MnSi secondary phase. *Journal of Materials Chemistry C* **3,** 10500–10508 (2015).

163. Akio, Y., Swapnil, G., Hidetoshi, M., Manabu, I., Yoichi, N., Masaharu, M. & Tsunehiro, T. Thermoelectric Properties of Supersaturated Re Solid Solution

of Higher Manganese Silicides. *Japanese Journal of Applied Physics* **55,** 020301 (2016).

164. RGS Development B.V. Netherlands (2016, April 26). Retrieved from http://www.rgsdevelopment.nl/page21.html.

165. Kawasumi, I., Sakata, M., Nishida, I. & Masumoto, K. Crystal growth and characterization of $MnSi_{1.73}$. *Journal of Crystal Growth* **49,** 651–658 (1980).

166. Nishida, I. Semiconducting properties of nonstoichiometric manganese silicides. *Journal of Materials Science* **7,** 435–440 (1972).

167. De Ridder, R., van Tendeloo, G. & Amelinckx, S. Electron Microscopic Study of the Chimney Ladder Structures $MnSi_{2x}$ and $MoGe_{2x}$. *Physica Status Solidi A* **33,** 383–393 (1976).

168. Chen, X., Weathers, A., Carrete, J., Mukhopadhyay, S., Delaire, O., Stewart, D. A., Mingo, N., Girard, S. N., Ma, J., Abernathy, D. L., Yan, J., Sheshka, R., Sellan, D. P., Meng, F., Jin, S., Zhou, J. & Shi, L. Twisting phonons in complex crystals with quasi-one-dimensional substructures. *Nature Communications* **6,** 1 (2015).

169. Migas, D. B., Shaposhnikov, V. L., Filonov, A. B., Borisenko, V. E. & Dorozhkin, N. N. *Ab initio* study of the band structures of different phases of higher manganese silicides. *Physical Review B* **77,** 075205 (2008).

170. Zide, J., Vashaee, D, Bian, Z., Zeng, G, Bowers, J., Shakouri, A & Gossard, A. Demonstration of electron filtering to increase the Seebeck coefficient in $In_{0.53}Ga_{0.47}As/In_{0.53}Ga_{0.28}Al_{0.19}As$ superlattices. *Physical Review B* **74,** 205335 (2006).

171. Fujiwara, T. & Ishii, Y. *Quasicrystals* (Elsevier, 2007).

172. Chen, X., Bansal, D., Zhou, J., Delaire, O. & Shi, L. Weak coupling of acoustic-like phonons in incommensurate spin ladder compound $Sr_{14}Cu_{24}O_{41}$. *in preparation* (2016).

173. Finger, W. & Rice, T. M. Long-wavelength phonons in incommensurate systems. *Physical Review B* **28,** 340–358 (1983).

174. Currat, R., Katz, E. & Luk'yanchuk, I. Sound Modes in Composite Incommensurate Crystals. *European Physical Journal B* **26,** 339–347 (2002).

175. De Boissieu, M, Currat, R & Francoual, S. Phason modes in aperiodic crystals. *Handbook of Metal Physics* **3,** 107–169 (2007).

176. Peierls, R. Zur kinetishcen Theorie der Warmeleitung in Kristallan. *Annalen der Physik (Leipzig)* **3,** 1055 (1929).

177. Allen, P. B. & Feldman, J. L. Thermal Conductivity of Disordered Harmonic Solids. *Physical Review B* **48,** 12581–12588 (1993).

178. Allen, P. B., Feldman, J. L., Fabian, J. & Wooten, F. Diffusons, Locons and Propagons: Character of Atomic Vibrations in Amorphous Si. *Philosophical Magazine Part B* **79,** 1715–1731 (1999).

179. Ioffe, A. F. & Regel, A. R. *Progress in Semiconductors* (1960).

180. Feldman, J. L., Kluge, M. D., Allen, P. B. & Wooten, F. Thermal conductivity and localization in glasses: Numerical study of a model of amorphous silicon. *Physical Review B* **48,** 12589–12602 (1993).

181. Birch, A. F. & Clark, H. The thermal conductivity of rocks and its dependence upon temperature and composition. *American Journal of Science* **238,** 529–558 (1940).

182. Kittel, C. Interpretation of the Thermal Conductivity of Glasses. *Physical Review* **75,** 972–974 (1949).

183. Hardy, R. J. Energy-Flux Operator for a Lattice. *Physical Review* **132,** 168–177 (1963).

184. Nakayama, T. & Orbach, R. Anharmonicity and thermal transport in network glasses. *EPL (Europhysics Letters)* **47,** 468 (1999).

185. Seol, J. H., Moore, A. L., Saha, S. K., Zhou, F., Shi, L., Ye, Q. L., Scheffler, R., Mingo, N. & Yamada, T. Measurement and analysis of thermopower and electrical conductivity of an indium antimonide nanowire from a vapor-liquid-solid method. *Journal of Applied Physics* **101,** 023706 (2007).

186. Chen, X., Shi, L., Zhou, J. & Goodenough, J. B. Effects of ball milling on microstructures and thermoelectric properties of higher manganese silicides. *Journal of Alloys and Compounds* **641,** 30 –36 (2015).

187. Chen, X., Girard, S. N., Meng, F., Lara-Curzio, E., Jin, S., Goodenough, J. B., Zhou, J. & Shi, L. Approaching the Minimum Thermal Conductivity in Rhenium-Substituted Higher Manganese Silicides. *Advanced Energy Materials* **4.** 1400452, n/a–n/a. ISSN: 1614-6840 (2014).

188. Uchida, K., Xiao, J., Adachi, H., Ohe, J., Takahashi, S., Ieda, J., Ota, T., Kajiwara, Y., Umezawa, H., Kawai, H., Bauer, G. E. W., Maekawa, S. & Saitoh, E. Spin Seebeck insulator. *Nature Materials* **9,** 894–897 (2010).

189. Liao, B., Zhou, J. & Chen, G. Generalized two-temperature model for coupled phonon-magnon diffusion. *Physical Review Letters* **113,** 025902 (2014).

190. Hohensee, G. T., Wilson, R. B., Feser, J. P. & Cahill, D. G. Magnon-phonon coupling in the spin-ladder compound $Ca_9La_5Cu_{24}O_{41}$ measured by time-domain thermoreflectance. *Physical Review B* **89,** 024422 (2014).

191. Beeman, D. & Pincus, P. Nuclear Spin-Lattice Relaxation in Magnetic Insulators. *Physical Review* **166,** 359–375 (1968).

192. Giles, B. L., Yang, Z., Jamison, J. S. & Myers, R. C. Long-range pure magnon spin diffusion observed in a nonlocal spin-Seebeck geometry. *Physical Review B* **92,** 224415 (2015).

193. Birt, D. R., An, K., Tsoi, M., Tamaru, S., Ricketts, D., Wong, K. L., Khalili Amiri, P., Wang, K. L. & Li, X. Deviation from exponential decay for spin waves excited with a coplanar waveguide antenna. *Applied Physics Letters* **101,** 252409 (2012).

194. Sologubenko, A. V., Felder, E., Giann, K., Ott, H. R., Vietkine, A. & Revcolevschi, A. Thermal conductivity and specific heat of the linear chain cuprate Sr_2CuO_3 : Evidence for thermal transport via spinons. *Physical Review B* **62,** R6108–R6111 (2000).

195. Sologubenko, A. V., Giann, K., Ott, H. R., Ammerahl, U. & Revcolevschi, A. Thermal Conductivity of the Hole-Doped Spin Ladder System $Sr_{14-x}Ca_xCu_{24}O_{41}$. *Physical Review Letters* **84,** 2714–2717 (2000).

196. Jaworski, C. M., Yang, J., Mack, S., Awschalom, D. D., Myers, R. C. & Heremans, J. P. Spin-Seebeck Effect: A Phonon Driven Spin Distribution. *Physical Review Letters* **106,** 186601 (2011).

197. Kehlberger, A., Rser, R., Jakob, G., Ritzmann, U., Hinzke, D., Nowak, U., Onbasli, M. C., Kim, D. H., Ross, C. A. & Jungfleisch, M. B. Determination of the origin of the spin Seebeck effect-bulk vs. interface effects. *arXiv preprint arXiv:1306.0784* (2013).

198. Hoffman, S., Sato, K. & Tserkovnyak, Y. Landau-Lifshitz theory of the longitudinal spin Seebeck effect. *Physical Review B* **88,** 064408 (2013).

199. Jaworski, C. M., Myers, R. C., Johnston-Halperin, E. & Heremans, J. P. Giant spin Seebeck effect in a non-magnetic material. *Nature* **487,** 210–213 (2012).

200. Xiao, J., Bauer, G. E. W., Uchida, K.-c., Saitoh, E. & Maekawa, S. Theory of magnon-driven spin Seebeck effect. *Physical Review B* **81,** 214418 (2010).

201. Huang, S. Y., Fan, X., Qu, D., Chen, Y. P., Wang, W. G., Wu, J., Chen, T. Y., Xiao, J. Q. & Chien, C. L. Transport Magnetic Proximity Effects in Platinum. *Physical Review Letters* **109,** 107204 (2012).

202. Huang, S. Y., Wang, W. G., Lee, S. F., Kwo, J. & Chien, C. L. Intrinsic Spin-Dependent Thermal Transport. *Physical Review Letters* **107,** 216604 (2011).

203. Schreier, M., Kamra, A., Weiler, M., Xiao, J., Bauer, G. E. W., Gross, R. & Goennenwein, S. T. B. Magnon, phonon, and electron temperature profiles and the spin Seebeck effect in magnetic insulator/normal metal hybrid structures. *Physical Review B* **88,** 094410 (2013).

204. Uchida, K., Adachi, H., An, T., Ota, T., Toda, M., Hillebrands, B., Maekawa, S. & Saitoh, E. Long-range spin Seebeck effect and acoustic spinpumping. *Nature Materials* **10,** 737–741 (2011).

205. Eastman, D. E. Measurement of Third-Order Elastic Moduli of Yttrium Iron Garnet. *Journal of Applied Physics* **37,** 2312–2316 (1966).

206. O'Haver, T. *Command Line Peak Fitter, 7.4* (The University of Maryland at College Park, 2015). <https://terpconnect.umd.edu/~toh/spectrum/InteractivePeakFitter.htm>.

207. Demokritov, S. O., Demidov, V. E., Dzyapko, O., Melkov, G. A., Serga, A. A., Hillebrands, B. & Slavin, A. N. Bose-Einstein condensation of quasi-equilibrium magnons at room temperature under pumping. *Nature* **443,** 430–433 (2006).

Vita

Annie Weathers received her Bachelor of Science in Physics from New York University in 2010, and her Master of Science in Engineering from the Mechanical Engineering Department at The University of Texas at Austin in 2012 under the supervision of Professor Li Shi. She is the recipient of a NSF Graduate Research Fellowship, the Warren A. and Alice L. Meyer Endowed Scholarship in Engineering from UT Austin, and the Ben Streetman Junior Award for outstanding research by a graduate student in microelectronics.

Permanent email: annie.weathers@gmail.com

This dissertation was typed by the author.